INVESTIGATION OF IRON ISOTOPE VARIABILITY IN THE BIMODAL AZTEC WASH PLUTON, ELDORADO MOUNTAINS, NEVADA

BY

KELSEY KEHOE

THESIS

Submitted in partial fulfillment of the requirements
for the degree of Master of Science in Geology
in the Graduate College of the
University of Illinois at Urbana-Champaign, 2014

Urbana, Illinois

Adviser:

Professor Craig Lundstrom

ABSTRACT

Over the course of the past decade, our understanding of silicic plutons has undergone a fundamental shift, from envisioning pluton emplacement as one large magmatic intrusion to the concept of incremental emplacement, in which plutons form from multiple smaller injections of magma over hundreds of thousands to million-year time scales (Coleman et al., 2004; Glazner et al., 2004). While this concept helps to assuage previously held concerns about pluton emplacement, it also raises questions about the formation of features shared by many felsic intrusions, such as compositional zonation and the presence of significant volumes of relatively homogeneous granite.

Water-rich temperature gradient experiments (Huang et al., 2009) have been able to produce compositional zonation similar to that found in zoned plutons. The process that alters andesitic starting material to granitic and mafic end members within a temperature gradient is called thermal migration zone refining (Lundstrom, 2009). In addition to the compositional changes that occur within the temperature gradient, an isotopic signature was also observed: heavy isotopes of Fe, Mg, O, H and Li became enriched in the cold, felsic end of the gradient (Bindeman, et al., 2013; Huang et al., 2009). This isotopic trend is strikingly similar to one found in igneous systems, in which non-traditional stable isotopes such as Fe and Si become increasingly heavy as the silica content increases (Poitrasson and Freydier, 2005; Schoenberg and von Blanckenburg, 2006; Heimann et al., 2008; Savage, et al., 2011). Could the isotopic trend found in magmatic systems be related to temperature gradients formed as a result of multiple intrusions? There are only a few investigations of the role that temperature gradients have in driving isotopic fractionation within magmatic systems (Zambardi et al., 2014; Gajos, 2014).

In order to test this hypothesis, I have analyzed samples collected from transects oriented paleo-vertically and paleohorizontally through the Miocene-aged Aztec Wash Pluton (AW). AW is a bimodal, reversely zoned pluton, consisting of an outer "rim" of granite (the granite zone) underlain by the heterogeneous zone, which contains co-existing mafic, felsic and intermediate rocks. Rotation of the intrusion during Basin and Range extension exposed a sub-vertical slice of AW from the roof downwards, allowing for the paleovertical and paleohorizontal transects. Major element compositions and iron isotope ratios were measured for samples from four transects: PV, a paleovertical transect through the top of the pluton, ELT and 11-22, two paleohorizontal transects, and 11-20, a short transect through monzonite and monzodiorite layers. Fe isotope ratio results do not match reasonable Rayleigh fractionation models for fractional crystallization or fluid exsolution. The scattering of a range of iron isotope compositions of samples throughout the transects may be indicative of thermal diffusion signatures. However, the complicated open system history of AW has likely obscured the presence of simple diffusional gradients like those seen in the experiments (Huang et al. 2009; Bindeman et al. 2013).

ACKNOWLEDGEMENTS

I am grateful for my Advisor, Professor Craig Lundstrom, without whose patience, guidance, and wisdom I could not have completed this project. I would also like to thank my reader, Dr. Stewart, for his advice and sharp eye during the writing process. A big thank you goes to UIUC's Department of Geology for funding field work, analyses, and travel to GSA conferences through the Roscoe Jackson Travel fund and the Graduate Student Research fund. I also want to thank Meagan Pollock at the College of Wooster, NSF EAR-0958928 and the undergraduate students who work in the XRF lab for their help with sample preparation and XRF analyses. Thank you to Shane Butler for letting me use the jaw crusher and shatterbox at the ISGS. My gratitude goes to the administrative staff of the UIUC Geology Department, especially Lana Holben, Marilyn Whalen, Shelley Campbell and Lori Baker, who help the department to run as smoothly as possible. Thank you to my field assistants and fellow students, Norbert Gajos and Nick Huggett, whose enthusiasm and creativity help make field and lab work even more fun. I am also grateful to the entire Isotope Geology lab group at UIUC for their knowledge, help and friendship. I would also like to thank James Nguyen and Tommy Wiseau for providing much needed entertainment breaks. Finally I would like to thank my family, Sheila, Jim and Kyle for instilling in me curiosity and an appreciation of the outdoors from a young age.

TABLE OF CONTENTS

INTRODUCTION

The formation of silicic plutons has undergone a paradigm shift in the past decade, from viewing the emplacement process as a single large magmatic injection to the concept of incremental emplacement, in which a pluton is constructed from multiple smaller volume inputs of magma over the course of several hundred thousand to million years (Coleman et al., 2004; Glazner et al., 2004). While the quantity and volume of intrusions involved in incremental emplacement likely differ from pluton to pluton, one feature is common throughout: the intrusions represent large homogeneous swaths of granite. The question that begs to be asked is how does all this homogeneous granite form, especially if it is created from many small intrusions?

One proposed mechanism for the formation of zoned plutons with large proportions of granite is through thermal migration (Lundstrom, 2009). During laboratory experiments in which partially molten material sits in a temperature gradient, the process of thermal migration drives compositional differentiation (Huang et al., 2009; Lundstrom, 2009). In one particular experiment, andesite with 4 wt.% H_2O evolved into zones having 100% melt at the hot end, an amphibole-plagioclase gabbro in the middle and a granitic cold end (Huang et al., 2009). If an interconnected partial melt exists over a similar range in temperatures within magmatic systems, then the same processes acting within the thermal gradient experiments should also act in those systems. Notably, temperature gradient based processes might be traced using non-traditional stable isotope ratios like iron isotopes. Natural samples collected from the Aztec Wash pluton (Nevada), which is exposed in a ~5 km sub-vertical slice from the roof downwards, will be analyzed for iron isotope ratios in order to test the hypothesis that differentiation and isotopic fractionation occur across thermal gradients within a pluton.

Globally, we observe a correlation between non-traditional stable isotopes and extent of differentiation within igneous rocks; this indicates that iron isotope ratios can be used as a tracer of differentiation mechanisms. By furthering our knowledge of how iron isotopes fractionate within magmatic systems, we can identify the processes involved in the formation of silicic plutons, improving the broader understanding of continental crust growth.

BACKGROUND

Theoretical and experimental studies of Fe isotope fractionation in magmatic systems

Early measurements of iron isotope ratios in terrestrial and cosmochemical processes showed significant fractionation (Volkening and Papanastassiou, 1989; Dixon et al., 1992). This spurred theoretical and experimental research into the mechanisms behind fractionation of iron isotopes and predictions of fractionation between compounds that continues to this day. Early calculations based on Mössbauer spectroscopy data found that at temperatures up to 1000K there should be significant equilibrium isotope fractionation of iron between various Fe-bearing compounds (Polyakov, 1997). Polyakov and Mineev (2000) found that for minerals with ionic bonds, the reduced isotope partition function factors are higher for compounds with Fe^{3+} than those with Fe^{2+}. Similar results were found by Schauble et al. (2001), who, during modeling of equilibrium iron isotope fractionations between simple Fe-bearing complexes, found that the $^{56/54}$ Fe ratio will be higher in Fe(III)-bearing compounds than in compounds with Fe(II). Equilibrium experiments conducted between fayalite and magnetite agree with these predictions - showing that magnetite preferentially incorporates heavy isotopes relative to fayalite (Shahar et al., 2008). Shahar et al. (2008) predicts that if magnetite crystallization was the primary cause of iron fractionation, then the remaining melt which becomes more silicic would actually become isotopically lighter. This is echoed by experiments run by Bilenker et al. (2012) between magnetite and hydrous fluid, in which the magnetite is heavier than the co-existing fluid.

Iron isotope ratios observed in igneous rocks

With the advent of analytical techniques capable of measuring significant variations in non-traditional stable isotopes (NTSI) (such as iron, magnesium and silicon), we can now

investigate the drivers behind these isotopic fractionations, giving us a deeper look into earth systems processes. The system with the most data for igneous rocks to date is iron, whose isotopes have been measured in a variety of geologic materials (Beard and Johnson, 1999; Zhu et al, 2001; Beard et al., 2004; Poitrasson et al., 2004; Bergquist and Boyle, 2006; among others).

Initial high-precision measurements of iron isotopes in a variety of igneous rocks appeared to find no significant differences in isotopic composition (Beard and Johnson, 1999; Beard et al., 2003) and established a mean mafic-earth composition of iron isotopes. However, later studies began to notice that samples of silicic igneous rocks tended to have heavier iron isotope ratios than those from the mantle (Poitrasson and Freydier, 2005; Poitrasson, 2006; Schoenberg and von Blanckenburg, 2006); Poitrasson and Freydier (2005) were the first to find that granites with SiO_2 contents greater and 71 wt.% have significantly heavier $\delta^{56}Fe$ values. This finding was at first controversial but debate ended with the publication of Heimann et al. (2008). This observed increase in $\delta^{56}Fe$ values has been found in magmatic systems throughout the world, and appears to be unaffected by geologic setting (Figure 1) (Heimann et al., 2008; Poitrasson and Freydier, 2005; Schoenberg and von Blanckenburg, 2006; Schuessler et al., 2009; Zambardi et al, 2013).

There are multiple explanations given for the increase in $\delta^{56}Fe$ found in high-silica crustal rocks, with the origin of the signature still debated. I will briefly review each explanation:

1) Poitrasson and Freydier (2005) suggested that heavy iron isotopes could be left behind in a magma (melt with crystals of magnetite) if an aqueous fluid having light iron isotopes was exsolved and lost to country rocks due to saturation of water. Similarly Heimann et al. (2008), concluded that loss of a Cl-bearing fluid, exsolved from a highly evolved magma, could cause the heavy iron isotope signature found in granitic and volcanic samples. The exsolved fluid

would contain Fe^{2+}, which preferentially incorporates light iron isotopes. This would drive the remaining melt and crystals towards a heavier isotopic signature.

Telus et al. (2012) showed that while some felsic pegmatites and granites showed evidence for fluid exsolution perturbing the iron isotope ratios, not all samples showed this trend. For samples with high $\delta^{56}Fe$ that showed no evidence for fluid exsolution, their high iron isotope ratios were attributed to fractional crystallization. If fluid exsolution were to remove the light isotopes, then there should be a reservoir within the crust that contains this light signature. Possible reservoirs could include ore deposits, pegmatites or aplites; perhaps the fluids get dispersed throughout the crust, leaving behind no concentrated signature. With regards to pegmatites and aplites though, analyses have shown that they tend to have heavy iron isotope ratios similar to high-silica granitoids (Schoenberg and von Blanckenburg, 2006; Telus et al., 2012).

2) Schuessler et al. (2009) attributed variations in iron isotopes in a differentiation sequence of volcanic samples from Hekla to the formation and removal of titanomagnetite from the melt, and found no correlation between Fe fractionation and Li isotopes, an indicator of fluid exsolution, arguing against fluid exsolution as a mechanism by which all iron isotope ratios in silicic rocks are fractionated. Other research has also supported fractional crystallization as the cause of iron isotope fractionation. Simple Rayleigh fractionation modeling conducted by Schoenberg and von Blanckenburg (2006) showed that the $\delta^{56}Fe$ of a suite of intrusives could be matched by the crystallization of a mineral that removes light isotopes. However, to obtain the measured values, almost all iron would have to be removed from the melt (Schoenberg and von Blanckenburg, 2006). Additionally, neither models from Schoenberg and von Blanckenburg (2006) or Schuessler et al. (2009) use any theoretical or measured iron isotope partitioning

values. Sossi et al. (2012) showed that the iron isotopes changed systematically with Fe^{2+}:Fe^{3+} of the bulk rock during differentiation through the Red Hill sill complex, thus showing that redox plays the biggest role in regulating the iron isotope ratios of samples during fractional crystallization. A tholeiitic differentiation trend could control the iron isotope ratio of the melt due to the saturation-driven crystallization of magnetite, which preferentially incorporates heavy iron isotopes (Sossi, et al., 2012). Dauphas et al. (2014) coupled force constant and spectroscopy measurements of iron in silicate glasses with Rhyolite−MELTS modeling, and predicted that the equilibrium fractionation factor between the silicic melt and minerals increased with increasing silica content due to a change in the coordination geometry of iron within the melt. This should drive the remaining iron in the melt towards a heavier isotopic value (Dauphas et al., 2014). However, the MELTS model also showed that the major increase in the iron isotope ratio would occur when ilmenite is crystallizing, and after magnetite has stopped forming,

3) Lastly, another proposed mechanism, as discussed below, is thermal diffusion (Huang et al., 2009; Lundstrom, 2009). This proposes that isotopic sorting reflecting momentum differences of different isotopes occurs in a temperature gradient (Lacks et al., 2012).

This mechanism will occur anytime a fluid exists within a sustained temperature gradient with the cold end of the gradient always enriched in the heavy isotope; the amount of fractionation is independent of the magnitude of the gradient. It predicts that there will be changes in isotopic ratios with regards to spatial position within an intrusion, and a positive covariation of isotope ratios of different non-traditional stable isotopes.

Thermal diffusion and non-traditional stable isotopes in high-temperature systems

Thermal diffusion is defined as diffusion driven by temperature gradients. It has become important in understanding processes at work in biology (Braun and Libchaber, 2004), materials science (Shewmon, 1960; Assadi, et al., 2001), and the earth sciences (Li et al., 1997; Taylor and Luthin, 1978). One of the most interesting discoveries is that temperature gradients have been shown to cause isotopic fractionation in a wide variety of systems (Furry et al., 1939; Severinghaus et al., 2001; Ott, 1969; Reith and Muller-Plathe, 2000).

Laboratory experiments in which fully and partially molten silicates are placed within a temperature gradient (Kyser et al., 1998; Richter et al., 2008, 2009; Huang et al., 2009) show that systematic stable isotope fractionation occurs at magmatic conditions. Specifically, light isotopes are relatively enriched at the hot end, and heavy isotopes at the cold end. In 100% melt "Soret" experiments, Kyser et al. (1998) found that oxygen isotopes could be fractionated up to several permil in a temperature gradient of ~50°/mm. Likewise, Richter et al. (2008) found heavy Mg isotopes were enriched in the cool end of a 100% melt experiment. Experiment LTM-AGV-1, a thermal migration experiment by Huang et al (2009), showed similar behavior in terms of Mg and Fe isotope ratios as seen in Soret experiments, despite the fact that the charge consisted of melt plus crystalline solids. Thus, based on this result, isotopic fractionation occurring in a melt can be imparted on coexisting minerals, indicating the thermal diffusion process occurring in magmatic systems might be recorded in rocks.

Further investigation of O, Li and H isotopes within the LTM-AGV-1 experiment were reported in Bindeman et al. (2013). These three isotope systems were found to have significant fractionations across the temperature gradient experiment, and were considerably higher than in dry temperature gradient experiments (Bindeman et al., 2013). The presence of water appears to increase the rate of diffusion within a temperature gradient, much in the same way that water

also increases overall mass movement. Zambardi et al. (2014) report silicon isotope analyses of the cold end of the capsule in the LTM-AGV-1 experiment indicating that as SiO_2 concentration increases during thermal migration, Si isotope ratios become increasingly enriched in the heavier isotope.

Iron and silicon isotope ratios were measured for a sample set from the silicic Cedar Butte volcanic series, which span compositions from high-silica rhyolites to basaltic trachyandesite (Zambardi, et al., 2014). The results show that both silicon and iron isotopic ratios increase as the silica content of samples also increases (Zambardi, et al., 2014). These results are significant because while iron occurs as two valence states (Fe^{2+}, Fe^{3+}) in magma, silicon only has one (Si^{4+}). Mechanisms that suggest iron isotope ratios fractionate due to differences driven by changes in valence state, such as fractional crystallization and fluid exsolution, cannot be applied to silicon isotopes. This is why thermal migration is such a potentially important fractionator – it would explain similar trends seen in multiple isotopic systems.

Molecular dynamics simulations by Lacks et al. (2012) suggest that the isotopic fractionation within silicate liquid and crystal systems by thermal diffusion do not depend upon the actual value of the temperature gradient nor on the relative mass differences between isotopes. Instead Lacks et al. (2012) suggest that the isotopic fractionation occurs as a result of classical mechanical effects between heavy and light particles diffusively hopping through the temperature gradient and becoming isotopically sorted. Simply, heavy isotopes moving from the hot to the cold end of a temperature gradient will have greater momentum and therefore be more likely to exchange with and move to the cold end than a light isotope (Lacks et al., 2012). This is in contrast with the work of Dominguez et al. (2011) which hypothesized that isotopic fractionation in high-T silicate melt systems was due to zero-point energy effects. However this

model cannot explain the isotopic changes observed in LTM-AGV-1 and is thus not a consistent explanation the observation that the same fractionations occur in both Soret and thermal migration experiments.

Thermal migration as a mechanism of differentiation in high-temperature systems

Although the two types of experiments display identical isotopic behavior, Soret and thermal migration experiments show contrasting behavior when it comes to compositional changes. For instance, Soret experiments show significant increases in the concentrations of MgO, FeO and CaO at the cool end of the experiment, and the hot end became enriched in SiO_2 (Lesher and Walker, 1986; Richter et al., 2008). In contrast, thermal migration experiments show bulk compositional trends indicating that MgO, FeO and CaO decrease down temperature as phase proportions and compositions change (Lesher and Walker, 1988; Walker et al., 1988). For the Huang et al. (2009) temperature gradient experiment, what began as a uniform, hydrated, andesitic starting material, differentiated into a fine-grained granitic material at the cold end (350°C), a middle section of melt plus crystals of amphibole, plagioclase and magnetite-ilmenite, and a hot end (950°C) containing only melt. Overall, bulk major (and even trace) elements change in a manner mimicking a liquid line of descent.

Tuttle and Bowen's seminal work Origin of granite in the light of experimental studies in the system $NaAlSi_3O_8$-$KAlSi_3O_8$-SiO_2-H_2O (1958) showed that the composition of granitic rocks was the same as that of the minimum melt in equilibrium with quartz and alkali feldspar solid solution. Their results confirmed that granites were, in fact, igneous rocks, and not the result of a metasomatic/metamorphic "granitization" process. This also laid the groundwork for the rise of

mechanical processes such as fractional crystallization and partial melting as differentiation mechanisms.

The results of experiment LTM-AGV-1 (Huang, et al., 2009) suggest that thermal migration, the compositional differentiation of a mush (melt + crystals) via mineral-melt equilibrium and diffusion within a temperature gradient, can explain these questions. Within the cold end of LTM-AGV-1, bulk compositions are granitic, and similar to the minimum melt composition of Tuttle and Bowen (1958) despite starting with andesitic material (Lundstrom, 2009). How could this increase in felsic material occur? The answer may actually lie in other experiments conducted by Tuttle and Bowen and outlined in the previously mentioned 1958 tome. These showed that even below temperatures of 400°C, hydrous peralkaline silicate melts can coexist with quartz and potassium feldspar (Tuttle and Bowen 1958). The presence of intergranular porosity throughout the <400°C granitic end of LTM-AGV-1 points towards the presence of a melt at this end (Lundstrom, in prep).

Lundstrom (2009) based his hypothesis of granite formation via thermal migration zone refining on the results of experiment LTM-AGV-1 coupled with the concept of incremental assembly of plutons. The discovery that km-scale intrusions have million year age differences (Coleman et al., 2004; Glazner et al., 2004; Matzel et al., 2006) led to the idea of incremental assembly (Wiebe and Collins, 1998; Coleman et al., 2004; Miller et al., 2011). When a new volume of magma is added to a pluton, it brings with it heat and fluids. Thus the continued addition of new magma creates localized thermal gradients, which can lead to differentiation by thermal migration (Lundstrom, 2009). These later intrusions can often erase earlier evidence of previous intrusive mechanisms as well as contacts between injections, resulting in homogenized areas of rock (McNulty et al. 1996; Miller et al., 2011). This is why the trends found in non-

traditional stable isotope ratios in igneous rocks are potentially so important – they may help to differentiate between the processes of crystal fractionation and thermal migration zone refining. However, the injection process likely does not occur in a perfect top-down order. Multiple injections may occur simultaneously, or not near the center of the pluton. Thus, the simple non traditional stable isotopic fractionation patterns seen in temperature gradient experiments may be overprinted by such disordered intrusions.

Geologic Background of Aztec Wash Pluton

Aztec Wash pluton (AW), exposed within the Colorado River extensional corridor (CREC) in southern Nevada (Figure 2), is interpreted as having formed incrementally (Miller et al., 2011); U-Pb dating of zircons by SHRIMP estimate emplacement and solidification from ~15.5 - 15.8 Ma (Cates, et al., 2003). Regional extension occurred along the CREC starting ~15.5-16.2 Ma and ending by 9 Ma (Faulds, et al., 2001; Miller and Miller, 2002), exposing the pluton in three anti-formal fault blocks that have been rotated to reveal 5 km of vertical exposure, including the roof contact with overlying host rock (Figure 3) (Miller, et al., 2011). The eastern block contains exposures of the uppermost portion of the pluton. Due to unconstrained movement along the Thule Wash Fault, the stratigraphic position of the western block is unknown relative to the eastern block. The middle block contains far fewer exposures of rock, and is therefore not discussed in this paper.

The magmas that formed AW intruded into heterogeneous country rock of Proterozoic gneisses of the Mojave terrane, the 66Ma Ireteba Pluton, the middle Miocene Nelson Pluton and the early Miocene Pasty Mine Volcanic Suite (Kapp et al., 2006; Smith, et al., 2011).

Aztec Wash is lithologically divisible into two categories: along the top and side of the pluton is a ~1 km thick layer of granite called the granite zone, stratigraphically beneath this, in the center of the pluton, is the heterogeneous zone, which consists of rocks with compositions that range from troctolite to high-silica granites (Miller, et al., 2011).

The granite zone has been further subdivided based on texture (descriptions modified from those given in Harper et al, 2004):

1) Granite zone "cumulate" – This is a coarse-grained porphyritic granite with abundant feldspar phenocrysts and interstitial quartz. This also contains moderate abundances of mafic enclaves that range in scale from cm to ten meters. By using the term "cumulate" in this paper, we are not implying any specific petrogenesis of the rock, simply that it has a cumulate texture.
2) Transitional granite – This is a medium-grained granite with fewer feldspar phenocrysts and more quartz than in the coarse-grained granite. It also contains less abundant biotite than the coarse porphyritic granite (the "cumulate").
3) Chilled Border granite – This is a fine-grained phaneritic granite that occurs along the margin of the pluton adjacent to the country rock. This lithology coarsens into the medium grained granite tens of meters away from the contact.
4) Border porphyritic granite – This is a light gray porphyritic granite with a granophyric groundmass that ranges from aphanitic to very-fine grained phaneritic. This rock type contains phenocrysts of alkali feldspar, plagioclase and biotite. It is interpreted to have been the top of the pluton.

5) Felsic border granite – This is a porphyritic leucogranite that occurs along the edge of the pluton. The groundmass is very fine grained, and with phenocrysts of feldspar and quartz. It is finer than the transitional granite.
6) Miarolitic border granite – This is a leucogranite containing miarolitic cavities that range in size from mm to a few cm across. The rock has a granophyric texture with rare biotite. It occurs adjacent to country rock.

The heterogeneous zone contains a wide variety of lithologies and petrologic textures, including felsic pipes, alternating layers of felsic rocks (granite to quartz monzonite) with granodiorite, diorite, quartz monzodiorite and gabbro, mafic enclaves within granitic host rock that occur individually and in groups, phaneritic gabbroic layers with aphanitic edges, and repeating layers of amphibole-rich diorites with varying crystal sizes (Figure 4). While it is common for felsic intrusions to have exposures of enclave-rich areas, it is relatively rare to see a bimodal zone as large or as varied as that of Aztec wash. This feature, coupled with the large vertical exposure, makes the AW an ideal field site in which to study the spatial distributions of iron isotopes within a single intrusion in an effort to further our understanding of the mechanisms behind iron isotope fractionation and thus formation of silicic igneous rocks.

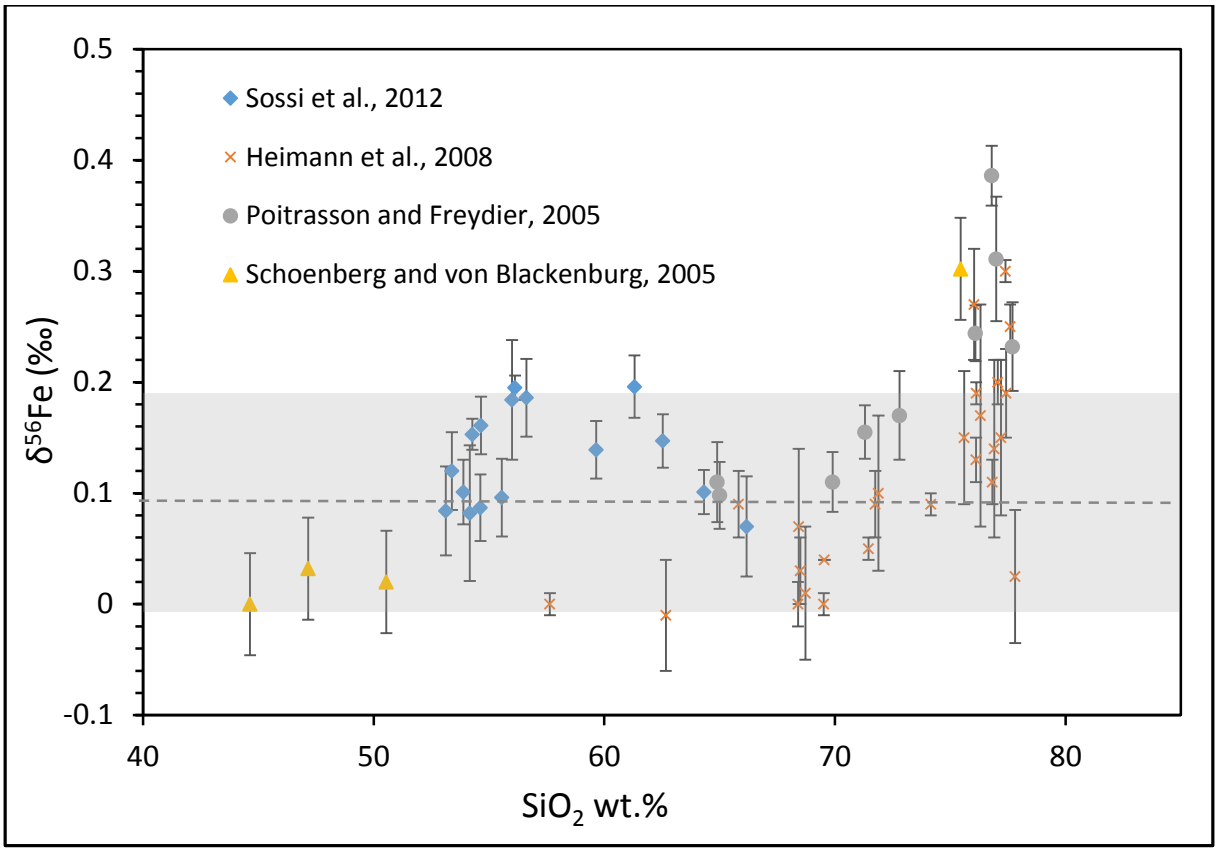

Figure 1. Plot of $\delta^{56}Fe$ vs. SiO_2 wt.% for previously published iron isotope data of intrusive igneous rocks. For high silica rocks, the iron isotope ratios are more likely to be heavier than for rocks with less silica. The mechanism driving this increase in $\delta^{56}Fe$ is still debated. The data plotted here include samples from a tholeiitic sill complex (Sossi, et al., 2012), convergent margin intrusive rocks (Schoenberg and von Blackenberg, 2005; Heimann, et al., 2008), and peralkaline and peraluminous intrusives (Poitrasson and Freydier, 2005). Horizontal dashed line represents the "bulk earth" value of +0.09‰ (Beard et al., 2003). Shaded region represents the 2σ error of ±0.10‰ for the bulk earth $\delta^{56}Fe_{IRMM\text{-}14}$ as determined by Dauphas and Rouxel (2006).

Figure 2. Location map showing the location of the Aztec Wash pluton relative to geographic features of the region.

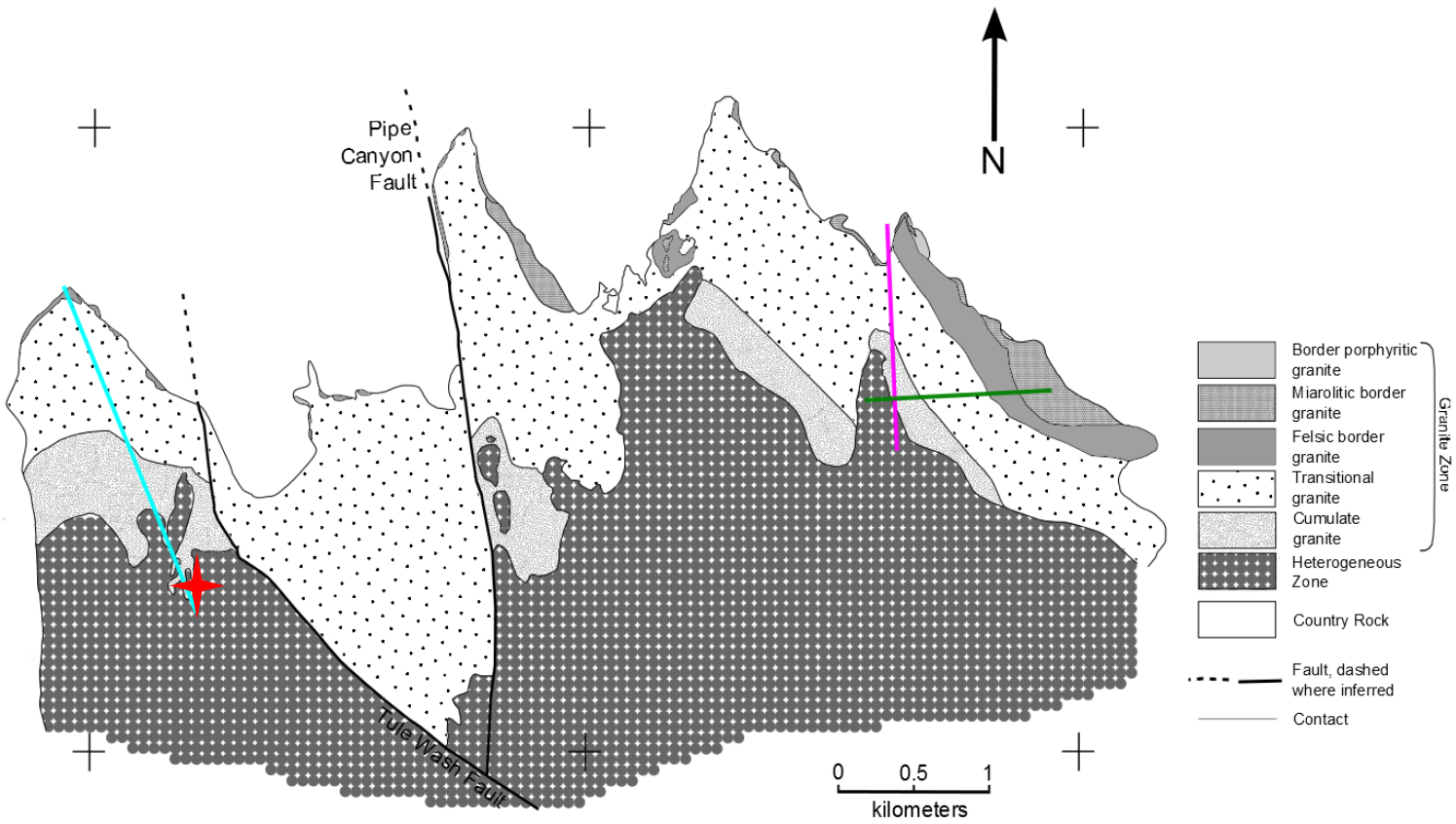

Figure 3. Geologic map of Aztec Wash pluton and the surrounding undifferentiated country rock. The pluton has been structurally divided into western, eastern and central blocks. The different transects are represented on the map by the colored lines. In the eastern block is the PV transect (green) and the ELT transect (pink). Within the western block is the 11-22 transect (blue line) and the 11-20 transect (the red star). (Geologic map after Harper et al, 2004).

(a)

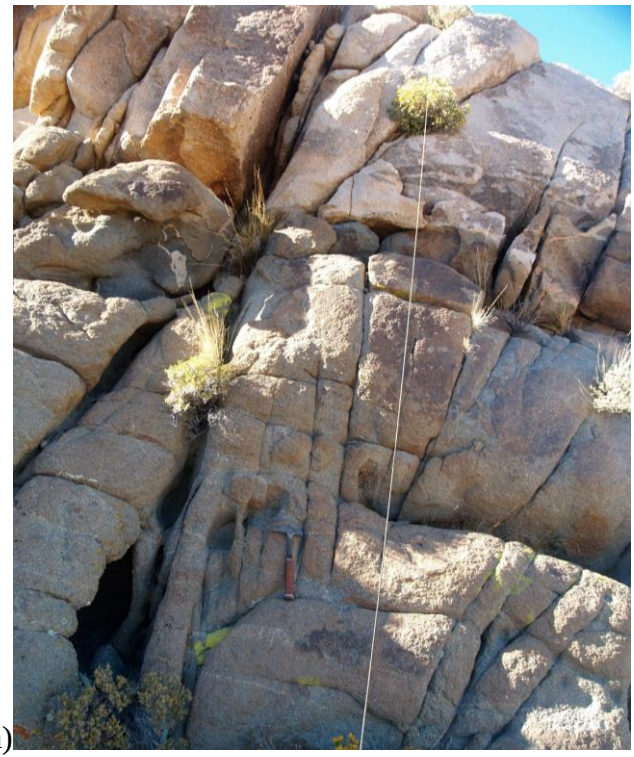

(b)

Figure 4. Images of outcrops from the heterogeneous zone of Aztec Wash pluton. (a) Shows an example of an area with felsic over mafic sheets. Both the felsic and mafic layer contain enclaves of material with opposing compositions. The mafic layer also contains thin cm-scale felsic dikes. (b) This image shows a common intrusive texture within the heterogeneous zone, of irregularly shaped blobs of fine-grained mafic material surrounded by coarser-grained felsic to intermediate rock. In both images a hammer is included for scale.

SAMPLES AND METHODS

Sample collection

Two trips were made to the Aztec wash Pluton in the Eldorado Mountains in November 2012 and March 2013 to collect samples. Samples range in mass from 0.1 kg to over 2 kg. The samples collected are from both the heterogeneous zone and the granite zone of Aztec Wash, and thus display a large variety of textures and mineral modes, with compositions ranging from high-silica granites to troctolite. Samples were collected along transects expected to represent paleohorizontal and paleovertical lines within the pluton (Figure 3, based on the map of Harper et al. (2003)). These transects extend from country rock, through the granite zone of Aztec Wash and into the heterogeneous zone. This paper will focus on four sample transects collected within the Aztec Wash Pluton named PV, ELT, 11-22, and 11-20.

PV is a paleovertical transect, 1.3 km long, which extends from the miarolitic border granite in the roof of the pluton, through the felsic border granite and transitional granite and into the uppermost lobe of the heterogeneous zone.

The ELT transect, 2 km long, is also located in the easternmost block of the pluton, and runs approximately paleohorizontally from country rock north of the pluton, into the felsic border granite, the transitional granite, the cumulate granite and to the easternmost lobe of the heterogeneous zone. Three of the first four samples are of country rock with gneissic to schistose textures. They contain varying levels of foliated biotite with quartz and feldspar. The third sample of the transect, ELT 3, is from a meter-scale felsic dike that cuts through the country rock.

The 11-22 transect is a paleohorizontal transect through the western block of Aztec Wash. Due to unconstrained movement along the Thule Wash fault, it's stratigraphic position

relative to transects within the eastern block is uncertain. At 2.8 km long, the transect starts in country rock near the northern contact. The first sample, of granoblastic feldspathic quartzite, was collected tens of meters from the intrusive contact, which is buried by colluvium in a narrow wash. From the country rock the transect passes through the granite zone sub-units of felsic border granite, transitional granite, a mafic dike cutting through the transitional granite, and cumulate granite, then into a lobe of the heterogeneous zone.

The 11-20 transect is a shorter paleovertically oriented transect, only 10 m in length, and is located within the heterogeneous zone within the western block of AW near the end of the 11-22 transect. In this area of the heterogeneous zone are alternating layers of mafic and felsic rock. The transect passes perpendicularly through a layer of quartz-monzonite stratigraphically above a biotite-rich monzodiorite layer (Figure 5). The contact between the lithologies is relatively sharp, with feldspar phenocrysts creating a crenulated contact at centimeter scales. Near the contact on the felsic side are blocky, fine-grained enclaves of intermediate to mafic composition. Meters away from the transect, felsic enclaves can be found within the monzodioritc layer. Enclaves range in size from 10 to 50 cm. The monzodiorite layer is also cross-cut by centimeter-scale, fine to medium grained felsic dikes.

Sample preparation and analyses

At the University of Illinois, 10-20 g blocks were cut from samples, and afterwards were sonicated twice in water to remove any foreign particles and loosely bound weathered material. The cut sample blocks were crushed using jaw crushers at the Illinois State Geological Survey (ISGS). Five to ten grams of powder were made from the crushed material using the alumina

shatterbox at the ISGS. The powdered samples were used for analyses of major elements and for iron isotope compositions.

Major element analyses

Glasses for X-Ray Fluorescence (XRF) spectrometry were prepared at the College of Wooster. Sample powders were ground to finer grain size with an agate mortar and pestle, then sieved using a no. 325 sieve. Approximately 2 mg of sample were weighed into ceramic crucibles and Loss On Ignition (LOI) was determined by oxidizing samples in a 950°C furnace for 1 hour (Pollock et al., 2014). For the fusions, 1.2500 ± 0.0001g of sample were mixed with 8.7500 ± 0.0001g of Lithium Tetraborate flux, and the mixture was fused in a Katanax K1 fluxer.

The major element composition of the glasses were measured on the Rigaku ZSX Primus II X-Ray Fluorescence spectrometer XRF, which uses a 4kW Rh-target. Before each run drift correction was applied to the XRF. Each glass was analyzed 3 times, and duplicate glasses were made for two samples. Standards used in the run were the USGS standards BHVO-2, AGV-2 and GSP-2.

Iron isotope analyses

For Fe isotope analysis, 5 to 15 mg sample powder was digested in HF and HNO_3, followed by column chemistry involving 8N HCl and AG1-X8 100-200 mesh resin in 0.5ml polyethylene columns, following established procedures (Schoenberg and von Blanckenberg, 2005). Fe isotope ratio analyses were performed at the University of Illinois Department of Geology's Nu-plasma HR MC-ICPMS in dry plasma mode using a $^{58}Fe/^{57}Fe$ double-spike. High mass resolution mode was used to resolve peaks of Fe from mass interferences ($M/\Delta M$ of

>5000), and both $^{58}Fe/^{57}Fe$ double-spike and standard-sample bracketing methods were used to correct for instrumental mass bias. The bracketing standard used was IRMM-14, and BCR-1 and UI-Fe (an in-house Fe standard) were used as secondary standards to assess accuracy of offsets. Results are reported as

$$\delta^{56}Fe = \frac{{}^{56}Fe/{}^{54}Fe_{sample} - {}^{56}Fe/{}^{54}Fe_{IRMM-14}}{{}^{56}Fe/{}^{54}Fe_{IRMM-14}} \times 1000‰.$$

BCR-2, one of the secondary standards used during analyses, had an average $\delta^{56}Fe = 0.08 \pm 0.02‰$ (error is 2se, n=34). The accepted value of BCR-2 is $\delta^{56}Fe = 0.06 \pm 0.03‰$ (error is 2se) (Dauphas and Rouxel, 2006). The other secondary standard used, UI-Fe, had an average $\delta^{56}Fe = 0.68 \pm 0.02$ ‰ (error is 2se, n=54). The accepted value for UI-Fe is $\delta^{56}Fe = 0.71 \pm 0.09‰$ (Huang et al. 2011).

Three samples were re-analyzed to determine the reproducibility. Sample 11-17-4 was analyzed during two separate runs, for a total of four analyses. The average $\delta^{56}Fe = 0.14 \pm 0.05‰$ (2σ). Another sample, 11-17-7, analyzed a total number of six times (on three separate occasions), gave an average $\delta^{56}Fe = 0.13 \pm 0.05‰$ (2σ). However, another sample, 11-17-8 was analyzed on two separate occasions ($n = 4$), and its average $\delta^{56}Fe$ is 0.09 ± 0.08‰ (2σ). By averaging the three 2σ values calculated for repeat measurements, then the 95% confidence interval of reproducibility is 0.06‰.

Figure 5. Shows the outcrop from which transect 11-20 is sampled. The transect consists of samples from a monzonitic layer and a monzodiorite layer beneath it. The monozonitic layer continues horizontally across the hillside, and overlies another monzonitic layer.

RESULTS

PV transect

Ten samples were analyzed in the PV transect (Figure 6). The sample collected in the miarolytic granite zone closest to the contact with the country rock has the highest δ^{56}Fe of the transect at +0.32 ± 0.04‰. Further away from the transect the δ^{56}Fe decreases within the felsic border granite subunit, then increases within the transitional granite unit. The next samples are heterogeneous zone granites and diorites, which share fairly homogenous δ^{56}Fe. Overall there is a trend of decreasing δ^{56}Fe as depth in the pluton increases. The lightest values occur within the heterogeneous zone.

ELT transect

Twenty samples were analyzed for the ELT transect (Figure 7). The majority of country rock samples have iron isotope ratios similar to the three Aztec Wash samples nearest the contact. One country rock sample has a significantly lower δ^{56}Fe than the rest. Samples from the border porphyritic granite, at the edge of the pluton, and the transitional granite show relatively similar iron isotope ratios. The two samples with the heaviest δ^{56}Fe values occur near the outer edge of the felsic border granite. They are sandwiched by samples that are ~0.10‰ lighter. δ^{56}Fe values show a decreasing trend from the felsic border granite through to the heterogeneous zone. Near the end of the transect, the last samples within the heterogeneous zone show a variety of δ^{56}Fe values, between 0.09‰ and 0.23‰.

11-22 transect

11-22 is the paleohorizontal transect that is located in the western block of the Aztec Wash Pluton (Figure 8). Due to unknown amounts of movement along the Thule Wash fault, the stratigraphic position of this transect is unknown with respect to transects in the eastern block of Aztec Wash. The transect starts with a trend of increasing δ^{56}Fe values from the country rock, through the felsic border granite and into the transitional granite. This upward trend peaks three samples into the transitional granite zone with the heaviest sample, a porphyritic aphanitic granite. Further into the transition zone, a sample of a mafic dike has a significantly lower iron isotope ratio than surrounding samples. Samples throughout the cumulate granite and the heterogeneous zone sections have widely varying δ^{56}Fe values that show large changes over relatively short distances. An aplitic sample from the heterogeneous zone and a sample of cumulate granite that fingers into the heterogeneous zone both have δ^{56}Fe values significantly heavier than surrounding samples.

11-20 transect

This short transect consists of seven samples, five from a layer of granite and two from diorite beneath the granite (Figure 9). The felsic layer consists of porphyritic to phaneritic granite with dioritic enclaves near the contact with the layer of phaneritic diorite. Despite differences in mineralogy between the two sampled layers, the δ^{56}Fe of samples from both layers have a relatively small range, falling between +0.08‰ to +0.15‰.

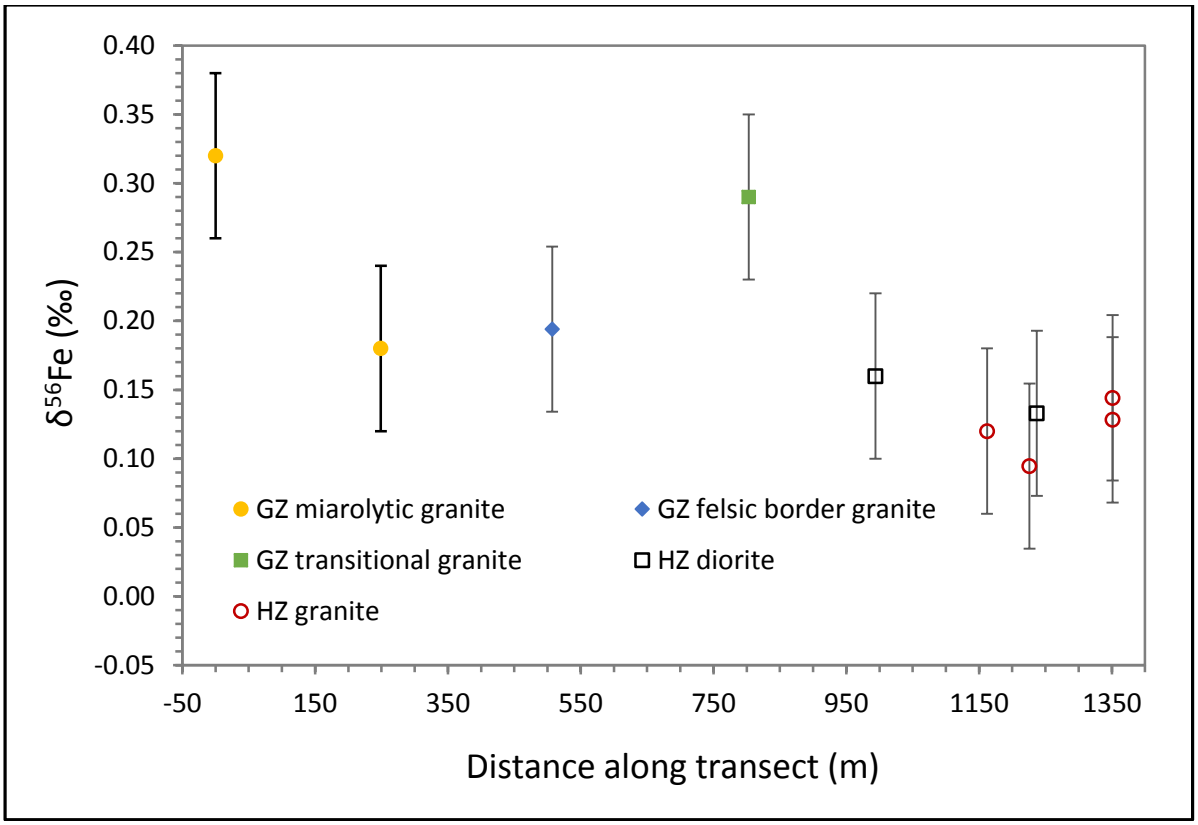

Figure 6. Plot of δ^{56}Fe vs. distance along PV transect, which runs approximately paleovertically from the roof of the pluton, through the miarolitic granite, felsic border granite and transitional granite sub-units of the granite zone, into the easternmost lobe of the heterogeneous zone. As depth into pluton increases, the δ^{56}Fe decreases overall.

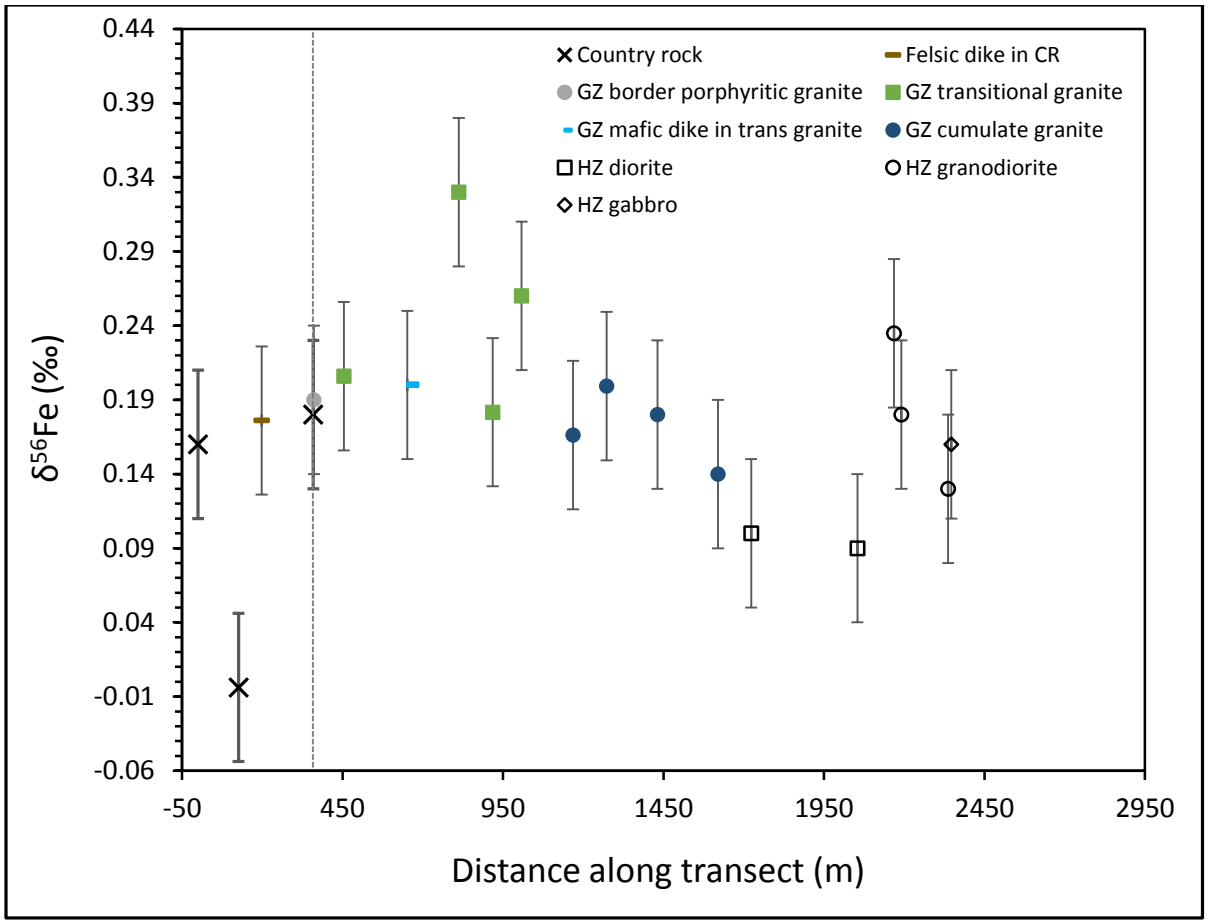

Figure 7. Plot of δ^{56}Fe vs. distance along ELT transect, which runs from country rock through the granite zone sub-units of border porphyritic granite, transitional granite and cumulate granite into the easternmost lobe of the heterogeneous zone, where diorite and granodiorite are sampled. Grey dashed line represents the inferred contact between country rock and Aztec Wash pluton. Note trend of increasing δ^{56}Fe among first five intrusive samples.

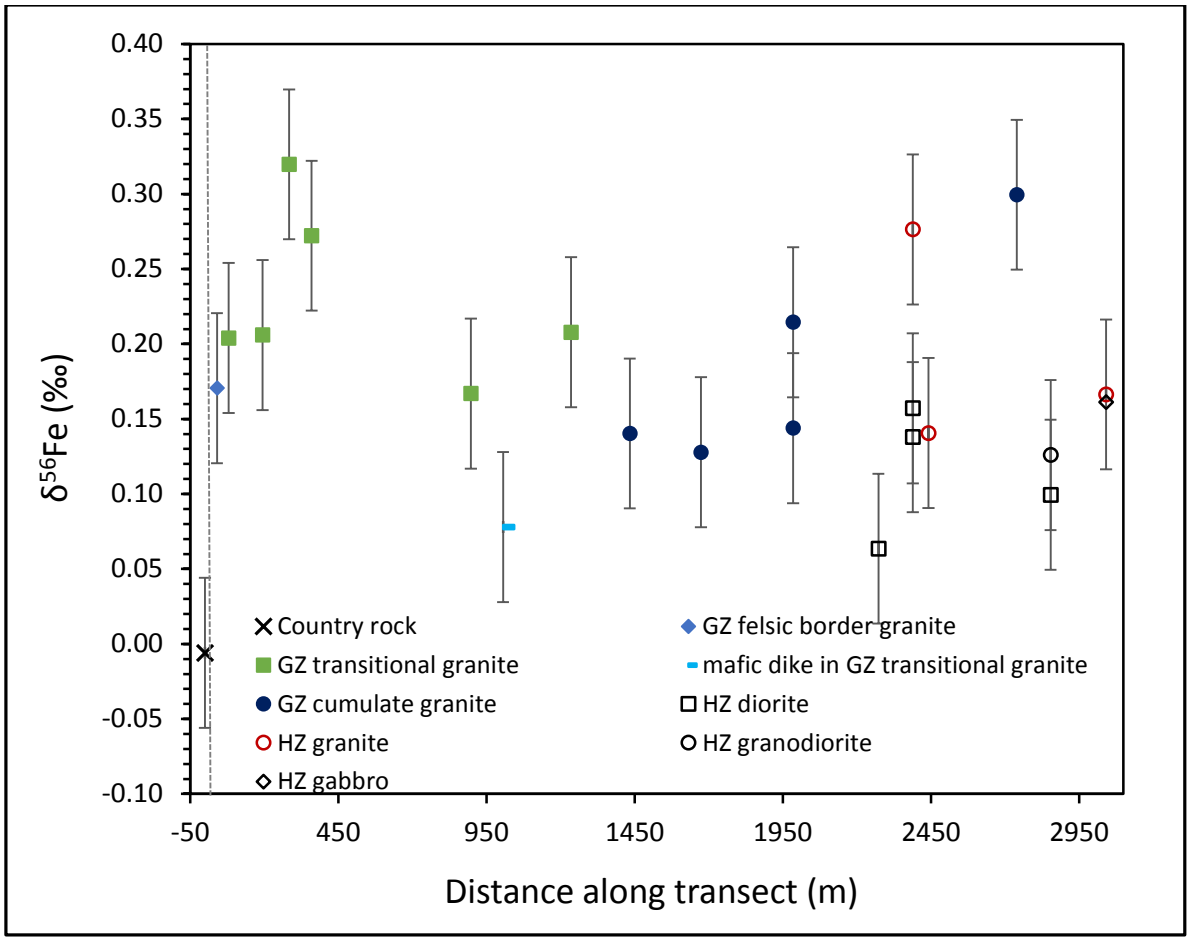

Figure 8. Plot of δ^{56}Fe vs. distance along 11-22 transect, which runs from country rock into the felsic border granite, transitional granite, a mafic dike in the transitional granite, cumulate granite and diorite, granite, granodiorite and gabbro of the heterogeneous zone. The dashed line represents the inferred contact between the country rock and Aztec Wash pluton. Within the first ~500 m from the contact the Aztec Wash samples show very significant increases in δ^{56}Fe.

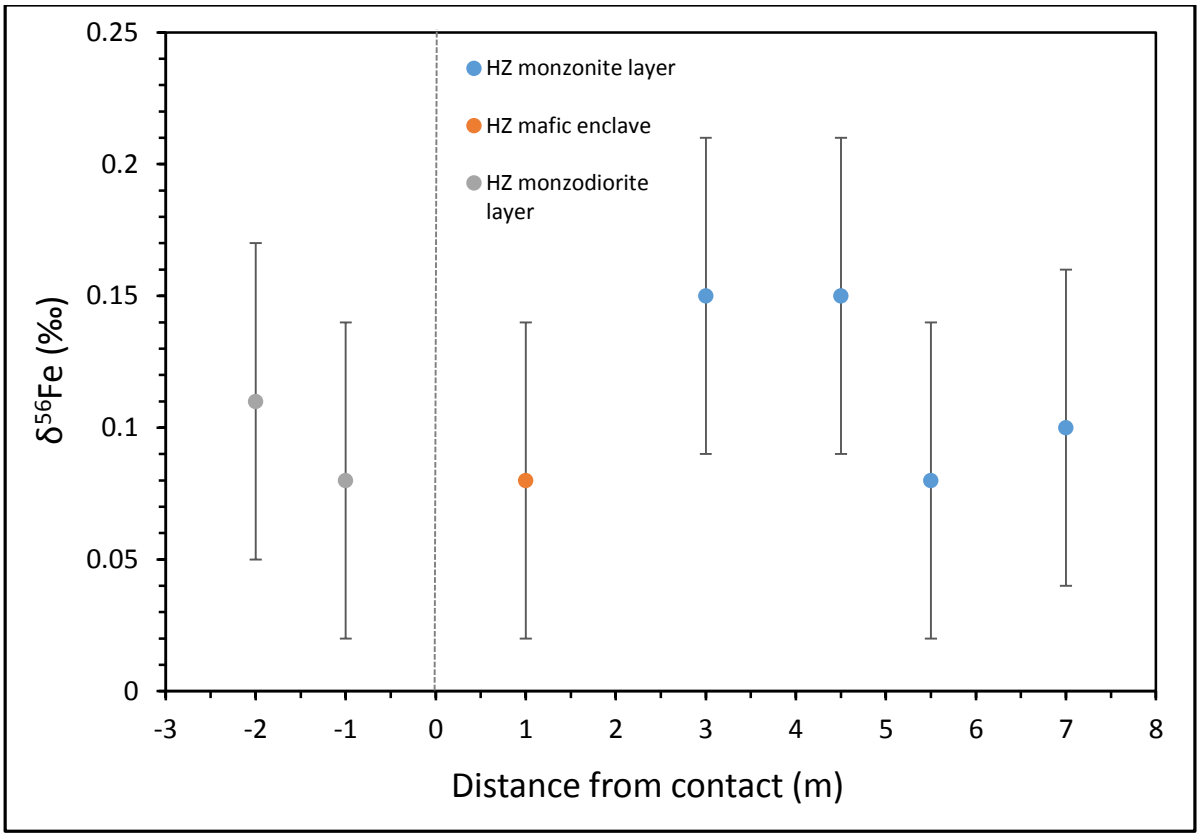

Figure 9. Plot of δ^{56}Fe vs. distance from contact in the 11-20 transect. Transect spans a layer of monzonite above a layer of monzodiorite. Near the contact on the monzonite side are enclaves of fine-grained mafic material. δ^{56}Fe values are relatively homogeneous across the contact. Contact is represented by the dashed grey line. Error bars represent external reproducibility.

Sample	SiO_2	TiO_2	Al_2O_3	Fe_2O_3	MnO	MgO	CaO	Na_2O	P_2O_5	K_2O	BaO	Sum	LOI
PV-1	76.43(03)	0.14(00)	13.25(01)	0.80(00)	0.06(00)	0.12(00)	0.53(00)	3.68(03)	0.00(00)	4.99(01)	0.00(00)	100.00	0.01
PV-2	73.24(05)	0.24(01)	14.50(02)	1.20(00)	0.03(00)	0.30(01)	1.16(01)	3.79(02)	0.05(00)	5.45(01)	0.04(00)	100.00	0.02
PV-3	71.08(01)	0.33(00)	15.60(02)	1.61(00)	0.04(00)	0.42(00)	1.27(01)	3.94(00)	0.09(00)	5.56(00)	0.071(01)	100.00	0.01
PV-4	70.74(03)	0.31(00)	15.72(03)	1.58(00)	0.03(00)	0.45(00)	1.58(00)	4.27(00)	0.11(00)	5.13(01)	0.09(01)	100.00	0.02
PV-5	63.64(02)	0.68(00)	16.96(02)	3.67(01)	0.07(00)	1.72(01)	4.05(01)	4.31(02)	0.50(00)	4.25(01)	0.14(00)	100.00	0.03
PV-6	66.50(02)	0.57(00)	16.57(01)	2.92(01)	0.06(00)	1.03(01)	2.78(01)	4.52(02)	0.25(00)	4.67(01)	0.14(00)	100.00	0.01
PV-7	68.93(01)	0.39(00)	16.27(03)	1.79(01)	0.04(00)	0.53(00)	1.96(00)	4.24(02)	0.18(00)	5.55(00)	0.13(00)	100.00	0.01
PV-8	54.81(02)	1.57(01)	15.28(02)	7.26(01)	0.17(00)	4.73(03)	7.90(01)	4.13(01)	0.97(00)	3.05(01)	0.11(01)	100.00	0.02
PV-8 d	54.79(03)	1.57(01)	15.27(01)	7.29(03)	0.17(00)	4.74(03)	7.90(01)	4.14(01)	0.97(00)	3.05(01)	0.11(00)	100.00	0.02
PV-9	69.28(07)	0.36(00)	16.28(01)	1.79(00)	0.05(00)	0.70(00)	1.70(00)	4.33(02)	0.15(00)	5.12(00)	0.07(00)	99.84	0.02
PV-10	69.98(01)	0.30(00)	15.83(02)	1.75(01)	0.06(00)	0.58(01)	1.69(01)	4.03(03)	0.12(00)	5.57(01)	0.08(00)	100.00	0.02
11-20-1	68.20(02)	0.50(00)	16.56(02)	2.27(00)	0.04(00)	0.71(01)	1.72(00)	4.27(04)	0.20(00)	5.40(01)	0.14(00)	100.00	0.02
11-20-2	68.19(03)	0.63(00)	16.15(02)	2.47(00)	0.05(00)	0.80(01)	1.80(00)	4.17(04)	0.27(00)	5.36(01)	0.11(01)	100.00	0.02
11-20-3	68.54(09)	0.67(00)	16.27(03)	2.24(00)	0.04(00)	0.74(01)	1.58(00)	4.27(02)	0.20(00)	5.21(01)	0.12(00)	99.87	0.02
11-20-5	67.74(03)	0.70(00)	15.96(01)	2.26(00)	0.04(00)	0.79(01)	2.79(01)	4.39(02)	0.21(00)	5.02(01)	0.12(01)	100.00	0.03
11-20-6f	66.70(05)	0.48(01)	17.34(02)	2.07(01)	0.04(00)	0.78(00)	2.22(00)	4.42(03)	0.20(00)	5.60(00)	0.17(00)	100.00	0.01
11-20-6m	55.79(03)	1.16(01)	14.03(01)	8.13(03)	0.18(00)	6.59(01)	6.50(01)	3.61(01)	0.98(00)	2.93(00)	0.11(01)	100.00	0.04
11-20-7	68.09(04)	0.56(01)	16.82(02)	1.91(00)	0.03(00)	0.65(00)	1.52(00)	4.18(04)	0.17(00)	5.95(01)	0.14(00)	100.00	0.02
11-20-7 d	67.69(02)	0.53(00)	16.68(02)	1.86(00)	0.03(00)	0.62(00)	1.50(01)	4.12(03)	0.16(00)	5.95(01)	0.14(01)	99.28	0.02
11-20-8	57.00(03)	1.18(00)	14.07(02)	7.49(00)	0.14(00)	6.01(02)	6.43(00)	3.45(03)	0.84(00)	3.25(01)	0.13(00)	100.00	0.03
11.20.9	55.46(02)	1.20(00)	13.82(02)	7.75(02)	0.13(00)	6.47(03)	6.87(00)	3.17(02)	0.98(00)	3.42(01)	0.14(00)	99.41	0.03
ELT1	56.36(02)	1.04(01)	22.19(02)	10.39(03)	0.11(00)	3.05(02)	0.75(00)	1.34(01)	0.04(00)	4.40(00)	0.14(01)	99.79	n/a

Table 1. Major oxide data (in wt.%) of 32 samples from three Aztec Wash transects and three standard glasses. The two samples ending in d (PV-8 and 11-20-7) indicate analyses of duplicate glasses. The standard BHVO-2 is a duplicate analysis of the BHVO-2 standard. Error is reported in 2s.

Sample	SiO_2	TiO_2	Al_2O_3	Fe_2O_3	MnO	MgO	CaO	Na_2O	P_2O_5	K_2O	BaO	Sum	LOI
ELT2	73.43(04)	1.12(00)	11.93(02)	5.51(01)	0.06(00)	2.00(01)	1.12(01)	1.72(01)	0.01(00)	2.87(01)	0.04(00)	99.82	0.03
ELT3	68.81(04)	0.30(00)	16.03(01)	1.82(00)	0.02(00)	0.64(01)	0.37(00)	2.88(01)	0.07(00)	8.95(00)	0.11(00)	100.00	0.01
ELT7	71.40(02)	0.28(01)	15.88(01)	1.22(00)	0.02(00)	0.51(01)	1.33(00)	4.73(02)	0.06(00)	4.42(00)	0.16(00)	100.00	0.01
ELT8	72.88(02)	0.34(00)	13.81(01)	1.94(00)	0.03(00)	0.61(01)	1.12(00)	3.24(01)	0.08(00)	5.83(01)	0.13(00)	100.00	0.02
ELT10	57.75(01)	1.51(00)	14.26(00)	7.91(02)	0.12(00)	5.15(00)	5.06(00)	3.33(03)	0.58(00)	3.75(00)	0.12(00)	99.54	0.02
ELT11	73.20(02)	0.21(00)	14.64(02)	0.90(00)	0.03(00)	0.29(01)	0.76(000	4.05(02)	0.01(00)	5.55(01)	0.02(00)	99.65	0.02
ELT12	74.86(01)	0.15(00)	14.03(01)	0.79(00)	0.03(00)	0.14(01)	0.56(01)	3.61(01)	0.02(00)	5.79(01)	0.02(00)	100.00	0.01
ELT13	73.49(01)	0.23(00)	14.53(02)	0.94(00)	0.03(00)	0.32(00)	0.82(00)	3.86(01)	0.04(00)	5.73(01)	0.02(00)	100.00	0.01
ELT14	73.84(05)	0.28(00)	14.02(03)	1.39(00)	0.02(00)	0.37(00)	0.86(00)	3.59(02)	0.07(00)	5.40(01)	0.05(00)	99.90	0.02
ELT15	72.53(04)	0.26(00)	14.83(05)	1.48(00)	0.03(00)	0.39(01)	1.27(01)	3.64(03)	0.10(00)	5.39(01)	0.07(00)	100.00	0.02
ELT16	69.69(06)	0.48(00)	15.55(03)	2.25(00)	0.07(00)	0.98(00)	1.52(00)	3.89(03)	0.16(00)	5.35(01)	0.06(00)	100.00	0.03
ELT17	72.22(05)	0.29(01)	14.69(07)	1.53(01)	0.03(00)	0.42(01)	1.38(01)	3.58(02)	0.07(00)	5.54(01)	0.08(00)	99.84	0.02
ELT18	68.62(02)	0.44(00)	16.17(02)	2.15(00)	0.06(00)	1.01(01)	1.92(01)	4.12(00)	0.17(00)	5.28(00)	0.08(00)	100.00	0.04
ELT19	57.54(02)	1.22(00)	14.27(02)	7.54(01)	0.14(00)	5.84(02)	5.56(01)	2.95(02)	0.46(00)	3.26(01)	0.13(01)	98.92	0.04
ELT23	58.85(12)	1.13(01)	15.32(03)	6.60(01)	0.13(00)	4.03(00)	4.89(01)	3.94(02)	0.43(00)	4.33(01)	0.16(00)	99.81	0.02
ELT24	65.40(02)	0.58(01)	17.25(03)	2.82(01)	0.05(00)	1.02(01)	3.01(00)	4.68(01)	0.29(00)	4.51(01)	0.14(00)	99.74	0.01
ELT25	69.26(03)	0.36(00)	16.24(02)	2.02(00)	0.05(00)	0.94(01)	1.95(00)	4.05(03)	0.12(00)	4.89(01)	0.13(00)	100.00	0.02
ELT26	69.04(03)	0.32(00)	16.28(03)	2.09(00)	0.04(00)	0.94(01)	1.70(00)	4.16(02)	0.12(00)	5.17(01)	0.14(00)	100.00	0.01
ELT27	50.40(02)	2.11(00)	15.48(01)	9.72(01)	0.15(00)	6.98(01)	7.43(02)	3.23(01)	1.12(00)	2.64(00)	0.12(00)	99.38	0.05
GSP-2	66.48(01)	0.67(00)	14.93(01)	4.91(01)	0.04(00)	0.97(00)	2.08(00)	2.81(02)	0.29(00)	5.39(01)	0.15(00)	98.73	n/a
AGV-2	60.14(02)	1.05(01)	17.16(02)	6.76(01)	0.10(00)	1.80(01)	5.24(02)	4.23(03)	0.48(00)	2.92(01)	0.13(00)	100	n/a
BHVO-2	49.84(03)	2.71(00)	13.54(01)	12.23(03)	0.17(00)	7.20(00)	11.32(01)	2.20(01)	0.26(00)	0.51(00)	0.01(00)	100	n/a
BHVO-2 d	49.71(01)	2.67(01)	13.73(02)	12.11(02)	0.17(00)	7.19(02)	11.43(01)	2.22(01)	0.25(00)	0.50(00)	0.01(00)	100	n/a

Table 1. (cont.)

Sample	Dist. along transect (m)	δ^{56}Fe (‰)	2s	*n*	Zone
PV transect	Bearing:	270°			
PV-1	0	0.32	0.01	2	GZ miarolytic granite
PV-2	249.0	0.18	0.11	2	GZ miarolytic granite
PV-3	507.0	0.19	0.02	2	GZ felsic border granite
PV-4	803.0	0.29	0.05	2	GZ transitional granite
PV-5	994.0	0.16	0.03	2	HZ qtz-monzodiorite
PV-6	1162.0	0.12	0.02	2	HZ qtz-monzonite
PV-7	1226.0	0.09	0.08	4	HZ qtz-monzonite
PV-8	1237.0	0.13	0.05	6	HZ qtz-monzodiorite
PV-9	1351.0	0.13	0.02	2	HZ qtz-monzonite
PV-10	1351.0	0.14	0.05	4	HZ qtz-monzonite
ELT transect	Bearing:	180.1°			
ELT 1	0	0.16	0.01	2	CR schist
ELT 2	126	-0.004	0.004	2	CR gneiss
ELT 3	198	0.18	0.03	3	Felsic dike through CR
ELT 6	359	0.18	0.05	2	CR gneiss
ELT 7	361	0.19	0.04	2	GZ border porphyritic granite
ELT 8	454	0.21	0.04	2	GZ transitional granite
ELT 10	652	0.20	0.01	2	mafic dike in trans. Gran.
ELT 11	812	0.33	0.05	2	GZ transitional granite
ELT 12	918	0.18	0.02	2	GZ transitional granite
ELT 13	1008	0.26	0.02	2	GZ transitional granite
ELT 14	1168	0.17	0.16	2	GZ cumulate granite
ELT 15	1273	0.20	0.02	2	GZ cumulate granite
ELT 16	1431	0.18	0.03	2	GZ cumulate granite
ELT 18	1620	0.14	0.02	2	GZ cumulate granite
ELT 19	1723	0.10	0.01	2	HZ qtz monzodiorite

Table 2. Samples from transects within Aztec Wash reporting their δ56Fe values, which represents the average, corrected value. Also included here is the number of analyses of each sample n, the 2s for iron analyses, the distance along the transect, the SiO2 wt % of each sample, and sample locations. GZ is short for granite zone; HZ is short for heterogeneous zone.

Sample	Dist. along transect (m)	δ^{56}Fe (‰)	2s	*n*	Zone
ELT 23	2054	0.09	0.01	2	HZ qtz monzodiorite
ELT 24	2168	0.23	0.03	2	HZ granodiorite
ELT 25	2191	0.18	0.11	2	HZ granite
ELT 26	2337	0.13	0.00	2	HZ granodiorite
ELT 27	2347	0.16	0.05	2	HZ gabbro
11-22 transect	Bearing:	160°			
11-22-1	0	-0.01	0.01	2	CR feldspathic quartzite
11-22-2	41	0.17	0.02	2	GZ fels. border granite
11-22-3	80	0.20	0.03	2	GZ trans. Granite
11-22-4	194	0.21	0.06	2	GZ trans. Granite
11-22-5	284	0.32	0.09	2	GZ trans. Granite
11-22-6	360	0.27	0.05	2	GZ trans. Granite
11-22-7	897	0.17	0.00	2	GZ trans. Granite
11-22-8	1006	0.08	0.02	2	mafic dike in GZ
11-22-9	1235	0.21	0.04	2	GZ trans. Granite
11-22-10	1434	0.14	0.03	2	GZ cumulate
11-22-11	1674	0.13	0.01	2	GZ cumulate
11-22-12	1985	0.14	0.04	2	GZ cumulate
11-22-13	1985	0.21	0.04	2	GZ cumulate
11-22-14	2273	0.06	0.01	2	HZ qtz-monzodiorite
11-22-16	2389	0.14	0.02	2	HZ qtz-monzodiorite
11-22-17	2389	0.28	0.02	2	HZ aplite
11-22-18	2389	0.16	0.02	2	HZ qtz-monzodiorite
11-22-15	2442	0.14	0.01	2	HZ qtz-monzonite
11-22-20	2740	0.30	0.01	2	GZ cumulate granite
11-22-21	2854	0.10	0.01	2	HZ qtz-monzodiorite
11-22-22	2854	0.13	0.00	2	HZ granodiorite
11-22-23	3041	0.17	0.05	2	HZ qtz-monzonite
11-22-24	3041	0.16	0.02	2	HZ gabbro
11-20 transect					
11-20-1	0	0.10	0.02	2	HZ qtz-monzonite layer
11-20-2	1.5	0.08	0.01	2	HZ qtz-monzonite layer
11-20-3	2.5	0.15	0.03	2	HZ qtz-monzonite layer
11-20-5	4	0.15	0.03	2	HZ qtz-monzonite layer
11-20-6m	6	0.08	0.04	2	HZ intermediate enclave
11-20-7	7				contact
11-20-8	8	0.08	0.02	2	HZ qtz-monzodiorite layer
11-20-9	9	0.11	0.05	2	HZ qtz-monzodiorite layer

Table2. (cont.)

DISCUSSION

Major elements vs. $\delta^{56}Fe$

Small variations in $\delta^{56}Fe$ occur with change in SiO_2 for samples from transects PV, ELT, 11-22 and 11-20 (Figure 10). The small variations in samples from AW, while possibly conforming to the global hyperbolic trend (Figure 1), do not provide a robust example of this behavior. Even though the AW samples with SiO_2 greater than 70 wt.% have a heavier average $\delta^{56}Fe$ than those with less silica, most samples do not differ significantly from each other, even at high silica contents. Only a small group of samples with FeO < 1.5 wt.%, and SiO_2 >70 wt.% (Figure 8) have significantly different iron isotope compositions. However, these samples are not unique in their compositions – other samples with similarly high SiO_2 and low FeO contents, have $\delta^{56}Fe$ that are lighter by 0.10‰.

What drives these isotopic variations? Processes such as late stage fluid exsolution and fractional crystallization, both of which would follow Rayleigh distillation curves, have been suggested as potential fractionating processes. After evaluating those two potential mechanisms of iron isotope fractionation, this paper will also consider how spatial variations among the iron isotope ratios may be indicative of the fractionation due to thermal diffusion.

Rayleigh distillation processes as applied to the Aztec Wash dataset

Isotopic fractionation during a Rayleigh distillation process occurs when a product reservoir forms and separates from an initial reservoir, preventing any back-reaction between product and initial pool. The Rayleigh distillation formula is given as

$$\delta^{56}Fe_{product} = (\delta^{56}Fe_{initial} + 1000‰)\, f^{\alpha-1} - 1000‰,$$

where f is the fraction of iron remaining relative to the initial iron content, and α is the fractionation factor, equal to the iron isotope ratio of the product over the ratio of the reactant. Fractional crystallization and fluid exsolution have been proposed as mechanisms that can fractionate iron isotopes and both can be modeled using the Rayleigh distillation equation. By examining the change in $\delta^{56}Fe$ as iron concentration decreases during differentiation, Rayleigh models with different ε (instantaneous fractionation factor, where $\varepsilon \approx 1000 \ln\alpha$) can be made to assess the different processes.

Figure 11 shows the AW $\delta^{56}Fe$ data as a function of the FeO/FeO_i. Here I have used the sample with the highest FeO content (sample ELT 27) as the assumed starting point for subsequent Rayleigh fractionation. Assuming an initial $\delta^{56}Fe$ equivalent to the "mean mafic earth" value of +0.09‰ (Beard et al., 2003), the data increase in $\delta^{56}Fe$ with decreasing FeO/FeO_i, consistent with the trend seen in previously published data (Figure 1). A forward model with an $\varepsilon = -0.05$‰ provides an adequate though imperfect model of the data. For reference, two other models, with $\varepsilon = +0.18$‰ and $= +0.12$‰ are shown, illustrating that a positive fractionation factor results in $\delta^{56}Fe$ evolution opposite to the observed data (see discussion below).

1) In the case of fractional crystallization, as Fe-bearing minerals, such as magnetite, fayalite, pyroxene, amphibole and biotite, crystallize from a melt, they may mechanically separate from the melt. If iron isotopes partition between melt and crystal phases with an equilibrium fractionation factor, the isotope ratio of the melt will change.

As mentioned previously, magnetite is thought to play the major role in controlling the iron isotopic evolution of differentiating magmas. This is because it is the major Fe^{3+}-bearing phase, and, of phases removed during calc-alkaline differentiation (as evidenced by samples on AFM diagram, Figure 12), it contains the most iron. At AW, magnetite is present in rocks, and

based on a typical fractional crystallization model, accounts for 70% of the iron removed from the melt. In order to evaluate the fractionation of iron isotope ratios caused by fractional crystallization, I estimated the fractionation factor between iron bearing minerals and melt. The fractionation factor between magnetite and melt ($\varepsilon^{56}_{\text{Magnetite-Melt}}$) is less than the $\varepsilon^{56}_{\text{Magnetite-Fayalite}}$ = +0.18‰ (Shahar et al., 2008) because melt contains some Fe^{3+} as opposed to Fayalite, which only contains Fe^{2+}. Given the typical Fe^{3+} content of melts, I used $\varepsilon^{56}_{\text{Magnetite-Melt}}$ = +0.12 ‰. Iron-bearing silicate minerals, with their abundance of Fe^{2+}, will have a negative $\varepsilon^{56}_{\text{Fe silicates-Melt}}$. However, since magnetite accounts for the majority of iron removed from the melt, the $\varepsilon^{56}_{\text{Fe minerals-Melt}}$ will still be negative. This results in the δ^{56}Fe of the melt becoming more negative with increasing extent of differentiation. This is the opposite of what is observed in the AW dataset – as the rocks become more evolved, the δ^{56}Fe becomes larger in the positive direction (Figure 11). However, this is an approximation, and in order to fully evaluate fractional crystallization as the mechanism behind the fractionation of iron isotopes in igneous rocks, the fractionation factors between other iron-bearing minerals and melt need to be determined.

2) Exsolution of magmatic volatiles during differentiation has also been proposed as a potential mechanism for fractionating iron isotopes (Heimann et al., 2008; Poitrasson and Freydier, 2005). The $\varepsilon^{56} = -0.05$‰ calculated using the AW dataset can be used to evaluate isotopic fractionation caused by fluid exsolution (Figure 11). This is consistent with theory, that the exsolved volatiles would contain Fe^{2+} and therefore be enriched in light isotopes relative to the melt. Experiments conducted by Bilenker et al. (2012) show that a fluid is lighter than co-existing magnetite and melt. Thus removal of a fluid will produce a negative fractionation factor, and is consistent with the trend seen in δ^{56}Fe of the AW dataset. However, in order to fractionate iron isotopes to δ^{56}Fe = 0.30‰, as seen in the AW data, nearly all of the iron would have to be

removed from the system by removal in the exsolved fluid. The probability of this occurring, is very low, due to the fact that iron would also enter into mineral phases as well. If only 30% of iron was removed from the melt by exsolved volatiles, then in order to get the net change in δ^{56}Fe seen in the AW data, then the $\varepsilon^{56}_{30\%\ fluid-Melt} \approx -0.15‰$. If 10% of the iron was removed with an exsolved vapor or fluid phase, then the $\varepsilon^{56}_{10\%\ fluid-Melt} \approx -0.50‰$ would be required in order to obtain the net change in δ^{56}Fe that occurs in the AW data.

Contamination by country rock

Previous literature has cited country rock assimilation as a potential driver behind fractionated iron isotopes in igneous rocks (Schoenberg and von Blanckenburg, 2006). An isotopically heavy assimilant, they proposed, could drive the magma's iron isotope ratios to higher values. However, country rock samples measured in this study indicate a low δ^{56}Fe. The country rock samples range from δ^{56}Fe = 0.00 - 0.18‰, with an average δ^{56}Fe = 0.08‰ and a 2s = ± 0.20‰ (Table 2). This is nearly half the value of the heaviest intrusive AW samples. If anything, incorporation of country rock into the AW magma would actually drive the iron isotope ratios to lower values. In the context of the transects where the heaviest δ^{56}Fe values occur near the boundary with country rock, it is clear that crustal contamination is not responsible for the iron isotope ratio variations within the AW pluton.

Assessing thermal diffusion processes through spatial transects in Aztec Wash

While fluid exsolution and fractional crystallization may not explain the observed data, the spatial transect data allows for some assessment of whether thermal diffusion processes may produce the iron isotopic variations observed in AW. The incremental emplacement model of pluton formation would create temperature gradients within the intrusion, and thermal migration

predicts that within the temperature gradients, differentiation as well as thermal diffusion would occur, leading to isotopic and compositional trends with spatial position. The two paleohorizontal and the paleovertical transects show variations in iron isotope ratios with changing position.

The two paleohorizontal transects (ELT and 11-22) show increasing $\delta^{56}Fe$ trends within the outer ~500m of the pluton, within the granite zone subunits of the border porphyritic granite, the felsic border granite, and the transitional granite. Near the margin of the pluton the AW samples have low $\delta^{56}Fe$, but as the transects progress into the transitional granite, there is an overall increase by +0.15‰. This is significant in that it may be evidence for the presence of a sustained temperature gradient between the cold country rock and incoming melt. It also shows that the isotopic signature is not coming from the country rock but rather could be related to relative position from the contact.

The largest $\delta^{56}Fe$ of the near-paleovertical PV transect occur near the edge of the pluton within the granite zone, similar to the two paleohorizontal transects (ELT and 11-22). Samples from the heterogeneous zone have lower $\delta^{56}Fe$ values than those from the granite zone subunits. This trend of decreasing $\delta^{56}Fe$ with increasing pluton depth is consistent with formation via thermal migration zone refining. Essentially, as new intrusions are added to the base of a pluton, temperature gradients drive compositional changes and isotopic variations consistent with what is seen in this transect – primarily, the outer colder edge of the intrusion becomes more enriched in silica and heavy iron isotopes relative to the inner region of the pluton (Lundstrom, 2009). The presence of noise within the $\delta^{56}Fe$ variations along the transect may be indicative of an imperfect top-down formation process.

The 11-20 transect, represents a paleovertical transect across a contact between a layer of quartz-monzonite and a layer of biotite-rich monzodiorite. Despite their compositional differences (Table 1), including a 10 wt.% difference in silica, the samples show no significant variations in $\delta^{56}Fe$ amongst themselves, and fall within the "mean mafic-earth" value of $\delta^{56}Fe_{IRMM\text{-}14} = 0.09 \pm 0.10‰$ (Beard et al., 2003; Dauphas and Rouxel, 2006). This may be an important observation in that it shows $\delta^{56}Fe$ is not necessarily a simple reflection of silica content. In regards to testing the model of Lundstrom (2009), this isotopic invariance is consistent with expectation since further intrusions below this location (if AW does form in a top-down process) will erase any signature that might have come during the emplacement of these layers. One way to further expand on this could be to investigate the iron isotope ratios of mineral separates from this transect for any changes across the contact. In addition, more transects similar to 11-20 could be conducted to see if there are any definite trends in iron isotopes across contacts. The addition of high-silica intrusives adjacent to mafic rocks could provide more information illuminating iron isotope distributions across contacts.

In trying to interpret the meaning behind the iron isotope values of samples from Aztec Wash, it is important to keep in mind the formational history of the pluton. Zonation of accessory minerals is indicative of fluctuating conditions (Cates, 2003), and truncated surfaces found in zircons may point to five possible dissolution events (Robinson and Miller, 1999). These dissolution events, indicating changes in composition or temperature of the host magma, could be related to injections of magma, supporting the idea of formation via incremental emplacement. Field observations of compositionally-variable layers stacked on top of each other within both the heterogeneous zone and the granite zone also indicate that multiple intrusions likely played a role in forming AW.

Injections of new magma will create temperature gradients within intrusive systems, and isotopic fractionation by thermal diffusion should occur. However, in order to see significant thermal diffusion driven isotopic variations, temperature gradients have to be maintained over a period of time significantly longer than what a single injection could sustain (Lundstrom, 2009). The theoretical model is that incremental injection occurs such that the top down accumulation rate of rock in the pluton occurs in a near steady state rate of 1mm/year. However, magma injections are likely to be much more random, and while long-term averages may be 1mm/year, short term fluctuations may be much greater, causing variations in the isotopic composition.

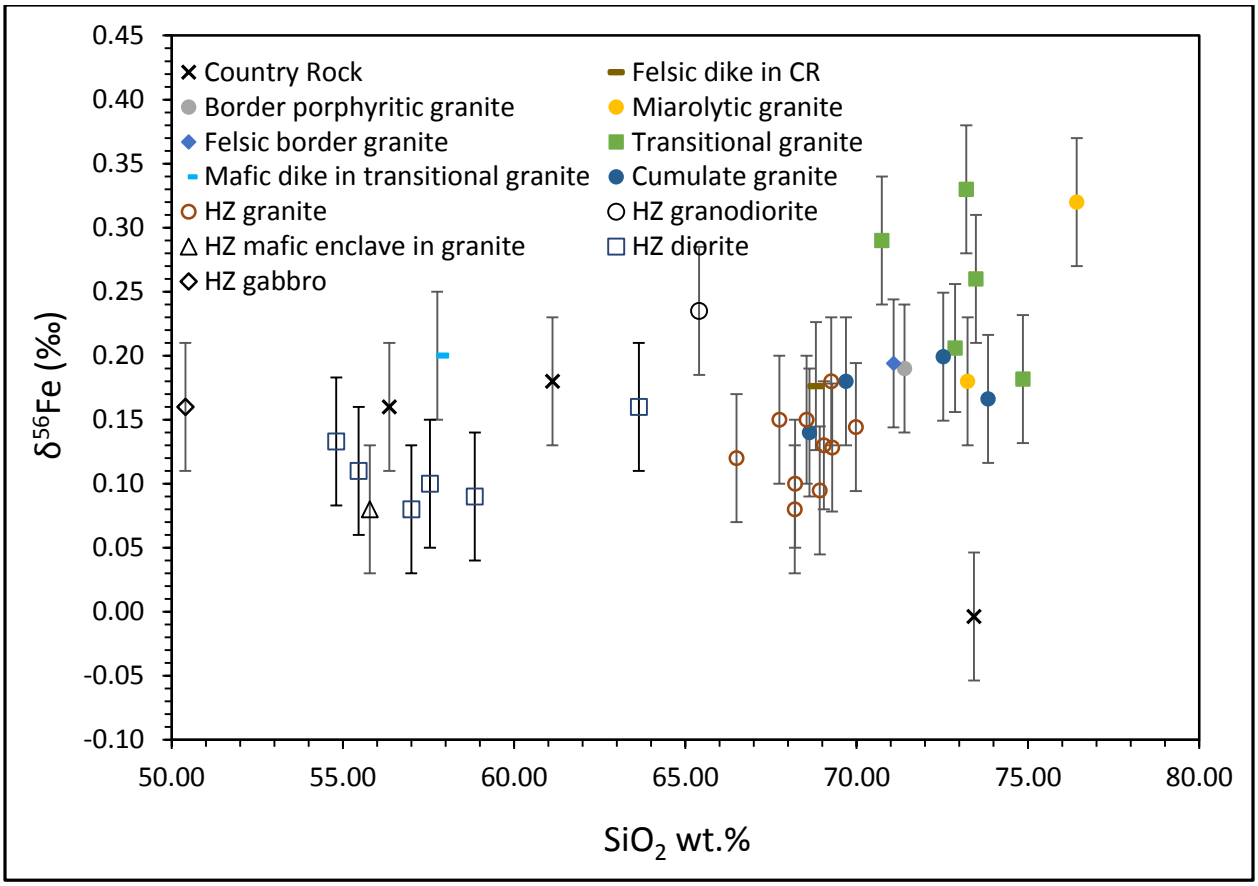

Figure 10. Plot of $\delta^{56}Fe$ vs. SiO_2 of samples from transects PV, ELT, and 11-20. X's are samples of country rock, the solid shapes represent the sub-units of the granite zone, and the open shapes are representative of the lithologies within the heterogeneous zone. The data show that samples with high silica content (>70%) tend to have higher $\delta^{56}Fe$. Error bars represent the external reproducibility of 0.06‰. .

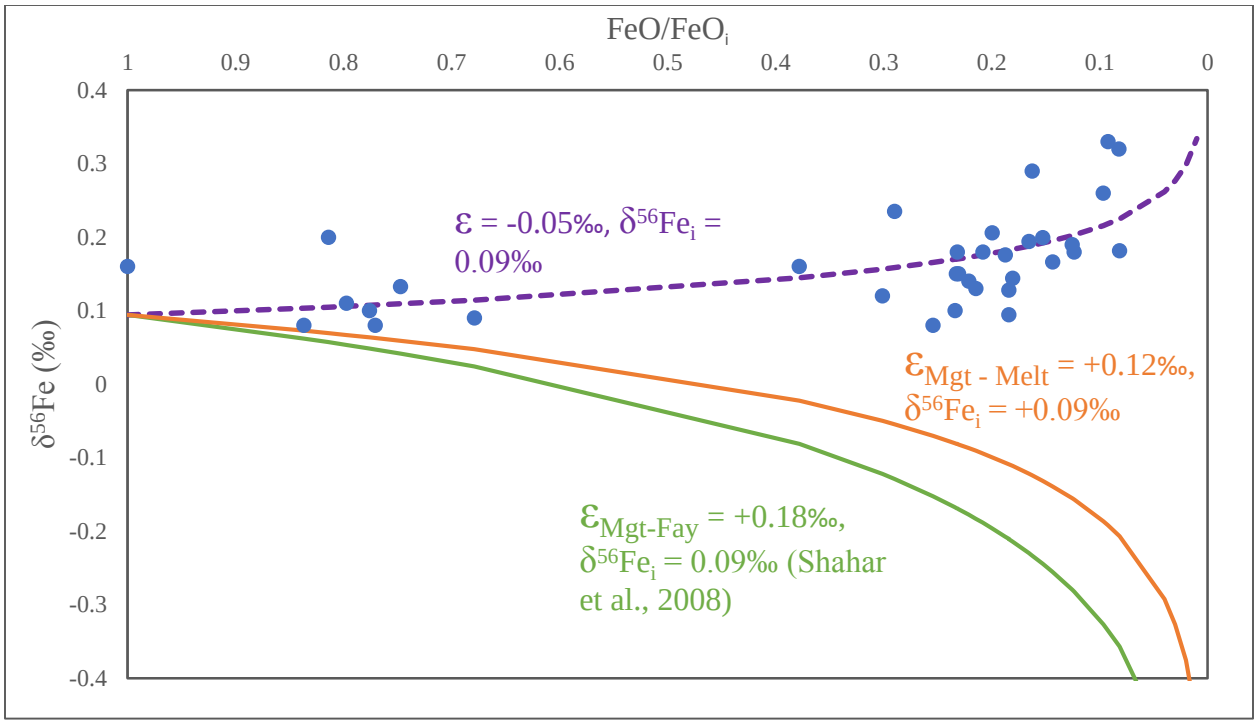

Figure 11. Rayleigh fractionation models using different ε values to model the trend between δ^{56}Fe and the fraction of FeO remaining over the initial FeO. The purple line represent ε = −0.05‰, calculated using the sample data. The initial δ^{56}Fe = +0.09‰, was assumed based on mean mafic earth value (Beard, et al., 2003). The green line shows the trend determined by Shahar et al. (2008), who determined $\varepsilon_{Magnetite-Melt}$ = +0.18‰. This value can be used to approximate the fraction factor between magnetite and a coexisting melt, $\varepsilon_{Magnetite-Melt}$ = +0.12‰. This fractionation factor results in a trend opposite that seen in the AW dataset, as well as that of previously published values (Fig. 1). Specifically, as rocks become more differentiated, their δ^{56}Fe values increase. The purple line represents the Rayleigh distillation model for fluid exsolution, with a fractionation factor of −0.05‰ between the exsolved fluid and melt. This trend approximately predicts direction of iron isotope fractionation. However, it requires 100% of iron to be removed via the melt in order to obtain the highly fractionated values of ~0.3‰ seen in some of the AW samples.

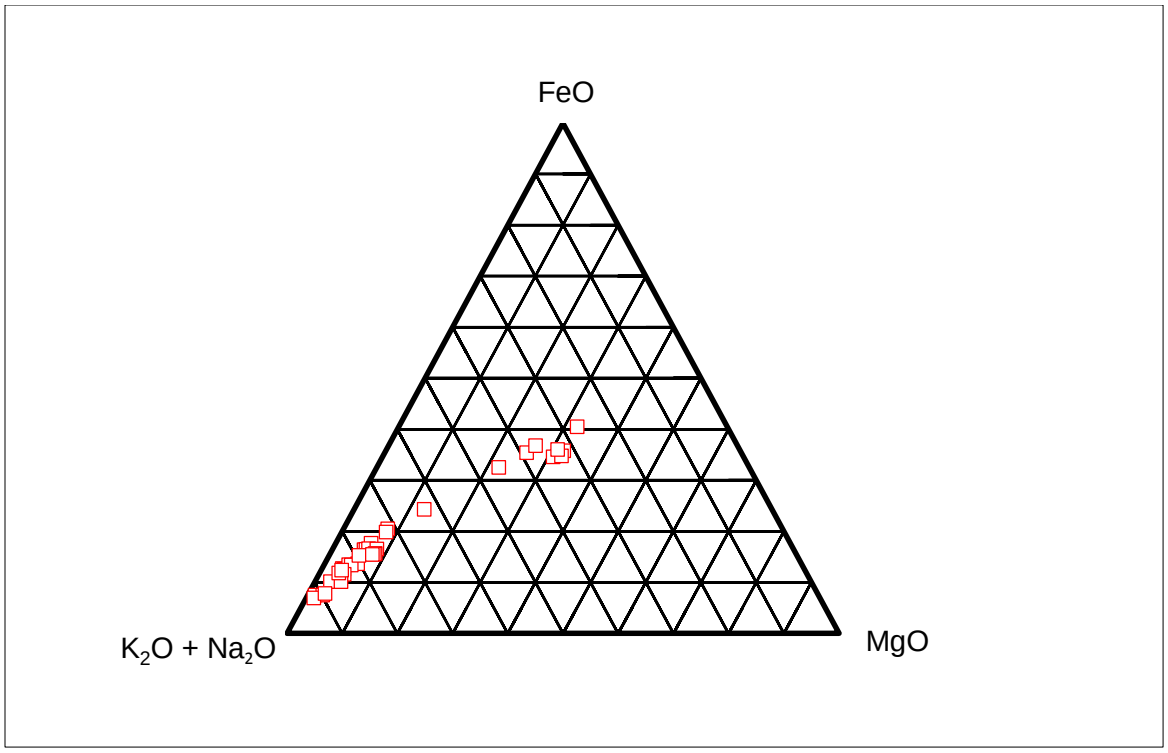

Figure 12. Alkalis-FeO-MgO ternary diagram with AW samples plotted (country rocks samples are excluded). The linear trend of data corresponds to a calc-alkaline evolution trend.

CONCLUSIONS

This project reports some of the first iron isotope ratios collected from a single pluton with focus on detailed spatial position of samples within an intrusive system. Significant iron isotope ratio variations occur in the pluton and these were assessed in the context of existing proposals for mechanisms causing iron isotope variations in igneous rocks.

Intrusive samples from AW ranged in δ^{56}Fe from +0.06 − +0.33‰. The iron isotope ratios correlate with silica content in that samples with higher silica content tend to have higher in δ^{56}Fe values. There are some exceptions to this trend, however, and these exceptions occur primarily in the heterogeneous zone. Spatial trends in iron isotope distribution have been found as well. The two paleohorizontal transects show significant increases in δ^{56}Fe from the country rock contact into the first ~500m of the transect. The paleovertical transect at the top of the pluton has an overall trend of decreasing δ^{56}Fe from the silica-rich miarolytic granite unit at the top of the pluton downwards into the heterogeneous zone. A short paleovertical transect within unknown relative position in the lower portion shows no significant δ^{56}Fe variation.

Comparison of Rayleigh distillation models for fractional crystallization and fluid exsolution allow assessment of these mechanisms as applied to the AW iron isotope ratio trends. Using existing fractionation factors for magnetite and melt, the trend in δ^{56}Fe with decreasing FeO content is not consistent with models of fractional crystallization. If other iron-bearing minerals and melt have opposing fractionation factors, it could work. These fractionation factors have yet to be determined. Fluid exsolution remains a viable model given recent experimental determinations, but these models must be reconciled with our understanding of how iron contents change during differentiation.

Spatial transect data show mixed results for isotopic fractionation of iron due to thermal diffusion. However, some of the results could be evidence of isotopic fractionation due to a

sustained temperature gradient, in particular the observation of increasingly higher $\delta^{56}Fe$ within the first 500m of the paleohorizontal transects. On the other hand, $\delta^{56}Fe$ variations are small, and random variability within the interior of the pluton shows that these variations are not easily interpreted. In order to further test this model, isotopes of another non-traditional stable element should be investigated for similar trends. Silicon would be particularly fitting because it lacks multiple valence states in melts, so any resulting isotopic fractionation of silicon could not be attributed to processes based on changes in valence state, such as fluid exsolution and fractional crystallization.

References

Beard, B. L., Johnson, C. M., Cox, L., Sun, H., Nealson, K. H., & Aguilar, C. (1999). Iron isotope biosignatures. *Science*, *285*(5435), 1889-1892.

Beard, B.L., Johnson, C.M., Skulan, J.L., Nealson, K.H., Cox, L., Sun, H. (2003) Application of Fe isotopes to tracing the geochemical and biological cycling of Fe. *Chemical Geology* 195 (1–4), 87–117.

Bergquist, B. A., & Boyle, E. A. (2006). Iron isotopes in the Amazon River system: Weathering and transport signatures. *Earth and Planetary Science Letters*, 248(1), 54-68.

Bilenker L.D., Simon A., Lundstrom C., Gajos N. (2012) Iron isotope fractionation among magnetite, pyrrhotite, chalcopyrite, rhyolite melt and aqueous fluid at magmatic-hydrothermal conditions. *Abstract A.G.U. Fall Meeting 2012*, abstract #11A-2734.

Bindeman, I. N., Lundstrom, C. C., Bopp, C., & Huang, F. (2013). Stable isotope fractionation by thermal diffusion through partially molten wet and dry silicate rocks. *Earth and Planetary Science Letters*, 365, 51-62.

Braun, D. & Libchaber, A. (2004) Thermal force approach to molecular evolution. *Phys. Biol*. 1, 1–8.

Candela, P. A. (1986). The evolution of aqueous vapor from silicate melts: effect on oxygen fugacity. *Geochimica et Cosmochimica Acta*, *50*(6), 1205-1211.

Cates, N.L. (2003) Perspectives on the development of an intermediate, open-[system magma chamber: Aztec Wash pluton, Nevada. Masters thesis, Vanderbilt University, Nashville, TN, 162 p.

Cates, N.L., Miller, J.S., Miller, C.F., Wooden, J.L., Eriksen, S., Means, M. (2003) Longevity of plutonic systems: SHRIMP evidence from Aztec Wash and Searchlight plutons, Nevada. *Geological Society of America, abstracts with programs* 35, v.4, 63.

Coleman, D. S., Gray, W. and Glazner, A. F. (2004) Rethinking the emplacement and evolution of zoned plutons: geochronologic evidence for incremental assembly of the Tuolumne Intrusive Suite, California. *Geology* 32, 433–436.

Dauphas, N., & Rouxel, O. (2006). Mass spectrometry and natural variations of iron isotopes. *Mass Spectrometry Reviews*, *25*(4), 515-550.

Dixon, P. R., Janecky, D. R., Perrin, R. E., Rokop, D. J., Unkefer, P. L., & Spal, W. D. (1992). Unconventional stable isotopes: Iron. *Water-Rock Interaction*, *2*, 915-918.

Faulds, J.E., Feuerbach, D.L., Miller, C.F., Smith, E.I. (2001) Cenozoic evolution of the northern Colorado River extensional corridor, southern Nevada and northwest Arizona: *Pacific Section of the Am. Assoc. Pet. Geol. Pubs*. GB, v.78, 239-272.

Furry, W. H., Jones, R. C. and Onsager, L. (1939) On the theory of isotope separation by thermal diffusion. *Physical Review*. 55, 1083–1095.

Gajos, N. (2014) Spatially controlled Fe isotope variations at Torres Del Paine. Masters thesis, University of Illinois, Champaign-Urbana, IL.

Glazner, A. F., Bartley, J. M., Coleman, D. S., Gray, W. and Taylor, R. Z. (2004) Are plutons assembled over millions of years by amalgamation from small magma chambers? *GSA Today* 14, 4– 7.

Harper, B.E., Miller, C.F., Koteas, G.C., Cates, N.L., Wiebe, R.A., Lazzareschi, D.S., Cribb, J.W. (2004) Granites, dynamic magma chamber processes, and pluton construction: Aztec Wash pluton, Eldorado Mountains, Nevada, USA. *Trans. Royal Soc. Edinburgh. Earth Sciences* 95, 277–296.

Heimann, A., Beard, B. and Johnson, C. (2008) The role of volatile exsolution and sub-solidus fluid/rock interactions in producing high 56Fe/54Fe ratios in siliceous igneous rocks. *Geochim. Cosmochim. Acta* 72, 4379–4396.

Huang F., Lundstrom C. C., Ianno A. J., Boudreau A. E., Li J., Ferre´ E. C., Marshak S. and DeFrates J. (2009) Thermal migration in wet andesite: experiments and models suggesting a new mechanism of magma differentiation. *Geochim. Cosmochim. Acta* 73, 729–749.

Huang, F., Chakraborty, P., Lundstrom, C. C., Holmden, C., Glessner, J. J. G., Kieffer, S. W., & Lesher, C. E. (2010). Isotope fractionation in silicate melts by thermal diffusion. *Nature*, *464*(7287), 396-400.

Huang, F., Zhang, Z., Lundstrom, C. C., & Zhi, X. (2011). Iron and magnesium isotopic compositions of peridotite xenoliths from Eastern China. *Geochimica et Cosmochimica Acta*, 75(12), 3318-3334.

Kapp, J. D. A., Miller, C. F., & Miller, J. S. (2002). Ireteba Pluton, Eldorado Mountains, Nevada: Late, Deep-Source, Peraluminous Magmatism in the Cordilleran Interior. *The Journal of geology*, *110*(6), 649-669.

Kyser, T. K., Lesher, C. E., & Walker, D. (1998). The effects of liquid immiscibility and thermal diffusion on oxygen isotopes in silicate liquids. *Contributions to mineralogy and petrology*, *133*(4), 373-381.

Lesher, C. E., & Walker, D. (1986). Solution properties of silicate liquids from thermal diffusion experiments. *Geochimica et Cosmochimica Acta*, *50*(7), 1397-1411.

Lesher, C. E., & Walker, D. (1988). Cumulate maturation and melt migration in a temperature gradient. *Journal of Geophysical Research: Solid Earth (1978–2012)*, *93*(B9), 10295-10311.

Lundstrom, C. (2009) Hypothesis for the origin of convergent margin granitiods and Earth's continental crust by thermal migration zone refining: *Geochim. Cosmochim. Acta*, v.73, 5709-5729.

Lundstrom, C. (in prep) Phase-equilibrium control on silicic igneous rock petrogenesis: the case for a ubiquitous low temperature melt in Earth's upper crustal magmatic systems

Matzel J. E. P., Bowring S. A. and Miller R. B. (2006) Time scales of pluton construction at differing crustal levels; examples from the Mount Stuart and Tenpeak Intrusions, north Cascades, Washington. *Geol. Soc. Am. Bull*. 118, 1412–1430.

Miller, C.F., Furbish, D.J., Walker, B.A., Claiborne, L.L., Koteas, G.C., Bleick, H.A., and Miller, J.S. (2011) Growth of plutons by incremental emplacement of sheets in crystal rich host: Evidence of Miocene intrusions of the Colorado River Region, Nevada, USA: *Tectonophysics*, v.500, 65-77.

Miller, C.F., and Miller, J.S. (2002) Contrasting stratified plutons exposed in tilt blocks, Eldorado Mountains, Colorado River Rift, NV, USA: *Lithos*, v.61, 209-224.

Ott, A. (1969). Isotope separation by thermal diffusion in liquid metal. *Science*, *164*(3877), 297-297.

Poitrasson, F., Halliday, A.N., Lee, D.C., Levasseur, S., Teutsch, N. (2004). Iron isotope differences between Earth, Moon, Mars and Vesta as possible records of contrasted accretion mechanisms. *Earth Planet. Sci. Lett*. 223, 253–266.

Poitrasson, F. and Freydier, R. (2005). Heavy iron isotope composition of granites determined by high resolution MC-ICP-MS. *Chemical Geolology*. 222, 132–147.

Pollock, M., Edwards, B., Hauksdóttir, S., Alcorn, R., & Bowman, L. (2014). Geochemical and lithostratigraphic constraints on the formation of pillow-dominated tindars from Undirhlíðar quarry, Reykjanes Peninsula, southwest Iceland. *Lithos*, *200*, 317-333.

Polyakov, V. B. (1997). Equilibrium fractionation of the iron isotopes: Estimation from Mössbauer spectroscopy data. *Geochimica et cosmochimica acta*, *61*(19), 4213-4217.

Polyakov, V. B., & Mineev, S. D. (2000). The use of Mössbauer spectroscopy in stable isotope geochemistry. *Geochimica et Cosmochimica Acta*, *64*(5), 849-865.

Reith, D., & Müller-Plathe, F. (2000). On the nature of thermal diffusion in binary Lennard-Jones liquids. *The Journal of Chemical Physics*, *112*(5), 2436-2443.

Richter, F. M., Watson, E. B., Mendybaev, R. A., Teng, F. Z., & Janney, P. E. (2008). Magnesium isotope fractionation in silicate melts by chemical and thermal diffusion. *Geochimica et Cosmochimica Acta*, 72(1), 206-220.

Savage, P. S., Georg, R. B., Williams, H. M., Burton, K. W., & Halliday, A. N. (2011). Silicon isotope fractionation during magmatic differentiation. Geochimica et Cosmochimica Acta, 75(20), 6124-6139.

Schauble, E. A., Rossman, G. R., & Taylor Jr, H. P. (2001). Theoretical estimates of equilibrium Fe-isotope fractionations from vibrational spectroscopy. *Geochimica et Cosmochimica Acta*, *65*(15), 2487-2497.

Schoenberg, R., & von Blanckenburg, F. (2005). An assessment of the accuracy of stable Fe isotope ratio measurements on samples with organic and inorganic matrices by high-resolution multicollector ICP-MS. International Journal of Mass Spectrometry, 242(2), 257-272.

Schoenberg, R. and Blanckenburg, F. v. (2006) Modes of planetary-scale Fe isotope fractionation. Earth Planet. Sci. Lett. 252, 342– 359.

Schuessler, J.A., Schoenberg, R., Sigmarsson, O. (2009) Iron and lithium isotope systematics of the Hekla volcano, Iceland – Evidence for Fe isotope fractionation during magma differentiation. Chem. Geol. 258, 78-91.

Severinghaus, J. P., Grachev, A. and Battle, M. (2001) Thermal fractionation of air in polar firn by seasonal temperature gradients. Geochim. Geophys, Geosys. 2.

Shahar, A., Young, E. D., & Manning, C. E. (2008). Equilibrium high-temperature Fe isotope fractionation between fayalite and magnetite: an experimental calibration. *Earth and Planetary Science Letters*, *268*(3), 330-338.

Smith, J. N. (2011) Incorporation of host rock blocks during the Growth of the Aztec Wash Pluton, Eldorado Mountains, Nevada. Masters Thesis: San Jose State University, San Jose, Ca. 172 p.

Sossi, P.A., Foden, J.D., Halverson, G.P. (2012) Redox-controlled iron isotope fractionation during magmatic differentiation: an example from the Red Hill intrusion, S. Tasmania. Contrib. Mineral Petrol. 164, 757-772.

Teng, F. Z., Dauphas, N., Huang, S., & Marty, B. (2013). Iron isotopic systematics of oceanic basalts. Geochimica et Cosmochimica Acta, 107, 12-26.

Völkening, J., & Papanastassiou, D. A. (1989). Iron isotope anomalies. *The Astrophysical Journal*, *347*, L43-L46.

Walker, D., Jurewicz, S., & Watson, E. B. (1988). Adcumulus dunite growth in a laboratory thermal gradient. *Contributions to Mineralogy and Petrology*, *99*(3), 306-319.

Weyer, S., Anbar, A. D., Brey, G. P., Münker, C., Mezger, K., & Woodland, A. B. (2005). Iron isotope fractionation during planetary differentiation. *Earth and Planetary Science Letters*, *240*(2), 251-264.

Wiebe, R. A., and Collins, W. J. (1998). Depositional features and stratigraphic sections in granitic plutons: implications for the emplacement and crystallization of granitic magma. *Journal of Structural Geology*, *20*(9), 1273-1289.

Zambardi, T., Lundstrom, C. C., Li, X., & McCurry, M. (2014). Fe and Si isotope variations at Cedar Butte volcano; insight into magmatic differentiation. *Earth and Planetary Science Letters*, *405*, 169-179.

Zhu, X. K., Guo, Y., O'Nions, R. K., Young, E. D., & Ash, R. D. (2001). Isotopic homogeneity of iron in the early solar nebula. *Nature*, *412*(6844), 311-313.

APPENDIX A. Sample data

Sample	Transect	Unit	Latitude	Longitude	Notes
11-17-1	11-17	Heterogeneous zone	N 35 39' 20.7"	W 114 46' 14.8"	
11-17-2	11-17	Heterogeneous zone	-	-	
11-17-3	11-17	Heterogeneous zone	-	-	
11-17-6	11-17	Heterogeneous zone	N 35 39' 35.6"	W 114 46' 24.7"	
11-17-9a	11-17	Heterogeneous zone	N 35 39' 34.6"	W 114 46' 23.0"	
11-17-9b	11-17	Heterogeneous zone	N 35 39' 34.6"	W 114 46' 23.0"	
11-17-10	11-17	Heterogeneous zone	N 35 39' 35.0"	W 114 46' 22.1"	
11-17-12	11-17	Granite zone	N 35 39' 33.7"	W 114 46' 17.0"	
11-17-13	11-17	Granite zone	N 35 39' 33.6"	W 114 46' 13.5"	
PV-1	PV	Granite zone miarolytic granite	35°39'38.64"N	114°45'34.74"W	Fmly AT 1b
PV-2	PV/11-17	Granite zone miarolytic granite	35°39'39.00"N	114°45'44.40"W	Frmly 11-17-15
PV-3	PV	Granite zone felsic border granite	35°39'34.58"N	114°45'55.09"W	Frmly AT 4
PV-4	PV/11-17	Granite zone transitional granite	35°39'34.40"N	114°46'6.70"W	Frmly 11-17-14
PV-5	PV	Heterogeneous zone qtz-monzodiorite	35°39'32.70"N	114°46'14.81"W	Frmly AT3
PV-6	PV/11-17	Heterogeneous zone qtz-monzonite	35°39'35.20"N	114°46'20.90"W	Frmly 11-17-11
PV-7	PV/11-18	Heterogeneous zone qtz-monzonite	35°39'34.50"N	114°46'23.50"W	Frmly 11-17-8
PV-8	PV/11-19	Heterogeneous zone qtz-monzodiorite	35°39'35.5"N	114°46'23.90"W	Frmly 11-17-7
PV-9	PV/11-20	Heterogeneous zone qtz-monzonite	35°39'36.9"N	114°46'27.70"W	Frmly 11-17-5
PV-10	PV/11-21	Heterogeneous zone qtz-monzonite	35°39'36.9"N	114°46'27.7"W	Frmly 11-17-4
ELT 1	ELT	CR schist	35°40'25.41"N	114°46'15.96"W	Frmly Worm 11
ELT 2	ELT	CR gneiss	35°40'21.28"N	114°46'17.29"W	Frmly Worm 10
ELT 3	ELT	Felsic dike through CR	35°40'18.93"N	114°46'16.39"W	Frmly Worm 9
ELT 4	ELT	CR gneiss	35°40'18.93"N	114°46'16.39"W	Frmly Worm 8
ELT 5	ELT	Felsic in CR			Frmly Worm 7
ELT 6	ELT	CR gneiss	35°40'16.25"N	114°46'15.89"W	Frmly Worm 6
ELT 7	ELT	Granite zone border porphyritic granite	35°40'15.17"N	114°46'16.18"W	Frmly Worm 5
ELT 8	ELT	Granite zone transitional granite	35°40'13.74"N	114°46'15.37"W	Frmly Worm 4
ELT 9	ELT	Granite zone transitional granite	35°40'13.74"N	114°46'15.37"W	Frmly Worm 3

Table 3. Information regarding samples collected from Aztec Wash Pluton and the surrounding country rock. Includes sample name(s), coordinates and unit. Formerly is abbreviated as Frmly.

Sample	Transect	Unit	Latitude	Longitude	Notes
ELT 10	ELT	mafic dike in granite zone	35°40'13.66"N	114°46'15.38"W	Frmly Worm 2
ELT 11	ELT	Granite zone transitional granite	35°40'10.67"N	114°46'17.98"W	Frmly Worm 1
ELT 12	ELT	Granite zone transitional granite	35°40'7.20"N	114°46'18.20"W	Frmly EPH 2
ELT 13	ELT	Granite zone transitional granite	35°40' 04.3"N	114° 46' 18.1"W	Frmly EPH 3
ELT 14	ELT	Granite zone cumulate granite	35° 39' 59.0"N	114° 46' 15.2"W	Frmly EPH 4
ELT 15	ELT	Granite zone cumulate granite	35° 39' 55.6"N	114° 46' 15.8"W	Frmly EPH 5
ELT 16	ELT	Granite zone cumulate granite	35° 39' 50.5"N	114° 46' 17.3"W	Frmly EPH 6
ELT 17	ELT	Granite zone cumulate granite	35° 39' 47.8"N	114° 46' 18.0"W	Frmly EPH 7
ELT 18	ELT	Granite zone cumulate granite	35° 39' 44.4"N	114° 46' 17.8"W	Frmly EPH 8
ELT 19	ELT	Heterogeneous zone qtz monzodiorite	35° 39' 41.3"N	114° 46' 19.8"W	Frmly EPH 9
ELT 20	ELT	Heterogeneous zone	35° 39' 38.4"N	114° 46' 21.0"W	Frmly EPH 10
ELT 22	ELT	Heterogeneous zone	35° 39' 30.5"N	114° 46' 21.6"W	Frmly EPH 12
ELT 23	ELT	Heterogeneous zone qtz monzodiorite	35° 39' 30.5"N	114° 46' 21.6"W	Frmly EPH 13
ELT 24	ELT	Heterogeneous zone granodiorite	35° 39' 26.7"N	114° 46' 20.5"W	Frmly EPH 14
ELT 25	ELT	Heterogeneous zone granite	35° 39' 25.9"N	114° 46' 19.4"W	Frmly EPH 15
ELT 26	ELT	Heterogeneous zone granodiorite	35° 39' 20.9"N	114° 46' 14.2"W	Frmly EPH 16
ELT 27	ELT	Heterogeneous zone gabbro	35° 39' 21.0"N	114° 46' 11.3"W	Frmly EPH 17
11-22-1	11-22	CR - feldspathic quartzite	35°40'12.20"N	114°51'13.32"W	
11-22-2	11-22	Granite zone fels. border granite	35°40'10.00"N	114°51'11.80"W	
11-22-3	11-22	Granite zone trans. Granite	35°40'9.00"N	114°51'10.90"W	
11-22-4	11-22	Granite zone trans. Granite	35°40'6.20"N	114°51'7.90"W	
11-22-5	11-22	Granite zone trans. Granite	35°40'4.20"N	114°51'5.30"W	
11-22-6	11-22	Granite zone trans. Granite	35°40'1.90"N	114°51'4.30"W	
11-22-7	11-22	Granite zone trans. Granite	35°39'45.40"N	114°50'57.30"W	
11-22-8	11-22	mafic dike in Granite zone	35°39'41.90"N	114°50'56.80"W	
11-22-9	11-22	Granite zone trans. Granite	35°39'34.50"N	114°50'55.90"W	

Table3. (cont.)

Sample	Transect	Unit	Latitude	Longitude	Notes
11-22-10	11-22	Granite zone cumulate	35°39'28.40"N	114°50'53.30"W	
11-22-11	11-22	Granite zone cumulate	35°39'21.20"N	114°50'49.70"W	
11-22-12	11-22	Granite zone cumulate	35°39'13.10"N	114°50'42.30"W	
11-22-13	11-22	Granite zone cumulate	35°39'13.10"N	114°50'42.30"W	
11-22-14	11-22	Heterogeneous zone qtz-monzodiorite	35°39'3.74"N	114°50'39.58"W	
11-22-16	11-22	Heterogeneous zone qtz-monzodiorite	35°39'1.30"N	114°50'35.30"W	
11-22-17	11-22	Heterogeneous zone aplite	35°39'1.30"N	114°50'35.30"W	
11-22-18	11-22	Heterogeneous zone qtz-monzodiorite	35°39'1.2"N	114°50'35.3"W	
11-22-15	11-22	Heterogeneous zone qtz-monzonite	35°38'57.8"N	114°50'39.31"W	
11-22-20	11-22	Granite zone cumulate granite	35°38'49.8"N	114°50'41.35"W	
11-22-21	11-22	Heterogeneous zone qtz-monzodiorite	35°38'51.1"N	114°50'37.90"W	
11-22-22	11-22	Heterogeneous zone granodiorite	35°38'51.1"N	114°50'37.90"W	
11-22-23	11-22	Heterogeneous zone qtz-monzonite	35°38'46.2"N	114°50'33.50"W	
11-22-24	11-22	Heterogeneous zone gabbro	35°38'46.2"N	114°50'33.50"W	
11-20-1	11-20	Heterogeneous zone qtz-monzonite layer	35°38'51.7"N	114°50'33.50"W	
11-20-2	11-20	Heterogeneous zone qtz-monzonite layer	35°38'51.7"N	114°50'33.50"W	
11-20-3	11-20	Heterogeneous zone qtz-monzonite layer	35°38'51.7"N	114°50'33.50"W	
11-20-4	11-20	Heterogeneous zone qtz-monzonite layer	35°38'51.7"N	114°50'33.50"W	
11-20-5	11-20	Heterogeneous zone intermediate enclave	35°38'51.7"N	114°50'33.50"W	
11-20-6f	11-20	Heterogeneous zone qtz monzonite layer	35°38'51.7"N	114°50'33.50"W	
11-20-6m	11-20	Heterogeneous zone qtz-monzodiorite layer	35°38'51.7"N	114°50'33.50"W	
11-20-7	11-20	Contact	35°38'51.7"N	114°50'33.50"W	
11-20-8	11-20	Heterogeneous zone qtz-monzodiorite layer	35°38'51.7"N	114°50'33.50"W	
11-20-9	11-20	Heterogeneous zone	35°38'51.7"N	114°50'33.50"W	
11-20-10	11-20	Heterogeneous zone	35°38'51.7"N	114°50'33.50"W	
11-20-11	11-20	Heterogeneous zone	35°38'51.7"N	114°50'33.50"W	
11-20-12	11-20	Heterogeneous zone	35°38'51.7"N	114°50'33.50"W	
11-20-13	11-20	Heterogeneous zone	35°38'51.7"N	114°50'33.50"W	

Table3. (cont.)

Sample	Transect	Unit	Latitude	Longitude	Notes
11-20-14	11-20	Heterogeneous zone	35°38'51.7"N	114°50'33.50"W	
11-20-15	11-20	Heterogeneous zone	35°38'51.7"N	114°50'33.50"W	
11-20-16	11-20	Heterogeneous zone	35°38'51.7"N	114°50'33.50"W	
11-20-17	11-20	Heterogeneous zone	35°38'51.7"N	114°50'33.50"W	
11-20-18	11-20	Heterogeneous zone	35°38'51.7"N	114°50'33.50"W	
11-20-19	11-20	Heterogeneous zone	35°38'51.7"N	114°50'33.50"W	
11-20-20	11-20	Heterogeneous zone	35°38'51.7"N	114°50'33.50"W	
11-20-21	11-20	Heterogeneous zone	35°38'51.7"N	114°50'33.50"W	
11-20-22	11-20	Heterogeneous zone	35°38'51.7"N	114°50'33.50"W	
11-20-23	11-20	Heterogeneous zone	35°38'51.7"N	114°50'33.50"W	
11-20-24	11-20	Heterogeneous zone	35°38'51.7"N	114°50'33.50"W	
11-20-25	11-20	Heterogeneous zone	35°38'51.7"N	114°50'33.50"W	
11-20-26	11-20	Heterogeneous zone	35°38'51.7"N	114°50'33.50"W	
11-20-27	11-20	Heterogeneous zone	35°38'51.7"N	114°50'33.50"W	
11-21-28	11-20	Heterogeneous zone	35°38'51.7"N	114°50'33.50"W	
11-21-29	11-20	Heterogeneous zone	35°38'51.7"N	114°50'33.50"W	
11-21-30	11-20	Heterogeneous zone	35°38'51.7"N	114°50'33.50"W	
11-21-31	11-20	Heterogeneous zone	35°38'51.7"N	114°50'33.50"W	
11-21-32	11-20	Heterogeneous zone	35°38'51.9"N	114°50'36.50"W	
11-21-33	11-20	Heterogeneous zone	35°38'51.9"N	114°50'36.50"W	
11-21-34	11-20	Heterogeneous zone	35°38'51.9"N	114°50'36.50"W	
11-21-35	11-20	Heterogeneous zone	35°38'51.5"N	114°50'36.6"W	
11-21-36	11-20	Heterogeneous zone	35°38'51.5"N	114°50'36.6"W	
11-21-37	11-20	Heterogeneous zone	35°38'51.5"N	114°50'36.6"W	
11-21-38	11-20	Heterogeneous zone	35°38'51.5"N	114°50'36.6"W	
11-21-39	11-20	Heterogeneous zone	35°38'51.5"N	114°50'36.6"W	
11-21-40	11-20	Heterogeneous zone	35°38'51.5"N	114°50'36.6"W	
11-21-41	11-20	Heterogeneous zone	35°38'51.5"N	114°50'36.6"W	
11-21-42	11-20	Heterogeneous zone	35°38'51.5"N	114°50'36.6"W	
11-21-43	11-20	Heterogeneous zone	35°38'51.5"N	114°50'36.2"W	
11-18-2	-	Heterogeneous zone			
11-18-3	-	Heterogeneous zone			
11-18-4	-	Heterogeneous zone			
11-18-5	-	Heterogeneous zone			
11-18-6	-	Heterogeneous zone			
11-18-7	-	Heterogeneous zone			
11-18-7a	-	Heterogeneous zone			
11-18-7b	-	Heterogeneous zone	35°38'19.1"N	114°50'34.7"W	
11-18-7c	-	Heterogeneous zone	35°38'19.1"N	114°50'34.7"W	

Table 3. (cont)

Sample	Transect	Unit	Latitude	Longitude	Notes
11-18-8	-	Heterogeneous zone	35°38'19.1"N	114°50'34.7"W	
11-18-9	-	Heterogeneous zone			
11-18-10	-	Heterogeneous zone			
11-18-11	-	Heterogeneous zone			

Table 3. (cont)

APPENDIX B. Major element data using SEM EDS and an electron microprobe

Before samples were analyzed at the College of Wooster XRF Lab for major element data, two attempts were made to analyze prepared fusion glasses at the University of Illinois, Urbana-Champaign and Indiana University for analysis using an electron microprobe. The glass preparation procedure and details of analysis are as follows.

Glasses for major element analyses were fused at 1070° for 80 minutes using lithium tetraborate as a flux in a 2:1 ratio. Felsic samples were re-crushed and re-fused to ensure full dissolution of quartz. Glasses were mounted and polished for energy dispersive (EDS) x-ray analyses using the JEOL 840A scanning electron microscope at the Department of Geology, University of Illinois; analyses used a 10 na current and 15 KV accelerating voltage. Standards based analyses used USGS rock standards, Smithsonian mineral standards and full ZAF corrections. Compositions were determined by averaging five standards-based analyses from each glass.

The prepared glasses were also taken to Indiana University for analysis using the Cameca SX50 electron microprobe. Analyses of glasses used a 10 μm beam size, an accelerating voltage of 15kV and a beam current of 5nA. USNM standards of basalt and rhyolite glasses were used for beam calibration and a lithium tetraborate fused glass of USGS AGV-1 standard was used for normalization of sample values.

Sample	Al_2O_3	CaO	FeO	MgO	K_2O	SiO_2	Na_2O	TiO_2	P_2O_5	TOTAL	*n*
AT1b	12.1	0.64	0.28	0.00	5.20	79.16	1.86	0.08	0.68	100.00	4
2s	0.086	0.17	0.05	0.00	0.21	0.43	0.25	0.05	0.35		
AT2	17.83	9.28	6.97	3.00	2.72	56.68	1.86	1.17	0.49	100.00	4
2s	0.216	0.20	0.14	0.22	0.15	0.58	0.22	0.30	0.19		
AT3	16.82	4.42	3.95	0.37	4.33	66.61	2.63	0.49	0.39	100.00	4
2s	0.297	0.13	0.09	0.18	0.29	0.44	0.12	0.33	0.18		
AT4	14.29	1.38	0.97	0.00	5.79	76.13	1.28	0.15	0.02	100.00	4
2s	0.216	0.28	0.09	0.00	0.25	0.39	0.13	0.07	0.03		
AT5	12.89	0.77	0.66	0.00	5.78	79.14	0.47	0.09	0.19	100.00	4
2s	0.208	0.24	0.22	0.00	0.15	0.45	0.29	0.07	0.20		
AT6	12.2	0.71	0.33	0.00	5.44	80.21	0.76	0.05	0.30	100.00	4
2s	0.05	0.25	0.31	0.00	0.15	0.51	0.13	0.07	0.12		
AT8	14.61	10.63	6.48	5.03	2.83	58.00	0.87	1.06	0.52	100.00	4
2s	0.124	0.30	0.34	0.08	0.31	0.75	0.33	0.35	0.15		
11-22-1	15.76	0.02	0.86	0.00	5.46	76.33	1.53	0.01	0.05	100.00	5
2s	0.575	0.06	0.36	0.00	0.40	2.38	2.16	0.03	0.12		
11-22-2	14.63	1.06	1.22	0.00	4.35	73.44	4.98	0.27	0.04	99.99	5
2s	0.181	0.38	0.40	0.00	0.36	0.61	0.56	0.23	0.18		
11-22-3	15.18	1.15	1.13	0.00	4.21	72.97	4.99	0.32	0.05	100.00	5
2s	0.183	0.15	0.24	0.00	0.07	0.30	0.21	0.33	0.10		
11-22-4	14.25	0.70	1.22	0.00	4.64	73.63	5.12	0.23	0.21	100.00	5
2s	0.227	0.21	0.15	0.00	0.31	0.87	0.27	0.24	0.16		
11-22-5	14.36	0.90	1.08	0.00	4.68	73.48	5.09	0.22	0.19	100.00	5
2s	0.254	0.32	0.21	0.00	0.33	0.38	0.44	0.21	0.27		
11-22-6	14.6	0.59	0.83	0.00	4.17	75.44	4.06	0.27	0.04	100.00	5
2s	1.363	0.41	0.23	0.00	0.82	2.08	1.79	0.30	0.12		
11-22-7	17.54	0.70	0.52	0.00	2.82	71.58	6.74	0.10	0.00	100.00	5
2s	1.108	0.53	0.45	0.00	0.37	1.48	1.44	0.19	0.00		
11-22-8	18.58	3.89	1.49	6.58	2.17	60.98	5.69	0.60	0.03	100.01	3
2s	1.035	0.96	1.80	0.99	0.40	1.91	0.31	0.75	0.09		
11-22-9	15.57	1.16	1.09	0.00	3.43	72.55	5.76	0.44	0.00	100.00	3
2s	0.106	0.13	0.30	0.00	0.07	0.62	0.64	0.15	0.00		
11-22-10	15.97	1.20	0.97	0.00	3.86	71.92	5.77	0.26	0.05	100.00	10
2s	0.82	0.58	0.79	0.00	2.22	0.82	2.64	0.27	0.22		
11-22-12	16.55	1.52	1.50	0.00	5.19	70.04	4.92	0.20	0.09	100.00	5
2s	0.129	0.49	0.30	0.00	0.45	0.72	0.03	0.17	0.18		
11-22-13	16.49	1.30	1.19	0.00	4.76	70.54	5.46	0.25	0.00	99.99	5
2s	0.185	0.16	0.88	0.00	0.25	0.37	0.18	0.26	0.00		
11-22-14	18.97	3.78	2.01	5.22	2.29	59.74	7.20	0.65	0.13	100.00	5
2s	1.203	0.58	1.42	0.74	0.26	1.28	1.09	0.44	0.30		
11-22-16	19.4	2.41	1.38	1.48	2.53	63.13	9.02	0.39	0.27	100.00	5
2s	0.98	0.33	0.99	0.29	0.26	1.01	1.30	0.22	0.30		

Table 4. SEM data of lithium tetraborate glasses fused at UIUC. Oxide values are in wt. %.

Samples	SiO2	Al2O3	MgO	Na2O	FeO	MnO	TiO2	CaO	K2O	Total	*n*
AT 1b/PV-1	76.64	12.70	0.17	3.25	0.69	0.00	0.30	0.67	5.59	100.00	3
2s	0.62	0.19	0.03	0.09	0.08	0.08	0.04	0.04	0.08		
AT 1b/PV-1 dupl.	73.36	14.06	0.60	4.11	1.64	0.00	0.33	1.56	4.35	100.00	3
2s	0.12	0.25	0.05	0.07	0.14	0.01	0.03	0.03	0.26		
AT 2	46.46	11.89	17.98	2.19	10.22	0.00	1.32	8.86	1.08	100.00	3
2s	1.45	0.19	0.33	0.03	0.53	0.12	0.09	0.16	0.06		
AT 4/PV-3	72.67	14.31	0.62	3.84	1.16	0.00	0.38	1.64	5.37	100.00	3
2s	0.88	0.23	0.02	0.10	0.12	0.07	0.06	0.08	0.16		
11-17-1	45.22	8.69	26.52	1.56	11.34	0.00	1.01	4.63	1.01	100.00	3
2s	0.44	0.05	0.19	0.04	0.23	0.07	0.02	0.12	0.06		
11-17-2	45.17	8.65	26.16	1.62	11.93	0.00	0.95	4.53	1.00	100.00	3
2s	0.14	0.16	0.36	0.05	0.50	0.09	0.07	0.09	0.09		
11-17-3m	55.60	17.81	3.88	5.24	7.37	0.00	1.97	5.86	2.26	100.00	3
2s	2.02	0.65	0.09	0.08	0.29	0.07	0.08	0.16	0.08		
11-17-3f	56.92	12.61	1.21	12.01	2.49	0.00	0.45	4.36	9.96	100.00	2
2s	0.94	0.11	0.03	0.12	0.19	0.01	0.01	0.09	0.17		
11-17-4/PV-10	73.63	14.57	0.54	3.39	1.00	0.00	0.35	1.45	5.07	100.00	3
2s	13.69	2.16	0.04	0.07	0.35	0.06	0.03	0.08	0.71		
11-17-5/PV-9	68.82	16.80	1.16	3.06	2.93	0.00	0.62	2.39	4.22	100.00	2
2s	0.67	0.02	0.05	0.03	0.31	0.05	0.12	0.05	0.03		
11-17-7/PV-8	56.19	17.21	3.92	4.98	5.74	0.00	1.44	7.15	3.36	100.00	3
2s	4.77	1.60	0.25	0.17	0.33	0.06	0.12	0.06	0.13		
11-17-8/PV-7	71.26	14.71	0.61	4.85	0.84	0.00	0.28	2.57	4.88	100.00	2
2s	4.37	0.93	0.01	0.02	0.24	0.07	0.06	0.10	0.15		
11-17-10	58.65	14.23	1.37	10.16	2.50	0.00	0.37	3.75	8.98	100.00	2
2s	0.56	0.13	0.16	0.13	0.18	0.01	0.06	0.10	0.00		
11-17-11/PV-6	58.97	16.91	3.14	4.24	5.75	0.00	1.16	5.67	4.16	100.00	2
2s	0.54	0.17	0.09	0.07	0.23	0.10	0.09	0.09	0.09		
11-17-12	52.17	13.24	7.03	3.21	8.16	0.00	2.60	9.57	4.01	100.00	2
2s	0.34	0.35	0.36	0.01	0.08	0.07	0.03	0.17	0.08		
11-17-14/PV-4	72.84	15.10	0.59	4.09	0.94	0.00	0.27	1.72	4.45	100.00	3
2s	2.66	0.50	0.03	0.12	0.17	0.03	0.02	0.02	0.14		
11-17-15/PV-2	73.46	14.35	0.49	3.54	0.86	0.00	0.29	1.56	5.45	100.00	3
2s	33.61	5.96	0.16	0.08	0.38	0.06	0.08	0.20	1.20		

Table 5. Major element data from electron microprobe analyses. Oxide values are in wt.%

APPENDIX C. Rayleigh distillation model calculations

An ε^{56} for the AW dataset was determined using the formula $\varepsilon^{56} = 1000\ln\alpha$. α was determined by plotting $\ln(\delta^{56}Fe + 1000‰)$ vs. $\ln(FeO/FeO_i)$ (Figure 13) and taking the slope of the best fit line. The resulting $\varepsilon^{56} = -0.05‰$ is for the Rayleigh distillation curve that best fits the AW data. The $\delta^{56}Fe_{initial} = 0.09‰$ of the starting material used for the Rayleigh models was calculated using the y-intercept of slope of the best fit line from the $\ln(\delta^{56}Fe + 1000‰)$ vs. $\ln(FeO/FeO_i)$ chart (figure 13). This value also happens to be the "bulk earth" $\delta^{56}Fe$ determined by Beard et al. (2003).

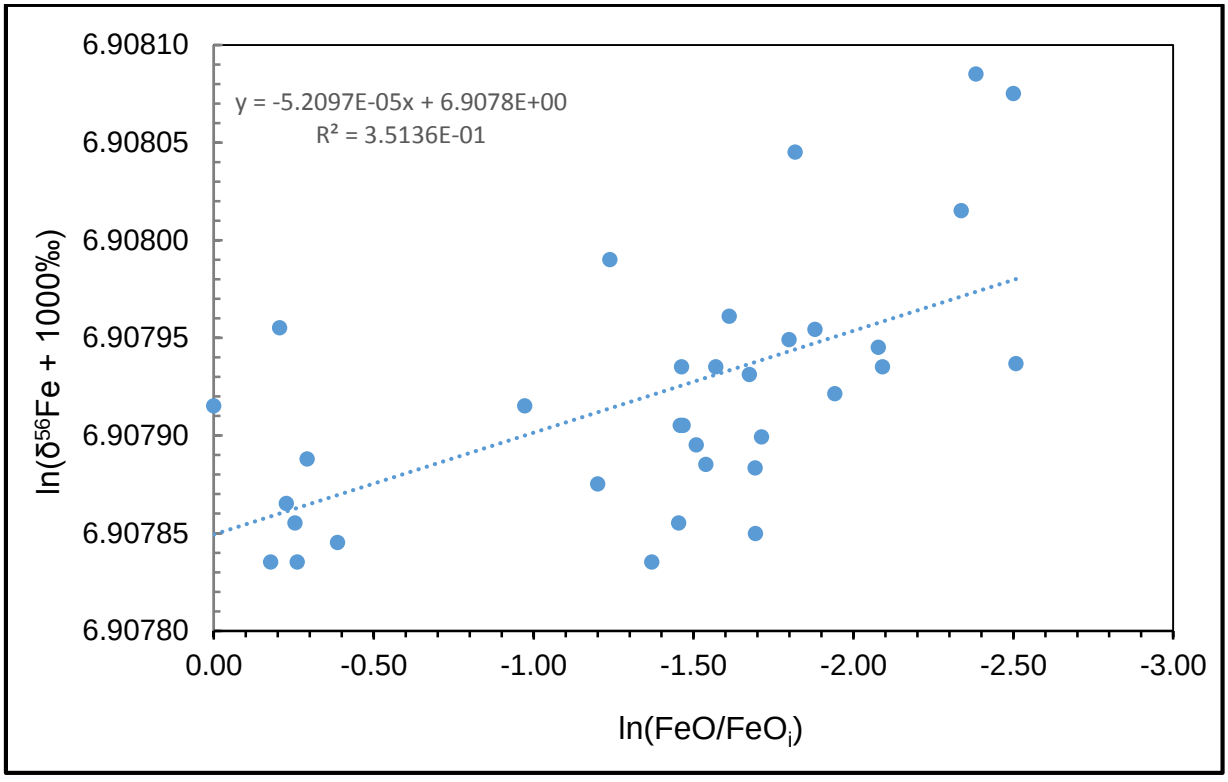

Figure 13. Plot of $\ln(\delta^{56}Fe + 1000‰)$ vs. $\ln(FeO/FeO_i)$. The slope of the best fit line was used to determine α, the ratio of $^{56}Fe/^{54}Fe$ of the product being produced at any given point in time over the $^{56}Fe/^{54}Fe$ of the remaining reactant.

Appendix D. Handheld XRF transects across in-situ samples

While conducting field work within the Aztec wash pluton, we had a Thermo Scientific Niton XL3t handheld X-Ray Fluorescence (XRF) instrument in order to obtain in-situ analyses of bulk compositions. It was hoped that the data collected could be used to observe trends in composition across magmatic features such as layered sheets and enclaves. The instrument was brought to an area within the eastern block of the pluton, just east of the pipe canyon fault within the heterogeneous zone. This part of the heterogeneous zone contains a very wide variety of intrusive relationships as shown previously in figure 4. Six small (meter or less in length) transects were chosen across which the XRF was applied to obtain approximate bulk compositions. Those transects are PC 1 (fig. 13, 14, 15), PC 2 (figs. 13, 16, 17), PC 3 (figs. 18, 19), PC5 (figs. 20, 21) and PS (figs. 22, 23).

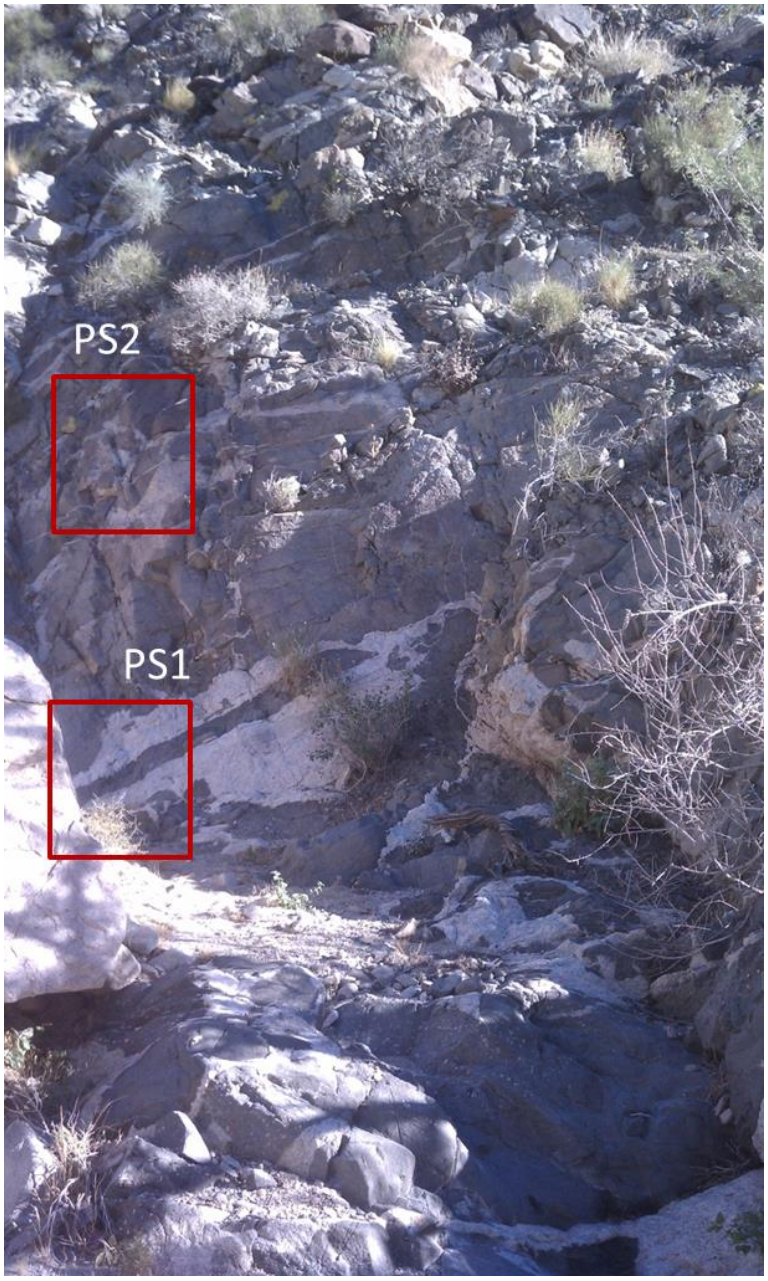

Figure 14. Showing the location of transects PC1 and PC2 in relation to each other. This image also helps to provide a context by which to better understand the intrusive geometries each transect focuses on.

Figure 15. Close up of transect PC 1. This transect occurs across a finger of fine-grained mafic material with feldspar phenocrysts. The mafic finger is surrounded by coarse=grained porphyritic granite. Transect position *a* starts in the lower right corner is and extends across the mafic finger to the hand holding the pen, which is transect position *l*. Field notebook for scale.

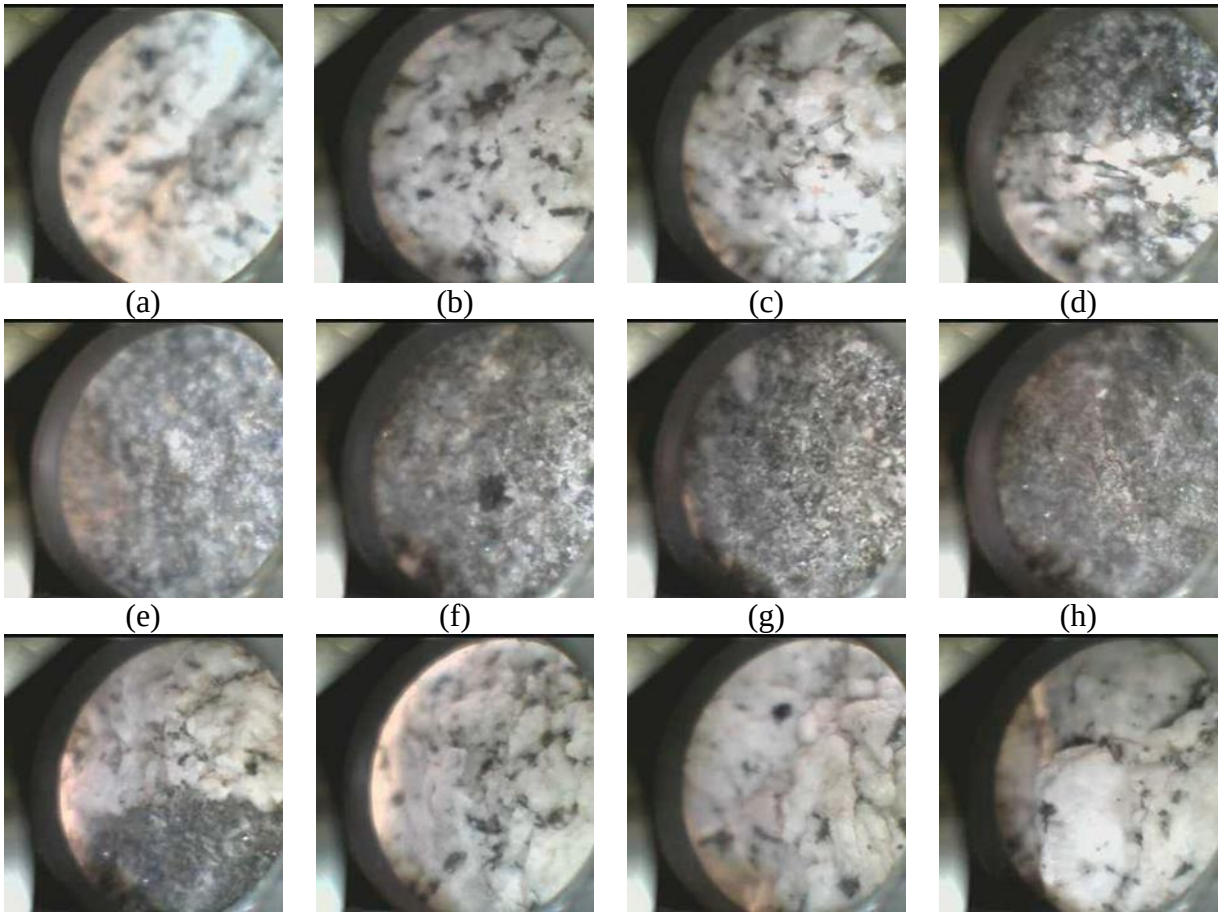

Figure 16. Shows the area that was analyzed at each point in the transect PC1. Consists of 12 spots in all, ordered from *a*-*l*.

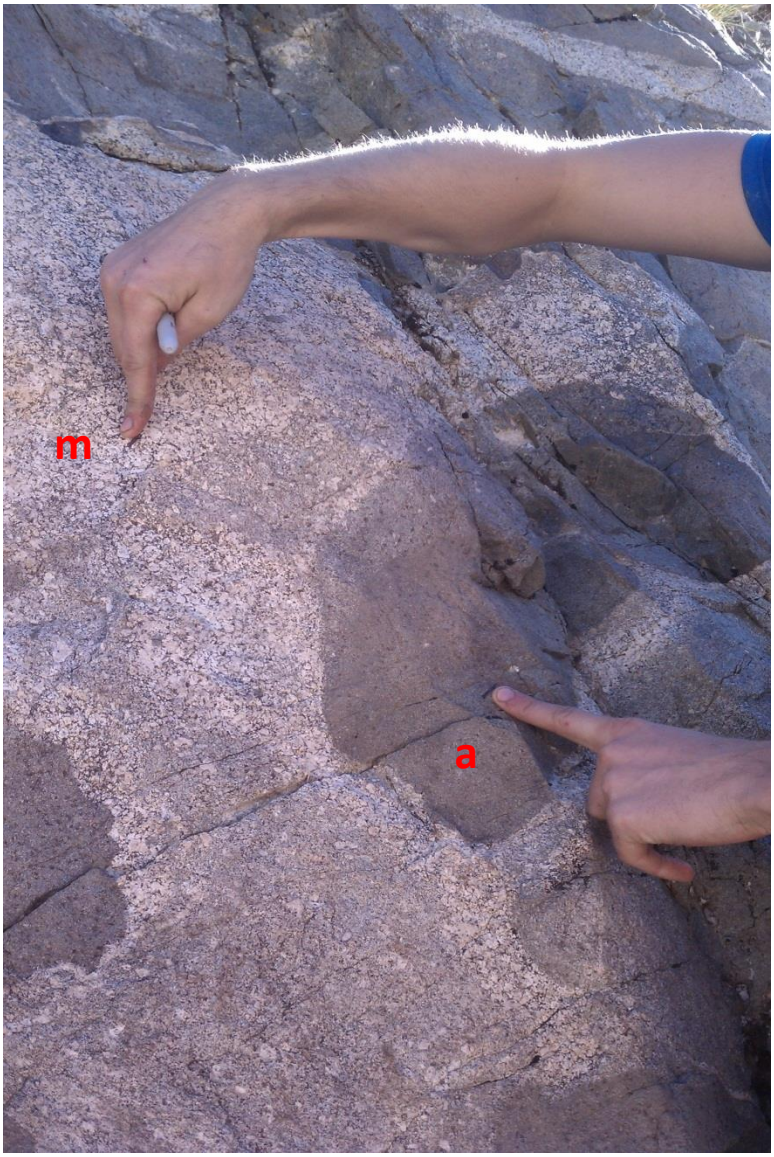

Figure 17. Transect PC2 starts in a fine-grained mafic blob (possibly an enclave) and passes through the contact with the surrounding material into the lighter colored, more felsic rock. However, neither the surrounding rock nor the mafic blob are homogenous. The mafic blob becomes lighter in color towards the edge, while the surrounding rock contains differing amounts of mafic phases. At the contact with the blob, the surrounding rock contains relatively low amounts of mafic phases, and is relatively light.

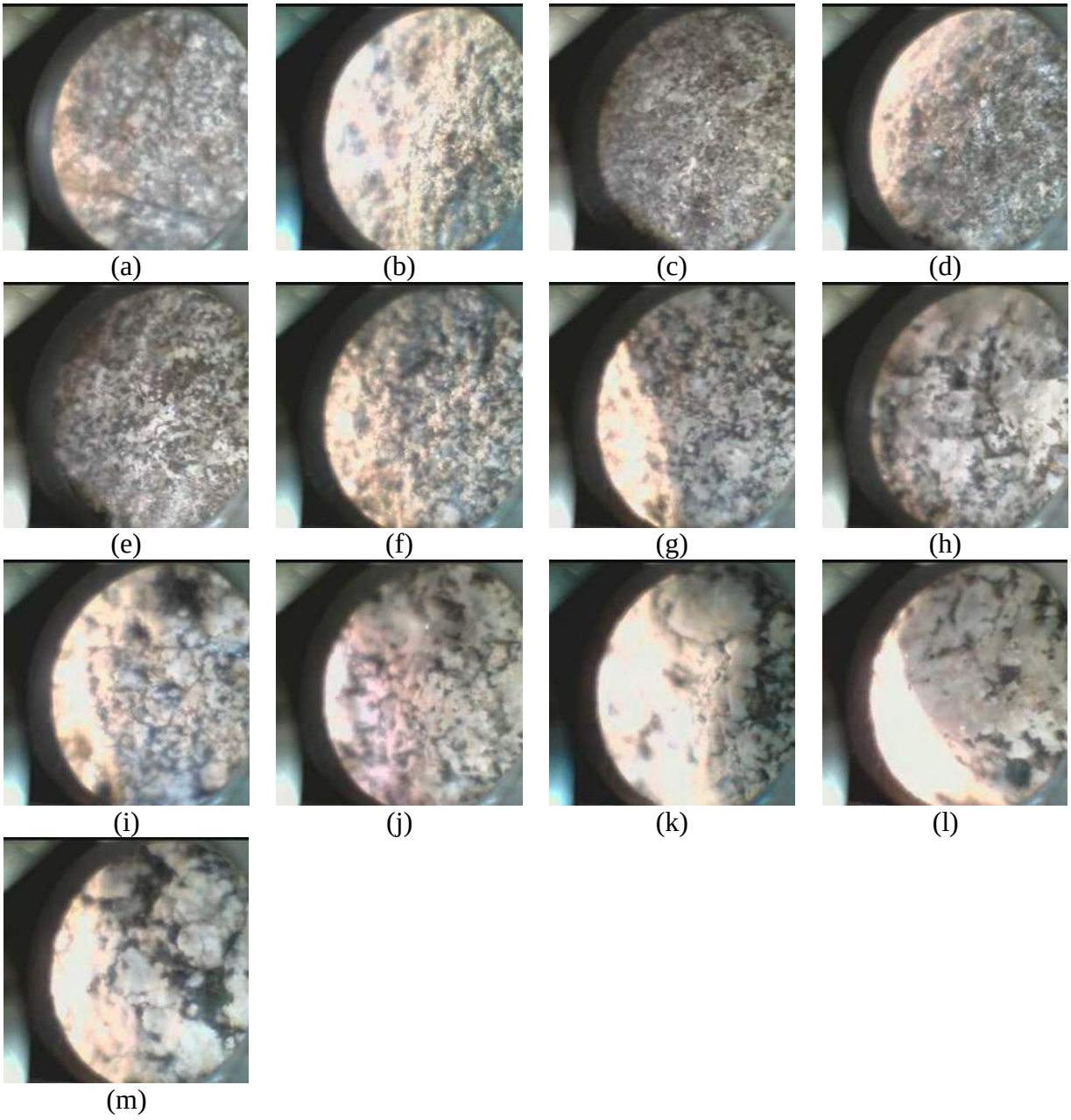

Figure 18. Images of the analysis spots from transect PC 2, thirteen spots total. The transect starts with spot a and ends with spot m.

Figure 19. Transect PC 3, which occurs across a sharp contact between a light colored granitic layer and another felsic layer which contains more mafic phases. Both layers are porphyritic with feldspar phenocrysts.

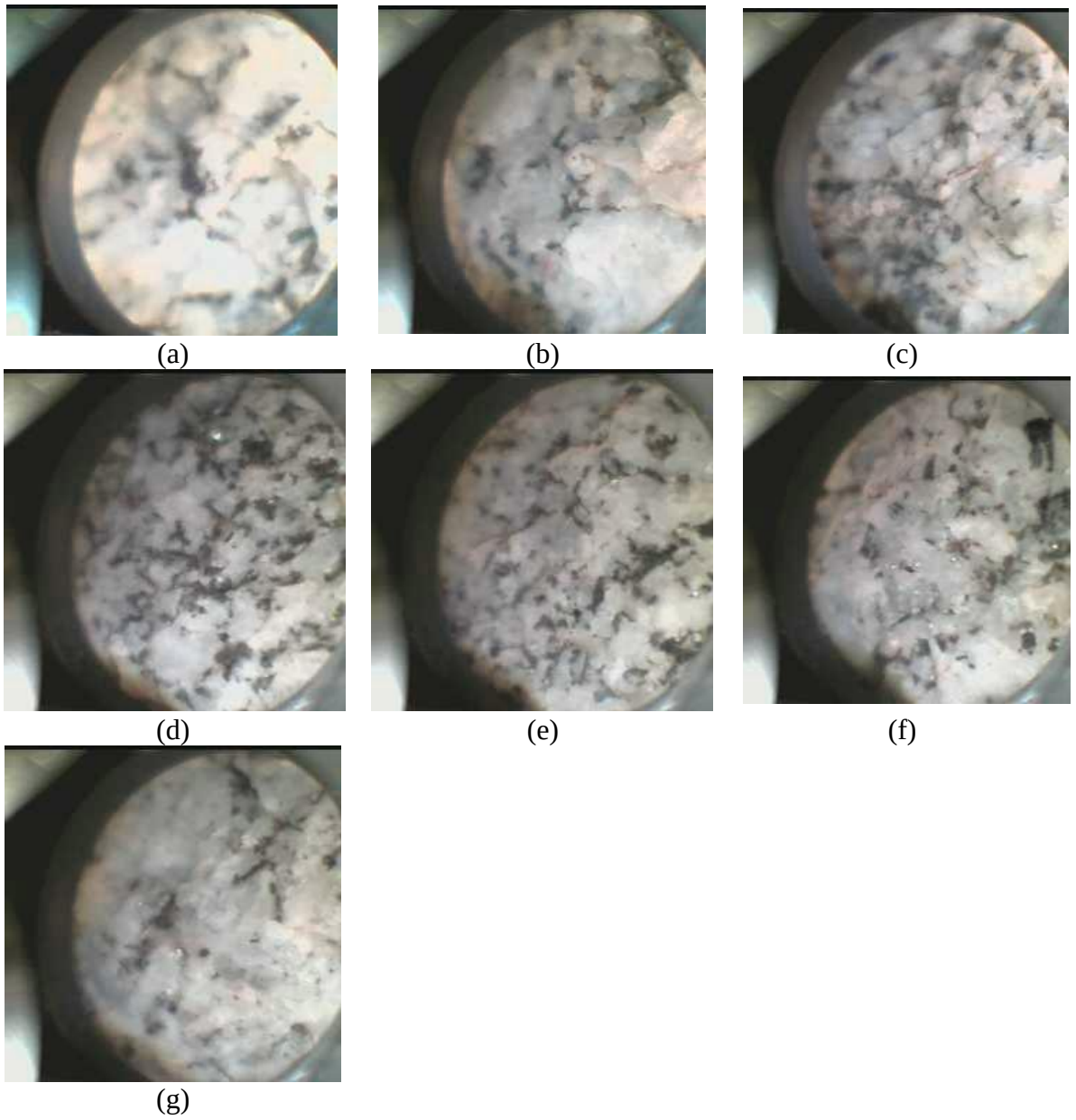

Figure 20. Analyzed spots for PC 3, seven in total. The transect starts with spot a, and ends with spot g.

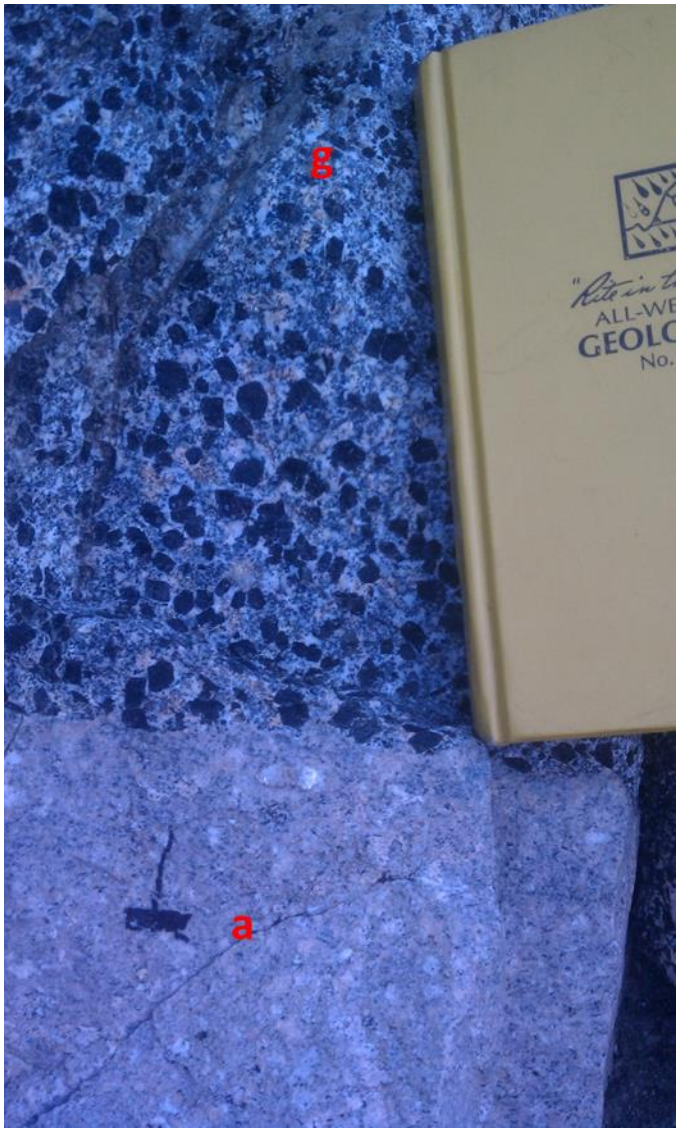

Figure 21. Image of PC5 transect from a porphyritic granite into an amphibole-diorite. The granite contains feldspar phenocrysts, while the diorite contains phenocrysts of feldspar and amphibole. Transect includes seven spots, from a to g.

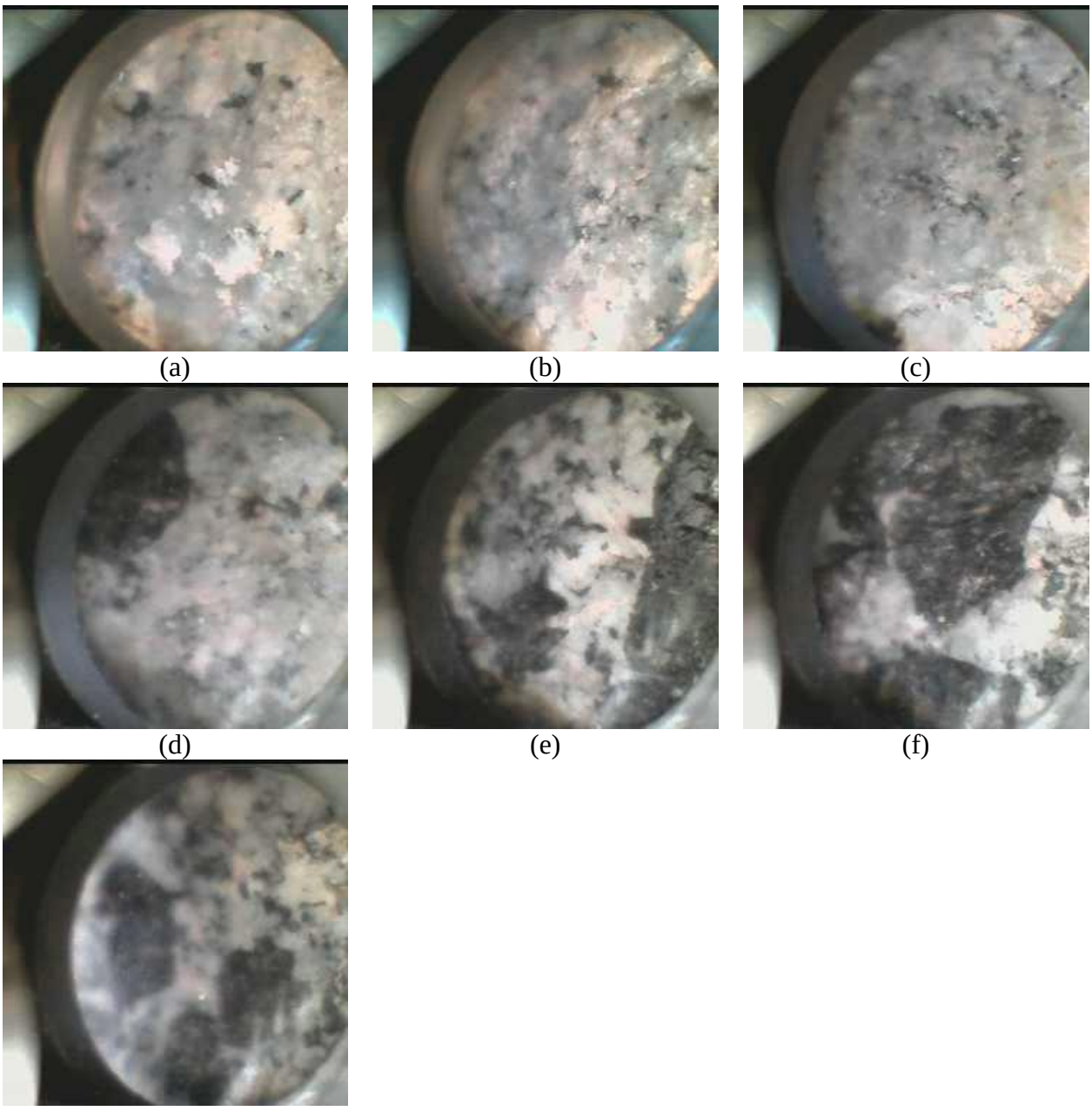

Figure 22. Analyzed spots for transect PC5, from a to g.

Figure 23. Transect PS across an irregularly shaped lobe of fine-grained mafic material within coarser porphyritic granitoid. This transect consists of 10 spots from a to j.

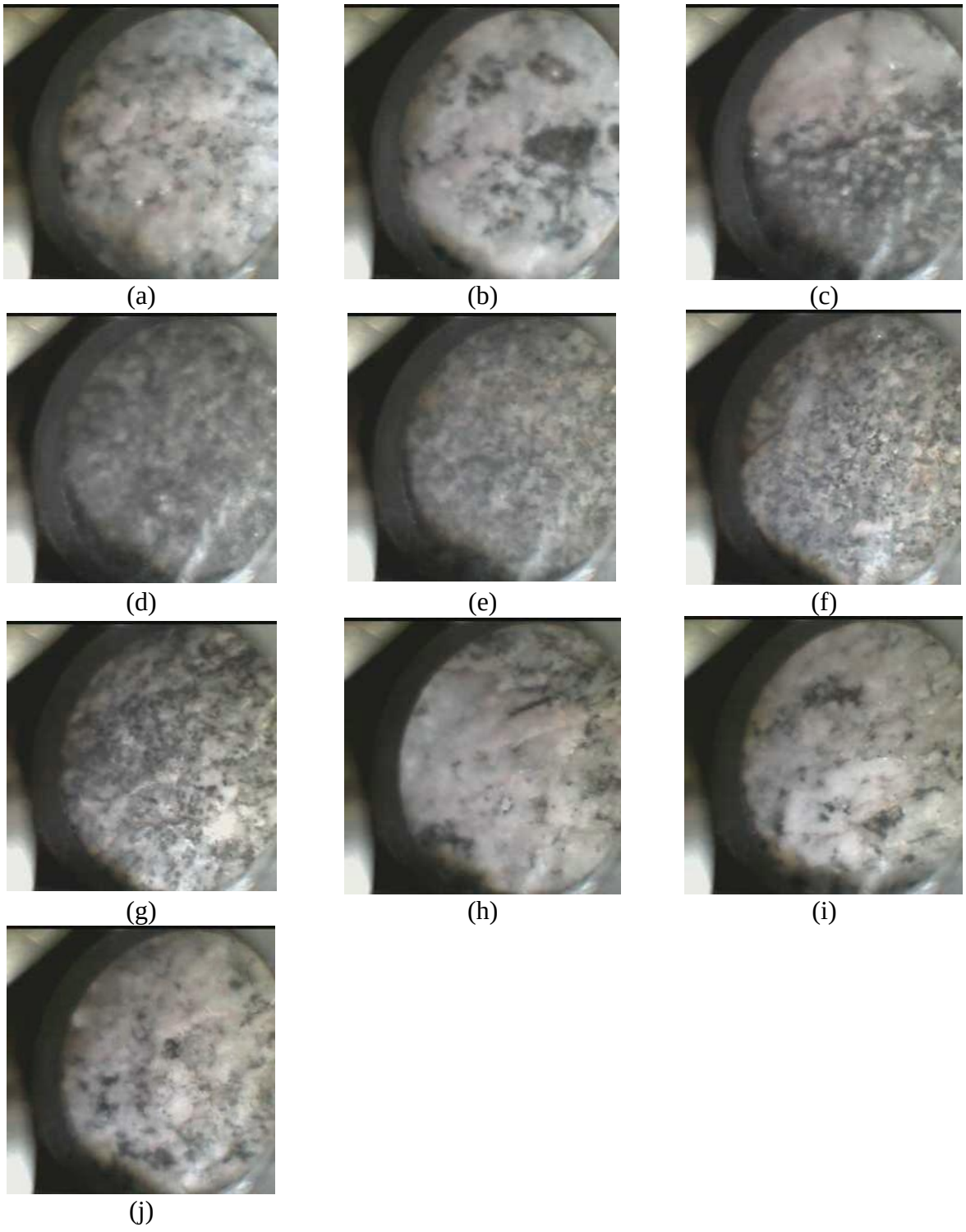

Figure 24. The ten analyzed spots for PS from a to j.

Sample	Transect	Mo	Error	Zr	Error	Sr	Error	U	Error	Rb	Error
a	pc1	< LOD	-	85.23	5.12	882.19	10.79	9.23	5.71	35.94	3.16
b	pc1	< LOD	-	394.2	7.14	1000.56	10.49	16.32	5.78	42.57	2.53
c	pc1	< LOD	-	127.02	5.27	1010.15	10.66	20.85	5.76	29.33	2.24
d cont	pc1	< LOD	-	189.75	5.95	926.77	10.66	14.91	6.06	46.69	2.76
e	pc1	< LOD	-	255.34	6.93	465.42	8.31	< LOD	-	55.19	3.33
f	pc1	< LOD	-	281.72	6.68	822.33	10.22	11.43	5.95	42.22	2.59
g	pc1	4.99	3.2	269.56	6.7	890.94	10.71	< LOD	-	54.87	3.01
h	pc1	< LOD	-	317.53	7.18	720.38	10.05	9.88	6.27	51.96	3.05
i cont	pc1	< LOD	-	445.64	7.26	805.61	9.39	16.05	5.34	29.78	2.19
j	pc1	< LOD	-	508.96	7.29	954.74	9.6	17.39	5.51	48.78	2.5
k	pc1	< LOD	-	162.27	5.29	983.8	10.08	12.52	5.47	43.87	2.49
l	pc1	< LOD	-	230.92	5.47	898.52	9.2	15.83	5.25	45.17	2.24
		Th	**Error**	**Pb**	**Error**	**Au**	**Error**	**Se**	**Error**	**As**	**Error**
a	pc1	8.49	3.19	< LOD	-	< LOD	-	< LOD	-	< LOD	-
b	pc1	7.19	3.03	19.27	5.33	< LOD	-	< LOD	-	< LOD	-
c	pc1	15.21	3.4	19.39	5.38	< LOD	-	< LOD	-	< LOD	-
d cont	pc1	5.87	3.16	19.72	5.61	< LOD	-	< LOD	-	< LOD	-
e	pc1	< LOD	-	< LOD	-	< LOD	-	< LOD	-	8.94	4.73
f	pc1	< LOD	-	8.24	5.01	< LOD	-	< LOD	-	< LOD	-
g	pc1	< LOD	-	17.02	5.74	< LOD	-	5.29	3.12	< LOD	-
h	pc1	< LOD	-	13.26	5.72	< LOD	-	< LOD	-	< LOD	-
i cont	pc1	10.27	3.18	27.44	5.67	< LOD	-	< LOD	-	7.03	4.02
j	pc1	10.73	2.99	20.58	5.08	< LOD	-	< LOD	-	< LOD	-
k	pc1	6.06	2.77	22.45	5.21	< LOD	-	< LOD	-	< LOD	-
l	pc1	14.69	3.04	17.19	4.53	< LOD	-	< LOD	-	< LOD	-
		Hg	**Error**	**Zn**	**Error**	**W**	**Error**	**Cu**	**Error**	**Ni**	**Error**
a	pc1	< LOD	-	12.92	7.19	< LOD	-	< LOD	-	< LOD	-
b	pc1	< LOD	-	31.75	7.42	< LOD	-	18.6	11.91	< LOD	-
c	pc1	< LOD	-	17.86	6.84	< LOD	-	23.18	12.58	88.02	26.71
d cont	pc1	< LOD	-	41.25	8.33	< LOD	-	29.31	13.48	62.14	27.78
e	pc1	< LOD	-	81.03	12.39	< LOD	-	< LOD	-	< LOD	-
f	pc1	< LOD	-	70.3	9.89	< LOD	-	55.86	15.48	98.55	30.92
g	pc1	< LOD	-	75.13	10.13	56.33	34.05	39.96	14.51	107.73	30.6
h	pc1	< LOD	-	95.28	11.32	< LOD	-	52.19	15.97	101.29	32.44
i cont	pc1	< LOD	-	41.46	7.89	48.08	29.38	29.7	12.4	56.43	25.74
j	pc1	< LOD	-	24.97	6.59	< LOD	-	25.67	11.28	45.76	23.34
k	pc1	< LOD	-	13.75	6.22	< LOD	-	< LOD	-	< LOD	-
l	pc1	< LOD	-	16.26	5.98	< LOD	-	< LOD	-	< LOD	-

Table 6. Handheld XRF data for the in-situ transect pc1. Values are given in ppm. LOD stands for Limit of Detection.

Sample	Transect	Co	Error	Fe	Error	Mn	Error	Cr	Error	V	Error
a	pc1	134.68	65.52	12628.2	1354.05	193.83	54.02	< LOD	-	46.11	29.34
b	pc1	< LOD	-	25979.86	301.3	418.97	58.34	< LOD	-	37.67	23.98
c	pc1	< LOD	-	24603.13	296.94	340.64	56.63	< LOD	-	64.42	17.12
d	pc1	< LOD	-	32874.59	363.01	507.18	65.19	< LOD	-	72.87	21.9
e	pc1	< LOD	-	54718.64	560.08	1224.65	120.81	< LOD	-	119.45	25.88
f	pc1	< LOD	-	59250.34	500.66	911.65	80.86	76.26	34.61	255.9	60.56
g	pc1	< LOD	-	60059.29	520.91	893.74	81.41	125.23	31.68	177.45	38.53
h	pc1	< LOD	-	62964.07	559.87	1421.96	97.12	132.2	36.56	184.13	36.21
i	pc1	< LOD	-	30706.88	327.51	602.41	64.13	84.81	24.51	99.51	24.27
j	pc1	< LOD	-	18868.04	242.38	347.93	51.72	< LOD	-	72.88	20.96
k	pc1	< LOD	-	4987.26	104.79	164.71	46.26	< LOD	-	< LOD	-
l	pc1	< LOD	-	11789.88	176.7	235.71	46.47	< LOD	-	< LOD	-
		Ti	**Error**	**Sc**	**Error**	**Ca**	**Error**	**K**	**Error**	**S**	**Error**
a	pc1	1945.64	104.69	-	-	17785.25	879.96	18513.93	821.69	-	-
b	pc1	4293.89	90.33	< LOD	-	20699.74	493.66	24833.76	364.81	709.07	178.93
c	pc1	2377.13	61.82	50.67	24.08	22622.51	498.87	15845.56	291.89	735.17	151.01
d	pc1	4296.01	82.98	90.68	30.72	31968.91	618.04	21283.66	350.61	589.01	162.46
e	pc1	6620.89	101.7	75.57	40.75	65228.15	1014.96	17233.36	381.1	641.61	174.27
f	pc1	8747.57	142.95	-	-	51407.72	897.32	14746.7	353.78	-	-
g	pc1	8416.32	145.19	< LOD	-	35929.71	754.05	25735.57	434.99	616.64	228.12
h	pc1	9018.41	140.92	< LOD	-	47485.26	899.6	16322.94	380.34	1156.22	249.94
i	pc1	4692.61	91.07	73.2	34.37	31949.38	588.89	10335.25	242.21	524.58	164.69
j	pc1	3210.6	76.29	72.56	29.1	26067.2	511.18	21952.06	324.15	835.25	171.27
k	pc1	894.3	43.58	49.1	21.14	21943.67	425.76	20004.71	285.86	1470.65	156.87
l	pc1	1378.63	46.87	-	-	21173.06	423.71	17607.11	270.74	-	-
		Ba	**Error**	**Cs**	**Error**	**Te**	**Error**	**Sb**	**Error**	**Sn**	**Error**
a	pc1	1102.54	81.21	-	-	-	-	< LOD	-	< LOD	-
b	pc1	1288.44	46.03	94.82	10.09	145.11	29.85	38.57	10.91	29.19	8.54
c	pc1	1284.71	49.38	76.76	10.73	82.96	31.33	35.57	11.64	23.65	9.08
d	pc1	1484.04	50.52	88.61	10.77	130.06	31.8	32.08	11.58	23.06	9.04
e	pc1	1522.9	64.74	141.93	14.16	209.02	41.76	53.75	15.2	40.24	11.92
f	pc1	1142.07	63.71	-	-	-	-	< LOD	-	< LOD	-
g	pc1	1932.74	54.61	69.89	10.94	76.45	31.92	31.41	11.81	18.7	9.17
h	pc1	1449.6	56.47	98.7	12.18	167.21	36.18	38.43	13.1	33.44	10.36
i	pc1	992.69	45.39	71.13	10.23	68.09	29.78	25.17	10.98	15.08	8.53
j	pc1	1248.62	43.47	65.92	9.43	94.42	27.8	15.62	10.04	22.14	7.98
k	pc1	1280.34	46.02	82.26	10.04	102.58	29.43	43.93	10.99	28.7	8.56
l	pc1	829.16	43.67	-	-	-	-	< LOD	-	< LOD	-

Table 6. (cont.)

Sample	Transect	Cd	Error	Ag	Error	Pd	Error	Nb	Error	Bi	Error
a	pc1	< LOD	-	< LOD	-	< LOD	-	< LOD	-	< LOD	-
b	pc1	19.28	8.2	< LOD	-	< LOD	-	12.84	1.68	< LOD	-
c	pc1	< LOD	-	< LOD	-	< LOD	-	5.49	1.54	11.54	4.35
d	pc1	< LOD	-	< LOD	-	< LOD	-	6.14	1.62	< LOD	-
e	pc1	30.71	11.52	< LOD	-	< LOD	-	15.6	2.08	< LOD	-
f	pc1	< LOD	-	< LOD	-	< LOD	-	20.83	1.88	< LOD	-
g	pc1	< LOD	-	< LOD	-	< LOD	-	17.74	1.89	< LOD	-
h	pc1	15.19	9.76	10.79	6.58	< LOD	-	15.31	1.93	< LOD	-
i	pc1	< LOD	-	< LOD	-	< LOD	-	19.96	1.79	8.48	4.19
j	pc1	< LOD	-	< LOD	-	< LOD	-	13.5	1.58	7.57	3.99
k	pc1	18.6	8.2	10.39	5.47	< LOD	-	4.89	1.47	< LOD	-
l	pc1	< LOD	-	< LOD	-	< LOD	-	5.03	1.31	13.88	3.84

Sample		Re	Error	Ta	Error	Hf	Error
a	pc1	< LOD	-	< LOD	-	< LOD	-
b	pc1	< LOD	-	< LOD	-	< LOD	-
c	pc1	< LOD	-	< LOD	-	< LOD	-
d	pc1	< LOD	-	< LOD	-	< LOD	-
e	pc1	< LOD	-	< LOD	-	< LOD	-
f	pc1	< LOD	-	< LOD	-	< LOD	-
g	pc1	< LOD	-	< LOD	-	< LOD	-
h	pc1	< LOD	-	< LOD	-	< LOD	-
i	pc1	< LOD	-	< LOD	-	< LOD	-
j	pc1	< LOD	-	< LOD	-	< LOD	-
k	pc1	< LOD	-	< LOD	-	< LOD	-
l	pc1	< LOD	-	< LOD	-	< LOD	-

Table 6. (cont.)

Sample	Transect	Mo	Error	Zr	Error	Sr	Error	U	Error	Rb	Error
a	pc2	< LOD	-	184.42	36.11	494.26	49.77	< LOD	-	37	16.69
b	pc2	< LOD	-	125.38	4.53	509.18	7.26	< LOD	-	46.54	2.57
c	pc2	< LOD	-	404.69	7.47	765.62	9.81	11.19	5.93	47.29	2.79
d	pc2	< LOD	-	161.97	5.75	730.08	9.96	11.63	6.32	55.39	3.09
e	pc2	4.96	3.05	148.24	5.49	688.18	9.55	< LOD	-	56.33	3.07
f	pc2	< LOD	-	128.54	5.51	713.44	10.07	< LOD	-	44.12	2.86
g	pc2	5.08	2.89	153.83	5.13	620.08	8.55	10.39	5.61	52.62	2.81
h	pc2	< LOD	-	208.72	5.47	688.43	8.66	12.67	5.72	66.85	3
i	pc2	< LOD	-	236.8	5.87	573.11	8.33	< LOD	-	36.85	2.49
j	pc2	6.41	3	300.8	6.08	528.47	7.68	10.8	4.9	32.55	2.26
k	pc2	< LOD	-	319.95	6.36	600.31	8.28	11.22	5.26	42.11	2.53
l	pc2	< LOD	-	180.11	4.99	694.88	8.29	8.66	5.22	60.6	2.76
m	pc2	9.35	3.51	563.85	8.18	648.37	8.81	11.35	5.6	47.42	2.73
Sample		**Th**	**Error**	**Pb**	**Error**	**Au**	**Error**	**Se**	**Error**	**As**	**Error**
a	pc2	< LOD	-	< LOD	-	< LOD	-	< LOD	-	< LOD	-
b	pc2	< LOD	-	38.35	6.12	< LOD	-	< LOD	-	17.13	5.44
c	pc2	5.59	3.49	47.22	6.94	< LOD	-	< LOD	-	15.9	6.09
d	pc2	< LOD	-	37.1	6.76	< LOD	-	< LOD	-	22.05	6.18
e	pc2	6.93	3.62	51.19	7.28	< LOD	-	< LOD	-	16.04	6.38
f	pc2	< LOD	-	50.5	7.47	< LOD	-	< LOD	-	19.74	6.69
g	pc2	5	3.26	57.08	7.06	< LOD	-	< LOD	-	18.74	6.28
h	pc2	5.52	3.02	55.68	6.71	< LOD	-	< LOD	-	17.41	5.04
i	pc2	9.22	3.29	44.51	6.65	< LOD	-	< LOD	-	9.44	4.8
j	pc2	16.21	3.42	34.3	5.99	< LOD	-	< LOD	-	9.13	4.26
k	pc2	13.4	3.36	34.62	6.04	< LOD	-	< LOD	-	< LOD	-
l	pc2	5.71	2.73	32.92	5.55	< LOD	-	< LOD	-	< LOD	-
m	pc2	13.51	3.56	51.32	6.89	< LOD	-	< LOD	-	11.26	5.08
Sample		**Hg**	**Error**	**Zn**	**Error**	**W**	**Error**	**Cu**	**Error**	**Ni**	**Error**
a	pc2	< LOD	-	< LOD	-	< LOD	-	< LOD	-	< LOD	-
b	pc2	< LOD	-	76.22	10.14	< LOD	-	31.51	15.55	< LOD	-
c	pc2	< LOD	-	75.65	10.07	72.25	34.1	50.86	14.65	105.04	30.24
d	pc2	< LOD	-	95.8	11.06	< LOD	-	67.07	16.07	103.47	31.72
e	pc2	< LOD	-	88.38	10.68	< LOD	-	40.2	14.68	137.28	31.13
f	pc2	< LOD	-	85.04	11.05	< LOD	-	27.21	15.18	64.21	31.22
g	pc2	< LOD	-	69.96	9.33	< LOD	-	26.22	13.32	75.78	28.12
h	pc2	< LOD	-	25.83	7.03	< LOD	-	21.17	11.95	48.11	24.81
i	pc2	< LOD	-	35.71	7.99	< LOD	-	21.69	13.1	< LOD	-
j	pc2	< LOD	-	29.63	7.42	< LOD	-	27.7	12.62	< LOD	-
k	pc2	< LOD	-	38.86	7.88	< LOD	-	< LOD	-	< LOD	-
l	pc2	< LOD	-	12.46	5.92	< LOD	-	< LOD	-	49.3	23.17
m	pc2	< LOD	-	34.91	7.87	< LOD	-	27.8	13.08	< LOD	-

Table 7. Handheld XRF data for the in-situ transects pc2. Values are given in ppm. LOD stands for Limit of Detection.

Sample	Transect	Co	Error	Fe	Error	Mn	Error	Cr	Error	V	Error
a	pc2	< LOD	-	52567.25	3056.66	1565.11	758.88	175.61	40.94	282.69	74.88
b	pc2	< LOD	-	63979.52	499.11	1519.78	103.5	158.68	33.55	270.4	54.69
c	pc2	220.71	145.04	58973.42	507.81	1525.02	93.87	202.71	32.7	261.58	38.6
d	pc2	< LOD	-	66017.03	565.99	1611.38	100.26	150.58	34.54	186.62	34
e	pc2	< LOD	-	56145.08	506.59	1825.66	101.98	214.99	33.28	164.38	36.12
f	pc2	< LOD	-	54716.02	516.1	2276.74	114	134.98	35.16	139.65	29.78
g	pc2	< LOD	-	48218.34	436.29	2348.56	104.19	201.53	29.68	128.91	25.28
h	pc2	< LOD	-	20348.78	266.67	1885.06	89.91	61.7	24.75	56.51	22.61
i	pc2	< LOD	-	26807.51	324.56	1286.16	82.86	< LOD	-	75.96	18.1
j	pc2	< LOD	-	25804.61	301.78	1004.54	73.29	< LOD	-	73.46	17
k	pc2	< LOD	-	23639.04	292.03	1024.03	74.26	69.38	22.64	63.79	19.26
l	pc2	< LOD	-	5950.11	111.92	778.15	62.35	< LOD	-	30.4	19.28
m	pc2	< LOD	-	23528.36	297.69	2894.6	111.58	< LOD	-	60.87	17.18
		Ti	**Error**	**Sc**	**Error**	**Ca**	**Error**	**K**	**Error**	**S**	**Error**
a	pc2	7295.31	342.95	-	-	47258.38	1991.5	12132.86	553.22	-	-
b	pc2	6480.34	120.85	-	-	43168.5	808.11	12224.16	319.01	-	-
c	pc2	9196.22	146.3	123.97	49.15	42118.81	801.03	14106.56	333.98	< LOD	-
d	pc2	8163.22	131.35	120.99	47.36	46045.88	842.87	12389.65	322.25	390.64	202.45
e	pc2	8530.59	139.89	107.22	46.77	39877.69	798.05	18705.59	384.02	< LOD	-
f	pc2	6341.9	113.57	94.25	38.28	38355.46	801.44	16851.9	379.28	590.25	194.61
g	pc2	3774.21	90.73	63.7	31.33	27114.79	623.76	22491.39	389.16	523.78	181.93
h	pc2	1618.32	76.71	< LOD	-	6423.44	135.08	40812.9	476.75	640.26	171.83
i	pc2	3458.86	67.35	< LOD	-	16019.2	428.69	13155.35	272.96	472.36	124.99
j	pc2	2737.64	61.69	33.7	17.21	13564.68	379.45	14085.51	268.39	395.39	120.49
k	pc2	3517.27	71.54	< LOD	-	14077.8	403.81	19867.65	321.22	370.77	130.51
l	pc2	1887.49	67.28	< LOD	-	7118.57	119.27	34891.41	398.38	521	139.29
m	pc2	1882.13	59.81	< LOD	-	6657.64	111.82	25789.11	358.89	666.15	136.81
		Ba	**Error**	**Cs**	**Error**	**Te**	**Error**	**Sb**	**Error**	**Sn**	**Error**
a	pc2	1456.4	107.93	-	-	-	-	< LOD	-	< LOD	-
b	pc2	979.4	59.28	-	-	-	-	< LOD	-	< LOD	-
c	pc2	1423.05	53.38	91.81	11.49	94.45	33.39	32.72	12.3	16.27	9.48
d	pc2	1331.89	72.93	96.38	15.92	116.86	46.57	35.58	17.11	23.17	13.28
e	pc2	1519.99	52.25	90.19	11.1	90.43	32.25	28.95	11.86	25.58	9.34
f	pc2	1339.37	57.34	102.16	12.56	128.02	36.76	42.52	13.53	18.14	10.38
g	pc2	1404.05	51.92	87.58	11.18	117.07	32.85	32.58	12.02	20.73	9.34
h	pc2	1756.36	48.76	96.14	10.1	145.71	29.84	34.15	10.84	30.53	8.56
i	pc2	1032.07	49.24	80.46	11.1	95.77	32.48	29.71	11.94	18.77	9.29
j	pc2	980.61	46.6	65.07	10.5	103.6	31.04	26.06	11.3	< LOD	-
k	pc2	1087.73	46.17	68.71	10.26	99.57	30.25	24.45	11.04	23.64	8.71
l	pc2	1569.12	46.79	93.68	9.89	126.72	29.09	41.7	10.74	26.76	8.35
m	pc2	1040.32	46.24	71.29	10.36	125.31	30.79	22.79	11.11	20.18	8.71

Table 7 (cont.)

Sample	Transect	Cd	Error	Ag	Error	Pd	Error	Nb	Error	Bi	Error
a	pc2	< LOD	-	< LOD	-	< LOD	-	< LOD	-	< LOD	-
b	pc2	< LOD	-	< LOD	-	< LOD	-	14.58	1.69	< LOD	-
c	pc2	< LOD	-	< LOD	-	< LOD	-	16.28	1.84	< LOD	-
d	pc2	< LOD	-	< LOD	-	< LOD	-	17.92	1.95	< LOD	-
e	pc2	< LOD	-	< LOD	-	< LOD	-	16.86	1.9	< LOD	-
f	pc2	< LOD	-	< LOD	-	< LOD	-	10.07	1.83	< LOD	-
g	pc2	< LOD	-	< LOD	-	< LOD	-	12.42	1.71	< LOD	-
h	pc2	18.77	8.19	< LOD	-	< LOD	-	13.49	1.67	< LOD	-
i	pc2	< LOD	-	10.07	6.03	< LOD	-	19.6	1.9	< LOD	-
j	pc2	< LOD	-	< LOD	-	< LOD	-	16.3	1.75	14.18	4.44
k	pc2	12.69	8.31	< LOD	-	< LOD	-	20.4	1.85	13.05	4.51
l	pc2	16.99	8	< LOD	-	< LOD	-	7.03	1.48	< LOD	-
m	pc2	< LOD	-	< LOD	-	< LOD	-	14.84	1.79	10.69	4.65
		Re	Error	Ta	Error	Hf	Error				
a	pc2	< LOD	-	< LOD	-	< LOD	-				
b	pc2	< LOD	-	< LOD	-	< LOD	-				
c	pc2	< LOD	-	< LOD	-	< LOD	-				
d	pc2	< LOD	-	< LOD	-	< LOD	-				
e	pc2	< LOD	-	< LOD	-	< LOD	-				
f	pc2	< LOD	-	< LOD	-	< LOD	-				
g	pc2	< LOD	-	< LOD	-	< LOD	-				
h	pc2	< LOD	-	< LOD	-	< LOD	-				
i	pc2	< LOD	-	< LOD	-	< LOD	-				
j	pc2	< LOD	-	< LOD	-	< LOD	-				
k	pc2	< LOD	-	< LOD	-	< LOD	-				
l	pc2	< LOD	-	< LOD	-	< LOD	-				
m	pc2	< LOD	-	< LOD	-	< LOD	-				

Table 7 (cont.)

Sample	Transect	Mo	Error	Zr	Error	Sr	Error	U	Error	Rb	Error
a	pc3	< LOD	-	202.71	6.09	873.37	10.51	16.04	5.87	35.21	2.52
b	pc3	< LOD	-	269.08	6.15	920.79	9.95	16.41	5.73	55.21	3.37
c	pc3	< LOD	-	240.73	6.03	926.48	10.11	14.42	5.98	61.97	2.95
d	pc3	< LOD	-	543.3	8.31	974.57	10.75	11.01	6.14	57.92	2.97
e	pc3	9.25	3.19	387.11	7.11	951.77	10.32	< LOD	-	54.19	2.81
f	pc3	< LOD	-	351.26	7.52	1367.94	12.8	12.88	6.51	60.19	3.75
g	pc3	< LOD	-	198.4	6.03	1185.81	11.52	18.48	5.92	34.09	2.37
		Th	**Error**	**Pb**	**Error**	**Au**	**Error**	**Se**	**Error**	**As**	**Error**
a	pc3	7.38	3.13	16.41	5.55	< LOD	-	< LOD	-	< LOD	-
b	pc3	6.94	2.91	12.49	4.83	< LOD	-	< LOD	-	< LOD	-
c	pc3	7.51	3.04	22.49	5.45	< LOD	-	< LOD	-	< LOD	-
d	pc3	7.2	3.32	22.03	5.72	< LOD	-	< LOD	-	< LOD	-
e	pc3	9.27	3.17	15.26	5.22	< LOD	-	< LOD	-	< LOD	-
f	pc3	8.6	3.32	13.12	5.24	< LOD	-	< LOD	-	< LOD	-
g	pc3	5.53	2.91	17.86	5.27	< LOD	-	< LOD	-	< LOD	-
		Hg	**Error**	**Zn**	**Error**	**W**	**Error**	**Cu**	**Error**	**Ni**	**Error**
a	pc3	< LOD	-	12.55	7.13	< LOD	-	< LOD	-	< LOD	-
b	pc3	< LOD	-	17.5	6.66	< LOD	-	26.44	12.05	43.5	24.66
c	pc3	< LOD	-	25.64	7.04	< LOD	-	25.78	12.04	77.7	25.5
d	pc3	< LOD	-	47.37	8.45	< LOD	-	33.48	13	79.47	27.42
e	pc3	< LOD	-	25.89	7.2	< LOD	-	37.31	12.73	57.09	25.59
f	pc3	< LOD	-	24.85	7.44	< LOD	-	34.83	12.98	79.62	26.98
g	pc3	< LOD	-	18.85	6.85	< LOD	-	26.93	12.2	< LOD	-
		Co	**Error**	**Fe**	**Error**	**Mn**	**Error**	**Cr**	**Error**	**V**	**Error**
a	pc3	< LOD	-	13033.64	229.92	231.29	54.36	< LOD	-	26.93	11.47
b	pc3	109.56	58.97	12706.52	1214.7	250.72	50.81	< LOD	-	73.79	29.09
c	pc3	< LOD	-	20721.01	272.12	307.45	54.53	< LOD	-	50.68	22.46
d	pc3	< LOD	-	43581.42	410.87	752.18	72.11	< LOD	-	166.88	32.71
e	pc3	< LOD	-	26245.51	305.87	456.35	60.26	91.11	23.54	90.78	24.46
f	pc3	< LOD	-	21991.65	1485.79	441.58	61.52	43.36	22.62	69.77	33.42
g	pc3	< LOD	-	16207.49	241.38	361.72	55.89	< LOD	-	40.21	18.98

Table 8. Handheld XRF data for the in-situ transect pc3. Values are given in ppm. LOD stands for Limit of Detection.

Sample	Transect	Ti	Error	Sc	Error	Ca	Error	K	Error	S	Error
a	pc3	1681.69	42.41	37.74	15.34	19493.17	460.68	14569.34	283.08	257.59	87.93
b	pc3	2447.72	113.75	-	-	16796.18	761.03	27257.63	1039.61	-	-
c	pc3	2854.21	80.38	65.84	26.02	20028.54	456.89	24685.7	348.02	657.43	166.63
d	pc3	7044.24	122.92	58.8	38.82	27822.13	578.09	16549.12	313.91	426.17	200.52
e	pc3	5030.54	92.01	82.26	28.54	23073.73	507.73	23488.52	350.22	389	160.51
f	pc3	2489.63	112	-	-	26865.6	1050.17	16297.56	601.61	-	-
g	pc3	2539.97	68.82	84.07	26.82	24401.45	489.5	17190.42	289.2	< LOD	-
		Ba	**Error**	**Cs**	**Error**	**Te**	**Error**	**Sb**	**Error**	**Sn**	**Error**
a	pc3	1052.11	55.4	84.79	12.49	116.95	36.74	32.64	13.44	22.61	10.51
b	pc3	1252.39	73.61	-	-	-	-	< LOD	-	< LOD	-
c	pc3	1256.09	45.85	75.93	10	114.29	29.53	25.67	10.73	26.65	8.5
d	pc3	1219.44	45.35	57.94	9.83	56.26	28.67	20.45	10.55	14.55	8.23
e	pc3	1088.6	43.16	51.1	9.49	62.05	27.85	< LOD	-	< LOD	-
f	pc3	1078.84	66.84	-	-	-	-	< LOD	-	< LOD	-
g	pc3	1457.01	49.87	82.36	10.64	99.71	31.13	36.85	11.52	24.86	8.99
		Cd	**Error**	**Ag**	**Error**	**Pd**	**Error**	**Nb**	**Error**	**Bi**	**Error**
a	pc3	< LOD	-	14.91	6.93	< LOD	-	11.3	1.78	< LOD	-
b	pc3	< LOD	-	< LOD	-	< LOD	-	15.18	10.03	< LOD	-
c	pc3	< LOD	-	< LOD	-	< LOD	-	8.04	1.58	< LOD	-
d	pc3	< LOD	-	< LOD	-	< LOD	-	18.74	1.85	< LOD	-
e	pc3	< LOD	-	< LOD	-	< LOD	-	21.34	1.85	< LOD	-
f	pc3	< LOD	-	< LOD	-	< LOD	-	< LOD	-	< LOD	-
g	pc3	< LOD	-	< LOD	-	< LOD	-	8.91	1.61	< LOD	-
		Re	**Error**	**Ta**	**Error**	**Hf**	**Error**				
a	pc3	< LOD	-	< LOD	-	< LOD	-				
b	pc3	< LOD	-	< LOD	-	< LOD	-				
c	pc3	< LOD	-	< LOD	-	< LOD	-				
d	pc3	< LOD	-	< LOD	-	< LOD	-				
e	pc3	< LOD	-	< LOD	-	< LOD	-				
f	pc3	< LOD	-	< LOD	-	< LOD	-				
g	pc3	< LOD	-	< LOD	-	< LOD	-				

Table 8. (cont.)

SAMPLE	Transect	Mo	Mo Error	Zr	Zr Error	Sr	Sr Error	U	U Error	Rb	Rb Error
a	pc5	< LOD	-	138.12	3.23	259.97	4.45	15.93	5.46	147.83	3.44
b	pc5	< LOD	-	66.16	2.64	131.45	3.48	8.47	5.59	145.31	3.85
c	pc5	< LOD	-	116.9	3.97	201.45	4.72	14.56	6.51	169	5.2
d	pc5	7.7	3.08	248.9	5.47	203.49	4.98	15.93	6.55	127.85	4.19
e	pc5	< LOD	-	184.91	6.59	1388.87	13.32	16.54	6.28	19.88	2.16
f	pc5	< LOD	-	100.36	5.53	1136.4	12.01	14.12	5.99	22.56	2.06
g	pc5	< LOD	-	178.63	7.81	2111.78	17.52	23.78	7.69	18.18	2.34

		Th	Th Error	Pb	Pb Error	Au	Au Error	Se	Se Error	As	As Error
a	pc5	15.65	2.82	33.22	4.63	< LOD	-	< LOD	-	< LOD	-
b	pc5	21.45	3.22	25.82	4.96	< LOD	-	< LOD	-	< LOD	-
c	pc5	21.42	3.62	20.86	5.19	< LOD	-	< LOD	-	< LOD	-
d	pc5	22.64	3.85	23.62	5.71	< LOD	-	< LOD	-	< LOD	-
e	pc5	13.39	3.69	16.35	5.67	< LOD	-	< LOD	-	< LOD	-
f	pc5	< LOD	-	17.85	5.38	< LOD	-	< LOD	-	8.78	4.59
g	pc5	5.96	3.67	23.07	6.54	< LOD	-	< LOD	-	< LOD	-

		Hg	Hg Error	Zn	Zn Error	W	W Error	Cu	Cu Error	Ni	Ni Error
a	pc5	< LOD	-	12.37	5.22	< LOD	-	15.75	9.5	65.08	20.29
b	pc5	< LOD	-	14.23	5.59	< LOD	-	< LOD	-	54.41	21.27
c	pc5	< LOD	-	15.65	6.34	< LOD	-	26.73	11.68	< LOD	-
d	pc5	< LOD	-	21.88	7.31	53.86	30.93	37.22	13.3	44.27	26.07
e	pc5	< LOD	-	41.94	8.83	86.93	34.98	38.17	14.38	110.84	30.16
f	pc5	< LOD	-	79.53	10.37	54.15	35.14	109.24	17.11	157.48	32.04
g	pc5	< LOD	-	36.87	9.27	< LOD	-	47.33	16.35	77.82	32.39

		Co	Co Error	Fe	Fe Error	Mn	Mn Error	Cr	Cr Error	V	V Error
a	pc5	< LOD	-	7933.56	133.46	230.26	41.18	< LOD	-	< LOD	-
b	pc5	< LOD	-	6746.15	110.4	217.6	43.93	< LOD	-	32.25	14.51
c	pc5	< LOD	-	6646.13	121.66	235.57	49.28	< LOD	-	< LOD	-
d	pc5	< LOD	-	19540.25	270.29	299.32	55.28	91.27	20.89	41.92	15.76
e	pc5	< LOD	-	40877.29	416.09	646.21	72.93	264.35	29.3	144.84	29.49
f	pc5	< LOD	-	58940.96	486.96	965.37	83	301.14	36.54	316.42	71.75
g	pc5	< LOD	-	34455.3	404.57	581.92	75.26	225.42	29.59	86.58	21.05

Table 9. Handheld XRF data for the in-situ transect pc5. Values are given in ppm. LOD stands for Limit of Detection.

SAMPLE		Ti	Ti Error	Sc	Sc Error	Ca	Ca Error	K	K Error	S	S Error
a	pc5	848.09	45.32	-	-	7257.08	309.72	43081.83	414.59	-	-
b	pc5	1120.14	49.57	< LOD	-	4173.32	112.52	47187.79	448.23	< LOD	199.11
c	pc5	1230.85	70.12	-	-	4081.62	349.06	56498.54	2004.48	-	-
d	pc5	1534.77	54.77	< LOD	-	4901.84	104.73	44509.24	487.27	253.24	122.88
e	pc5	6049.04	110.95	91.88	45	51356.53	808.34	9804.22	219.65	< LOD	-
f	pc5	8523.15	155.54	-	-	58650.44	950.38	13664.22	342.45	-	-
g	pc5	2157.12	73.11	119.29	34.26	51176.76	797.18	4734.32	137.02	294.77	132.52

		Ba	Ba Error	Cs	Cs Error	Te	Te Error	Sb	Sb Error	Sn	Sn Error
a	pc5	1243.53	49.33	-	-	-	-	< LOD	-	< LOD	-
b	pc5	682.91	37.72	79.62	8.94	112.25	26.38	28.16	9.63	26.05	7.58
c	pc5	780.73	56.25	-	-	-	-	< LOD	-	< LOD	-
d	pc5	860.6	46.52	56.9	10.61	53.11	30.93	23.48	11.46	14.38	8.89
e	pc5	2049.64	59.32	110.24	12	169.45	35.47	40.68	12.87	29.87	10.08
f	pc5	1859.59	65.74	-	-	-	-	< LOD	-	< LOD	-
g	pc5	1908.44	62.26	113.46	12.82	155.22	37.65	41.08	13.75	35.78	10.87

		Cd	Cd Error	Ag	Ag Error	Pd	Pd Error	Nb	Nb Error	Bi	Bi Error
a	pc5	< LOD	-	< LOD	-	< LOD	-	10.34	1.27	11.36	3.86
b	pc5	11.94	7.2	< LOD	-	< LOD	-	9.27	1.41	20.77	4.6
c	pc5	< LOD	0	< LOD	-	< LOD	-	< LOD	-	< LOD	-
d	pc5	< LOD	0	< LOD	-	< LOD	-	16.07	1.79	23.2	5.38
e	pc5	16.68	9.59	< LOD	-	< LOD	-	13.87	1.81	10.36	4.66
f	pc5	< LOD	0	< LOD	-	< LOD	-	17.13	1.76	< LOD	-
g	pc5	25.41	10.45	< LOD	-	< LOD	-	10.89	1.89	< LOD	-

		Re	Re Error	Ta	Ta Error	Hf	Hf Error
a	pc5	< LOD	-	< LOD	-	< LOD	-
b	pc5	< LOD	-	< LOD	-	< LOD	-
c	pc5	< LOD	-	< LOD	-	< LOD	-
d	pc5	< LOD	-	< LOD	-	< LOD	-
e	pc5	< LOD	-	< LOD	-	< LOD	-
f	pc5	< LOD	-	< LOD	-	< LOD	-
g	pc5	< LOD	-	< LOD	-	< LOD	-

Table 9. (cont.)

Sample	Transect	Mo	Error	Zr	Error	Sr	Error	U	Error	Rb	Error
a	PS	< LOD	-	138.38	4.92	635.36	8.51	9.05	5.8	75.12	3.24
b	PS	< LOD	-	225.32	6.32	439.07	7.73	< LOD	-	90.68	4.01
c	PS	5.65	3.22	250.96	6.38	696.77	9.51	18.04	6.69	80.97	3.58
d	PS	< LOD	-	229.51	40.63	637.25	58.66	< LOD	-	67.8	21.61
e	PS	< LOD	-	265.84	6.72	771.67	10.33	< LOD	-	84.28	3.62
f	PS	< LOD	-	284.26	6.98	1203.5	12.1	20.11	7.24	91.69	3.71
g	PS	< LOD	-	47.98	4.85	1062.11	11.44	19.91	7.04	85.8	3.61
h	PS	< LOD	-	180.9	5.44	861.25	9.63	18.82	6.38	91.25	3.46
i	PS	< LOD	-	279.79	6.26	855.41	9.73	19.62	6.53	93.73	3.55
j	PS	< LOD	-	274.4	6.13	761.48	9.19	14.88	6.13	80.42	3.31
		Th	**Error**	**Pb**	**Error**	**Au**	**Error**	**Se**	**Error**	**As**	**Error**
a	PS	7.4	3.03	28.91	5.76	< LOD	-	< LOD	-	< LOD	-
b	PS	< LOD	-	49.54	7.67	< LOD	-	< LOD	-	< LOD	-
c	PS	20.41	4.06	40.17	6.82	< LOD	-	< LOD	-	< LOD	-
d	PS	< LOD	-	< LOD	-	< LOD	-	< LOD	-	< LOD	-
e	PS	< LOD	-	53.15	7.29	< LOD	-	< LOD	-	< LOD	-
f	PS	15.46	3.93	52.94	7.19	< LOD	-	< LOD	-	9.65	5.18
g	PS	17.25	3.98	55.81	7.26	< LOD	-	< LOD	-	10.07	5.19
h	PS	12.1	3.31	44.41	6.33	< LOD	-	< LOD	-	< LOD	-
i	PS	15.47	3.51	38.66	6.2	< LOD	-	< LOD	-	< LOD	-
j	PS	14.14	3.42	40.86	6.27	< LOD	-	< LOD	-	< LOD	-
		Hg	**Error**	**Zn**	**Error**	**W**	**Error**	**Cu**	**Error**	**Ni**	**Error**
a	PS	< LOD	-	17.83	6.84	< LOD	-	< LOD	-	< LOD	-
b	PS	< LOD	-	37.75	10.41	< LOD	-	< LOD	-	< LOD	-
c	PS	< LOD	-	55.52	9.22	< LOD	-	31.52	14.33	< LOD	-
d	PS	< LOD	-	< LOD	-	< LOD	-	< LOD	-	< LOD	-
e	PS	< LOD	-	70.35	10.92	< LOD	-	< LOD	-	< LOD	-
f	PS	< LOD	-	79.27	9.95	49.71	32.25	43.12	13.94	101.21	28.81
g	PS	< LOD	-	76.03	9.83	< LOD	-	71.72	14.98	< LOD	-
h	PS	< LOD	-	22.2	6.85	< LOD	-	21.44	11.92	42.82	24.49
i	PS	< LOD	-	21.88	6.97	< LOD	-	22.22	11.99	45.35	24.94
j	PS	< LOD	-	23.02	7.04	< LOD	-	34.63	12.56	55.03	25.16

Table 10. Handheld XRF data for the in-situ transect PS. Values are given in ppm. LOD stands for Limit of Detection.

Sample	Transect	Co	Error	Fe	Error	Mn	Error	Cr	Error	V	Error
a	PS	< LOD	-	6527.9	124.86	242.75	51.25	< LOD	-	50.56	27.83
b	PS	< LOD	-	27219.29	358.83	851.25	112.77	< LOD	-	61.1	14.5
c	PS	< LOD	-	27254.58	336.45	550.45	68.01	< LOD	-	70.23	18.12
d	PS	< LOD	-	39528.28	2596.66	< LOD	-	54.77	30.29	195.47	52.55
e	PS	< LOD	-	33810.66	375.13	901.23	103.84	< LOD	-	88.93	21.34
f	PS	< LOD	-	38786.05	393.55	976.66	78.35	< LOD	-	148.65	30.7
g	PS	< LOD	-	39415.63	398.67	1270.45	85.09	< LOD	-	111.97	24.71
h	PS	< LOD	-	11757.84	202.43	345.21	53.87	< LOD	-	33.71	17.6
i	PS	< LOD	-	15297.18	233.37	347.5	55.2	< LOD	-	44.24	20.06
j	PS	< LOD	-	16544.63	242.25	373.57	56.51	< LOD	-	66.27	20.1
		Ti	**Error**	**Sc**	**Error**	**Ca**	**Error**	**K**	**Error**	**S**	**Error**
a	PS	1054.69	46.6	31.51	16.31	15687.2	395.02	27914.16	359.4	238.72	105.66
b	PS	2138.47	52.11	33.77	16.54	20291.83	499.85	27011.47	396.63	462.83	110.61
c	PS	2638.31	65.06	69.62	20.85	23148.04	528.12	27694.16	398.13	356.22	123.44
d	PS	4790.58	235.01	-	-	34491.59	1551.53	16612.88	724.55	-	-
e	PS	3659.5	77.77	61.23	25.75	33556.49	651.2	22938.39	377.98	390.2	132.71
f	PS	6421.59	115.06	< LOD	-	33513.98	665	24598.78	395.23	< LOD	-
g	PS	4643.85	91.55	70.05	30.79	29680.3	600.83	21171.79	353.09	373.54	156
h	PS	1681.26	61.27	30.65	18.64	16591.59	417.77	39922.55	430.54	342.82	129.81
i	PS	2173.2	70.47	38.05	21.03	16193.1	427.36	39930.78	439.98	392.87	148.97
j	PS	3591.46	73.96	< LOD	-	20801.07	460.62	28982.73	371.56	362.63	137.63
		Ba	**Error**	**Cs**	**Error**	**Te**	**Error**	**Sb**	**Error**	**Sn**	**Error**
a	PS	1934	53.22	117.88	10.92	153.56	32.04	43.19	11.75	37.28	9.28
b	PS	1912.71	65.42	127.64	13.59	247.21	40.81	72.46	14.98	52.82	11.76
c	PS	1731.13	56.4	101.07	11.77	164.56	34.88	46.88	12.76	32.39	9.99
d	PS	1376.88	101.07	-	-	-	-	< LOD	-	< LOD	-
e	PS	1998.05	63.64	104.76	12.92	131.24	37.74	40.2	13.84	24.69	10.79
f	PS	1816.51	53.23	66.71	10.78	62.7	31.34	< LOD	17.18	23.13	9.11
g	PS	1807.96	55.43	98.16	11.45	166.1	33.99	46.22	12.44	38.09	9.81
h	PS	2416.94	56.03	100.6	10.84	146.61	31.93	37.4	11.62	31.38	9.17
i	PS	2395.74	51.48	87.35	9.9	109.87	28.99	30.06	10.59	24.25	8.33
j	PS	1754.53	47.84	70.16	9.77	72.35	28.46	28.27	10.52	13.72	8.13

Table 10. (cont.)

Sample	Transect	Cd	Error	Ag	Error	Pd	Error	Nb	Error	Bi	Error
a	PS	25.74	8.92	< LOD	-	< LOD	-	5.57	1.56	< LOD	6.46
b	PS	34.06	11.21	< LOD	-	< LOD	-	16.06	2.03	13.06	5.6
c	PS	< LOD	-	11.28	6.36	< LOD	-	21.16	1.99	17.76	5.33
d	PS	< LOD	-	< LOD	-	< LOD	-	< LOD	-	< LOD	-
e	PS	< LOD	-	12.84	7.02	< LOD	-	19.36	1.93	10.46	5.16
f	PS	< LOD	-	< LOD	-	< LOD	-	18.44	1.87	13.3	5.24
g	PS	20.11	9.29	< LOD	-	< LOD	-	17.89	1.86	15.43	5.29
h	PS	< LOD	-	< LOD	-	< LOD	-	12.37	1.65	9.4	4.59
i	PS	< LOD	-	< LOD	-	< LOD	-	13.43	1.69	14.18	4.84
j	PS	< LOD	-	< LOD	-	< LOD	-	20.44	1.82	13.36	4.73

		Re	Error	Ta	Error	Hf	Error
a	PS	< LOD	-	< LOD	-	< LOD	-
b	PS	< LOD	-	< LOD	-	< LOD	-
c	PS	< LOD	-	< LOD	-	< LOD	-
d	PS	< LOD	-	< LOD	-	< LOD	-
e	PS	< LOD	-	< LOD	-	< LOD	-
f	PS	< LOD	-	< LOD	-	< LOD	-
g	PS	< LOD	-	< LOD	-	< LOD	-
h	PS	< LOD	-	< LOD	-	< LOD	-
i	PS	< LOD	-	< LOD	-	< LOD	-
j	PS	< LOD	-	< LOD	-	< LOD	-

Table 10. (cont.)